Alma Mater Studiorum - Università di Bologna

DOTTORATO DI RICERCA IN

INGEGNERIA ELETTRONICA, TELECOMUNICAZIONI E TECNOLOGIE DELL'INFORMAZIONE

Ciclo 35

Settore Concorsuale: 09/E3 - ELETTRONICA

Settore Scientifico Disciplinare: ING-INF/01 - ELETTRONICA

PHYSICAL MODELING AND NUMERICAL SIMULATIONS OF DEGRADATION MECHANISMS IN DEVICES AND INSULATORS FOR POWER APPLICATIONS

Presentata da: Federico Giuliano

Coordinatore Dottorato

Aldo Romani

Supervisore

Susanna Reggiani

Co-supervisore

Claudio Fiegna

Esame finale anno 2023

ALMA MSTER STUDIORUM - UNIVERSITÀ DI BOLOGNA

Abstract

ARCES-DEI

Doctor of Philosophy

Physical modeling and numerical simulations of degradation mechanisms in devices and insulators for power applications

by Federico Giuliano

Metal-insulator-metal (MIM) capacitors embedded in the back-end interlevel dielectric layers have been recently proposed for analog and RF applications. Silicon dioxide (SiO_2) is the main insulator in the electronics industry because of its near-ideal properties; however, ultimate device degradation and failure is still limited by charge buildup in defect sites of the oxide layer. The capacitors for galvanic insulation are complex structures with a large thickness (in the micrometer range) subject to high electric fields. The plasma-enhanced chemical vapor deposition process (PE-CVD) using the tetraehtyl orthosilicate (TEOS) as a precursor is usually adopted for interlayer dielectrics allowing to grow thick amorphous SiO_2 films. TEOS capacitors for galvanic insulation are complex structures made through several oxidation steps due to requirement related to the relaxation of the mechanical stress that arises during the deposition process. Due to the relevant differences in the processing steps adopted for the SiO_2 growth, the dielectric tends to show different electrical properties with respect to thermally grown SiO_2. TEOS SiO_2 is known to provide a high leakage current and is found to have a much larger density of preexisting defects. However, charge transport characterization and modeling has rarely been studied. It is well known that charge build-up in the bulk of the oxide and charge injection at the contacts can significantly modify the electric field distribution across the device. An undesired leakage current may arise that limits the device performance and reliability. For this reason, a detailed knowledge of charge injection and transport mechanisms of such materials under high electric fields plays a key role in improving the reliability of such devices.

In this thesis, a TCAD approach for the investigation of charge transport in amorphous silicon dioxide is presented for the first time. The proposed approach is used to investigate high-voltage silicon oxide thick TEOS capacitors

embedded in the back-end inter-level dielectric layers for galvanic insulation applications. In the first part of this thesis, a detailed review of the main physical and chemical properties of silicon dioxide and the main physical models for the description of charge transport in insulators are presented. In the second part, the characterization of high-voltage MIM structures at different high-field stress conditions up to the breakdown is presented with the measurements provided by STMicroelectronics. The main physical mechanisms responsible of the observed results are then discussed in details. The third part, which is also the core of this thesis activity, is dedicated to the implementation of a TCAD approach capable of describing charge transport in silicon dioxide layers in order to gain insight into the microscopic physical mechanisms responsible of the leakage current in MIM structures. In particular, I investigated and modeled the role of charge injection at contacts and charge build-up due to trapping and de-trapping mechanisms in the bulk of the oxide layer to the purpose of understanding the oxide behavior under DC and AC stress conditions. In addition, oxide breakdown due to impact-ionization of carriers has been taken into account in order to have a complete representation of the oxide behavior at very high fields. Numerical simulations have been compared against experiments to quantitatively validate the proposed approach. In the last part of the thesis, the proposed approach has been applied to simulate the breakdown in realistic structures in order to gain insight on the effect of the geometry of such structures on the breakdown under different stress conditions. In particular, the dependence of the breakdown field on several parameters, such as the oxide thickness and the stress condition, has been extensively investigated. The TCAD tool has been used to carry out a detailed analysis of the most relevant physical quantities, such as the trapped charge in the bulk oxide or the electric field, in order to gain a detailed understanding on the main mechanisms responsible for breakdown and guide design optimization.

Contents

Abstract **i**

1 Introduction **1**

2 Theory **9**

2.1 Silicon Oxide 9

2.1.1 Atomic structure of SiO_2 10

2.1.2 Electronic structure 13

2.1.3 High-field transport 15

2.2 Conduction mechanisms in insulators 17

2.2.1 Injection-limited conduction mechanisms 17

Thermionic emission 17

Fowler-Nordheim tunneling 18

Thermionic-field emission 19

2.2.2 Bulk-limited conduction mechanisms 20

Ohmic conduction 20

Space-Charge Limited conduction 21

Trap-assisted conduction 21

Ionic conduction 22

2.3 Drift-Diffusion model 23

2.3.1 Boundary conditions 26

2.4 Generation Recombination processes 27

2.4.1 Schockley-Read-Hall recombination 27

2.4.2 Auger recombination 27

2.4.3 Impact-ionization generation 28

2.5 Trap dynamics 30

2.6 TCAD-based numerical simulations 34

3 Characterization of TEOS MIM structures **37**

3.1 Experimental setup 37

3.2 Test structures characteristics 38

3.2.1 Breakdown under different stress conditions 42

3.3 Thickness dependence of the breakdown in realistic structures 47

4 TCAD modeling of the SiO_2 53

4.1 Modeling approach 54
4.1.1 Electronic structure 56
4.1.2 Electron and hole mobility 57
4.1.3 Charge injection 58
4.1.4 Defects 61
Poole-Frenkel model 63
Hurkx model 64
4.1.5 Impact-ionization 65
Van Overstraeten-De Man model 66
Okuto-Crowell model 66
4.2 Simulation results 66
4.2.1 Breakdown 73

5 Thickness dependence of the breakdown in realistic structures 81

5.1 2-D TCAD structure 81
5.2 Modifications to the impact ionization model 82
5.3 Simulation results 84
5.3.1 TCAD analysis of the AC breakdown at different oxide thicknesses 87
5.3.2 TCAD analysis of the breakdown under AC and DC stresses 92

6 Conclusions 97

List of Figures

1.1 Schematic view of a typical TEOS stacked capacitor. The TEOS thickness is in the range $10 - 20\mu$ m. From [4]. 2
1.2 Energy band diagram representation of injection-limited conduction mechanisms: thermionic emission, thermionic-field emission and Fowler-Nordheim tunneling. From [8]. 3

2.1 Schematic representation of the SiO_2 molecule. 11
2.2 Schematic representation of the tetrahedral structure of SiO_2. 11
2.3 Reflection spectra of amorphous SiO_2 and α-quartz. From [31]. 13
2.4 Fragment consisting of two SiO_2 tetrahedra: Ψ, O-Si-O tetrahedral angle; θ, Si-O-Si dihedral angle. From [28]. 14
2.5 Representation of the first Brillouin zone in α-SiO_2. From [29]. 14
2.6 Dependence of the energy on the quasi-momentum in α-SiO_2. From [29]. 15
2.7 Energy band diagram of the thermionic emission in a metal-insulator-metal structure. The blue dashed line represents the barrier lowering due to the Schottky effect. 18
2.8 Energy band diagram of the Fowler-Nordheim tunneling mechanism in a metal-insulator-metal structure. 19
2.9 Energy band diagram of the thermionic-field emission mechanism in a metal-insulator-metal structure. 19
2.10 Boundary conditions in a device. Black: insulating boundaries. Magenta: conducting boundaries. 26
2.11 Electron energy band diagram for an insulator or a semiconductor with deep-level impurities. From [37]. 30
2.12 Schematic representation of the electric-field-assisted emission mechanisms from a Coulombic well. From [46]. 34

3.1 Schematic view of the TEOS test structure. 38

3.2 **Top:** Oxide band diagram modifications due to the trapped charge. Charge trapping modifies the internal electric field distribution leading to different injection probabilities between the forward and the backward ramp. **Bottom:** Measured current densities as a function of the electric field. Two voltage ramp-rates have been applied, namely 24 V/s and 6 V/s. For the faster ramp measurements with both the polarities are represented. Black curve(squares): total measured current with negative bias; blue curve (squares): total measured current with positive bias; red curve (circles): areal contribution with negative bias; green curve (triangles): negative bias with ramp rate of 6V/s. 39
3.3 Slow voltage ramp measurements at different temperature conditions up to breakdown: $T = 25$ °C, $T = 100$ °C and $T = 150$ °C. 41
3.4 Inverse normal distribution of the breakdown voltage (and field) at $T = 25$ °C under DC negative (red), DC positive (black) and AC bipolar (blue) ramps. 42
3.5 **Left:** AC stress applied voltage. The amplitude is 650 V and the period is 14 s. **Right:** Current versus time semi-log plot of the AC (lines+symbols) and negative polarity DC (symbols) characteristics. The first semiperiod of the AC characteristics has negative polarity. Inset: log-log current plot of the DC measurements. 43
3.6 Voltage applied to the capacitor as a function of stress time (top) and current density flowing through the insulator as a function of time (bottom) during the constant-current stress. The target current is represented by the red dashed line. . . . 44
3.7 Constant current measurements performed on the SiO_2 TEOS thick capacitor. Two temperature conditions have been tested, namely $T = 25$ °C (close symbols) and $T = 150$ °C (open symbols). 45
3.8 Top: AC square wave signal and negative and positive staircase DC ramps (black and red lines) applied to the MIM under study. Bottom: Magnification of the applied AC signal. The applied voltage to the peak voltage ratio is plotted as a function of time. The period is $T = 0.82$ s. 46

3.9 Current density as a function of the applied electric field for the AC and DC stresses. 47
3.10 Schematic view of the 2D structure of the TEOS capacitor (not in scale). 48
3.11 Measurements of the current density as a function of the oxide field up to the breakdown for the devices with thickness 0.6μm and 0.9μm. 50
3.12 Breakdown field as a function of the oxide thickness for samples with thicknesses up to 17μm under AC and DC stresses. The black line has been obtained by fitting the DC-stress data with Eq. 3.3. $E_{\text{ref}} = 9.09$ MV/cm; $E_0 = 298$ MV/cm; $t_{\text{ref}} = 1\mu$m. 51

4.1 Conduction mechanisms in an insulator. In the proposed modeling approach, tunneling and trapping and de-trapping of electrons are taken into account. Trap-to-trap conduction (hopping, or multi-TAT) is expected not to be relevant, hence it is not taken into account. 55
4.2 Electron drift velocity as a function of the electric field at room temperature, namely $T = 300$K. Symbols: experiments from [68]. Solid line: TCAD model. The black dashed line represents the saturation velocity $v_{\text{sat}} = 1.6 \cdot 10^7$cm/s. 58
4.3 Analysis of charge injection: current density as a function of the oxide field at two temperature conditions, namely $T = 25$ °C and $T = 150$ °C. Simulations have been performed with no traps and by activating the barrier lowering model. 59
4.4 Analysis of charge injection: current density as a function of the oxide field at two temperature conditions, namely $T = 25$ °C and $T = 150$ °C. Simulations have been performed with no traps. Inset: Metal-insulator band diagram. 60
4.5 Electron and hole current densities as a function of the applied electric field from simulations for a voltage ramp stress with ramp rate of 6 V/s. 62
4.6 Energy distribution of traps. Both the uniform distribution adopted and the equivalent densities with Gaussian functions are plotted. The valence band has been taken as the reference level, i.e. $E_V = 0$. The point $(E_C - E_V)/2$ represents the mid-band gap and corresponds to the Fermi level. A band-gap $E_G = 8.9$ eV is assumed for SiO_2. 62

4.7 Trapped charge concentration as a function of time for a square wave AC stress near the top contact. Continuous line: simulation performed activating the Hurkx model; Dashed line: simulation performed without the Hurkx model. 65
4.8 Current density as a function of the applied electric field for voltage ramp stress up to breakdown. Three temperature conditions are represented, namely $T = 25$ °C, $T = 100$ °C and $T = 150$ °C. Symbols: experiments; Solid and dashed lines: simulations. 67
4.9 Current density as a function of the applied electric field for voltage ramp stress up to $F_{OX} = 6.75$ MV/cm. Two ramp rates have been used, namely 24 V/s and 6 V/s. Red Symbols: experiments, areal current (fast ramp); Blue symbols: experiments, total current (slow ramp); Lines: simulations. 68
4.10 **Left:** Semi-logarithmic current plot comparison of experimental data (symbols) and simulation results (lines) for a constant voltage stress performed at $F_{OX} = 6.65$ MV/cm. **Right:** Log-log current plot comparison of experimental data (symbols) and simulation results (lines) for a constant voltage stress performed at $F_{OX} = 6.65$ MV/cm. The black solid lines were obtained with the calibrated parameters for all the traps (reported in Table 4.2), while the blue dashed and red dash-dotted lines were obtained by changing either the capture cross section or the trap level of the first trap, respectively. 69

4.11 Semi-logarithmic current plot comparison of experimental data (symbols) and simulation results (solid and dashed lines) for a constant voltage stress performed at $F_{OX} = 6.65$ MV/cm and room temperature. **Left**: The black solid line was obtained with the calibrated parameters for all the traps (reported in Table 4.2), while the magenta dashed and the blue dash-dotted lines were obtained by defining only one distribution of traps, T1 and T2 respectively, with the calibrated parameters. **Right**: The black solid line was obtained with the calibrated parameters for all the traps (reported in Table 4.2). Other simulations were performed by defining only one distribution of traps (T1) and changing only one parameter at a time (with respect to those reported in Table 4.2): the energy level of the trap (magenta dash-dotted line), the total concentration (green dashed line) and the capture cross section (blue solid line). 70
4.12 Current density as a function time for a square wave AC stress with period $T = 14$ s and amplitude $F_{OX} = 6.65$ MV/cm. Symbols+line: experiments; Solid lines: simulations with the Hurkx model; Dashed line: simulations without the Hurkx model. 71
4.13 Trapped charge as a function of the position across the oxide layer for the DC-stress. Three instants are represented: $t = 1$ s (solid line), $t = 40$ s (dashed line), $t = 100$ s (dotted line). . . . 71
4.14 Electric field distribution across the oxide layer for the DC-stress. Three instants are represented: $t = 1$ s (solid line), $t = 40$ s (dashed line), $t = 100$ s (dotted line). 72
4.15 Trapped charge as a function of the position across the oxide layer for the AC-stress. Three instants are represented: $t = 1$ s (solid line), $t = 40$ s (dashed line), $t = 100$ s (dotted line). . . . 72
4.16 Electron avalanche coefficient as a function of the electric field at room temperature. Symbols: experimental data in [78]. Solid line: calibrated TCAD model at room temperature. Dashed line: calibrated TCAD model at $T = 150°$C. 73
4.17 Electron avalanche scattering rate as a function of the position across the device thickness at $F_{0X} = 4$ MV/cm (low field regime), $F_{0X} = 6.5$ MV/cm (intermediate field regime) and $F_{0X} = 8.7$ MV/cm (high field regime). 74

4.18 Experiments (left) and simulations (right) of the oxide field plotted as a function of time at different temperatures, namely $T = 25$ °C and $T = 150$ °C during the constant-current stress. . . . 75
4.19 Electric field distribution across the device at $T = 25$ °C and $J = 6.3 \cdot 10^{-8}$ A/cm^2 for three different stress times. 75
4.20 Total trapped charge across the device at $T = 25$ °C and $J = 6.3 \cdot 10^{-8}$ A/cm^2 for three different stress times. 76
4.21 Avalanche generation rate across the device at $T = 25$ °C and $J = 6.3 \cdot 10^{-8}$ A/cm^2 for three different stress times. 77
4.22 Current density as a function of the oxide field for the AC and DC voltage ramp stresses. Dots: Experiments. Solid lines: simulations with impact ionization (solid and dashed lines) and without (dotted and dash-dotted lines). 77
4.23 Trapped charge across the device under AC and DC regimes at two different oxide fields, namely $F_{OX} = 6$ MV/cm (in the cherge-trapping portion of the J-E characteristics) and $F_{OX} = 8.5$ MV/cm (just before the AC breakdown). 78
4.24 Electric field distribution across the device under AC and DC regimes at two different oxide fields, namely $F_{OX} = 6$ MV/cm (in the charge-trapping portion of the J-E characteristics) and $F_{OX} = 8.5$ MV/cm (just before the AC breakdown). 79

5.1 Schematic view of the 2D simulated structure of the TEOS capacitor (not in scale). 82
5.2 Electron avalanche coefficient as a function of the electric field. Left: Experimental data in [78] and the calibrated Van Overstraeten model at room temperature (solid line) and at $T = 150$°C (dashed line). Right: Experimental data in [78] and the calibrated Okuto model at room temperature. 84
5.3 Current density as a function of the oxide field up to the breakdown for different oxide thickness. Symbols and lines: experiments. Lines: Simulations at $t_{OX} = 0.6\mu$m, $t_{OX} = 0.9\mu$m and $t_{OX} = 15\mu$m. 85
5.4 Breakdown field as a function of the oxide thickness for samples with thicknesses up to 15μm under AC and DC stresses. Dots: experiments. Lines and dots: Simulations. 86

5.5 Electric field within the oxide layer for two thicknesses and cutlines of the impact-ionization generation rate and the current density along the Y axis (black lines in the leftmost figures). A. Electric field distribution for $t_{OX} = 0.9\mu$m at $E_{OX} =$ 9.4MV/cm (onset of avalanche breakdown). B. Impact-ionization generation rate along the Y coordinate in proximity of the top metal contact. C. Electric field distribution for $t_{OX} = 15\mu$m at $E_{OX} = 9.0$MV/cm (onset of avalanche breakdown). D. Current density along the Y coordinate in proximity of the top metal contact. X and Y axes have arbitrary units. The same scale is used on every Y axis, while different scales have been used for the X axes due to the different thicknesses. The distances from the two cutlines to the respective top metal contacts are the same. For the schematic of the structure, see Fig. 3.10. 87
5.6 Electric field within the oxide layer for the oxides with thicknesses: $t_{OX} = 0.9\mu$m (A-B) and $t_{OX} = 15\mu$m (C-D) at positive and negative polarity during the AC stress. X and Y axes have arbitrary units. The same scale is used on every Y axis, while different scales have been used for the X axes due to the different thicknesses. 88
5.7 Electric field along the Y axis for two thicknesses at positive and negative polarity during the AC stress. 89
5.8 Electric field along the X axis for the oxide with $t_{OX} = 15\mu$m during the AC stress at negative and positive polarity. 89
5.9 Impact ionization generation rate across the thick oxide ($t_{OX} = 15\mu$m) during the AC stress at $E_{OX} = 3.8$MV/cm for positive and negative polarity. 90
5.10 Trapped charge within the oxide layer for the oxides with thicknesses: $t_{OX} = 0.9\mu$m (A-B) and $t_{OX} = 15\mu$m (C-D) at positive and negative polarity during the AC stress. X and Y axes have arbitrary units. The same scale is used on every Y axis, while different scales have been used for the X axes due to the different thicknesses. 90

5.11 Trapped charge density along the normalized X axis (X_{norm}) during the AC stress at negative and positive polarity with $E_{\text{OX}} = 3.8$MV/cm. Dashed lines: $t_{\text{OX}} = 0.9\mu$m. Solid lines: $t_{\text{OX}} = 15\mu$m. The position $X_{\text{norm}} = 0$ corresponds to the bottom metal, the position $X_{\text{norm}} = 1$ corresponds to $X = t_{\text{OX}}$ (top metal). 91
5.12 Electric field along the normalized X axis during the AC stress at negative and positive polarity with $E_{\text{OX}} = 3.8$MV/cm. Solid lines: $t_{\text{OX}} = 15\mu$m. Dashed lines: $t_{\text{OX}} = 0.9\mu$m. The position $X_{\text{norm}} = 0$ corresponds to the bottom metal, the position $X_{\text{norm}} = 1$ corresponds to $X = t_{\text{OX}}$ (top metal). 92
5.13 Electric field profile within the thick oxide ($t_{\text{OX}} = 15\mu$m) during AC and DC stresses. A) DC stress at $E_{\text{OX}} = 3.8$MV/cm (far from breakdown) with negative polarity. B) DC stress at $E_{\text{OX}} = 8.8$MV/cm (onset of avalanche breakdown) with negative polarity. C-D) AC stress at $E_{\text{OX}} = 3.8$MV/cm with positive and negative polarity, respectively. 93
5.14 Impact ionization generation rate within the thick oxide ($t_{\text{OX}} = 15\mu$m) during AC and DC stresses. A) DC stress at $E_{\text{OX}} = 3.8$MV/cm (far from breakdown) with negative polarity. B) DC stress at $E_{\text{OX}} = 8.8$MV/cm (onset of avalanche breakdown) with negative polarity. C) AC stress at $E_{\text{OX}} = 3.8$MV/cm with positive polarity. D) AC stress at $E_{\text{OX}} = 3.8$MV/cm with negative polarity. 94
5.15 Trapped charge in the thick oxide ($t_{\text{OX}} = 15\mu$m) during AC and DC stresses. A) DC stress at $E_{\text{OX}} = 3.8$MV/cm (far from breakdown) with negative polarity. B) DC stress at $E_{\text{OX}} = 8.8$MV/cm (onset of avalanche breakdown) with negative polarity. C-D) AC stress at $E_{\text{OX}} = 3.8$MV/cm with positive and negative polarity, respectively. 95

List of Tables

3.1 Temperature conditions and current density targets used in experiments. . . . 44
3.2 Nominal oxide thickness, voltage ramp rates and oxide field ramp rates applied to the MIM structures used in experiments. 49

4.1 TCAD parameter set for SiO_2 and TaN: metal Work Function (Φ_m), metal-oxide Energy barrier (E_B), Energy bandgap (E_G), conduction and valence band denstity of states (N_C and N_V) and electron and hole mobility (μ_e and μ_h) are reported. . . . 61
4.2 Trap parameters used for the two trap distributions. Mean energy of the trap level, trap width, electron capture cross section and trap density are reported for each type of trap. The parameter E_T is referred to the top of the conduction band, taken as the reference level. . . . 63

List of Abbreviations

BTE	**B**oltzmann **T**ransport **E**quation
CVD	**C**hemical **V**apor **D**eposition
DD	**D**rift **D**iffusion
IC	**I**ntegrated **C**ircuit
IoT	**I**nternet **o**f **T**hings
LO	**L**ongitudinal **O**ptical
MIM	**M**etal **I**nsulator **M**etal
NMP	**N**onradiative **M**ulti-**P**honon
PAT	**P**honon **A**ssisted **T**unneling
PE	**P**lasma **E**nhanced
PF	**P**oole **F**renkel
RDF	**R**adial **D**istribution **F**unction
SCLC	**S**pace **C**harge **L**imited **C**urrent
SEM	**S**canning **E**lectron **M**icroscope
SRH	**S**chockley **R**ead **H**all
TAT	**T**rap **A**ssisted **T**unneling
TDDB	**T**ime **D**ependent **D**ielectric **B**reakdown
TDDB	**T**ime **D**ependent **D**ielectric **S**pectroscopy
TEOS	**T**etra**E**thyl **O**rtho**S**ilicate
ULSI	**U**ltra **L**arge **S**cale **I**ntegration
WKB	**W**entzel **K**ramers **B**rillouin

Chapter 1

Introduction

There is an increasing demand for systems that integrate logic, memory and power integrated circuits (ICs), especially for high power applications involving automobiles, drones, robots, and the Internet of Things (IoT) controllers. Historically, the high voltage and low voltage ICs have been integrated by optical interconnects so that the circuits remain isolated, but the signals communicated. Optical interconnects consume a significant amount of power and they have a large area footprint. Therefore, an alternative approach based on technologies compatible with IC processing techniques leading to far less power consumption and less area occupation, would be particularly appealing. In this regard, a new multi-kV voltage transformer, which uses standard IC back-end inter-metal dielectric as an ultra-compact capacitive voltage-divider to connect high and low voltage ICs, has received considerable attention [1]. Moreover, metal-insulator-metal (MIM) capacitors embedded in the back-end inter-level dielectric layers have been recently proposed for analog and RF applications [2], [3].

Silicon dioxide (SiO_2) is the main insulator in the electronic industry because of its near-ideal properties; however, the degradation and failure of MIM devices is still limited by charge buildup in pre-existing defect sites of the oxide layer. Moreover, tetraethyl orthosilicate (TEOS) capacitors for galvanic insulation are complex structures made through several oxidation steps due to their large thickness subject to high and non-uniform electric fields [1]. Figure 1.1 shows a schematic diagram of a typical stacked capacitor. The number of layers scales with the total oxide thickness. Since the structure is embedded in the back-end, the high voltage is applied directly at the top electrode where the bond wire is connected.

The tetraethyl orthosilicate ($Si(OC_2H_5)_4$: TEOS) is usually adopted as a precursor for the interlayer thick oxides in the plasma-enhanced chemical vapor deposition process(PE-CVD). Such technique allows to deposit thick SiO_2 films in the back-end with good physical properties, but they are known

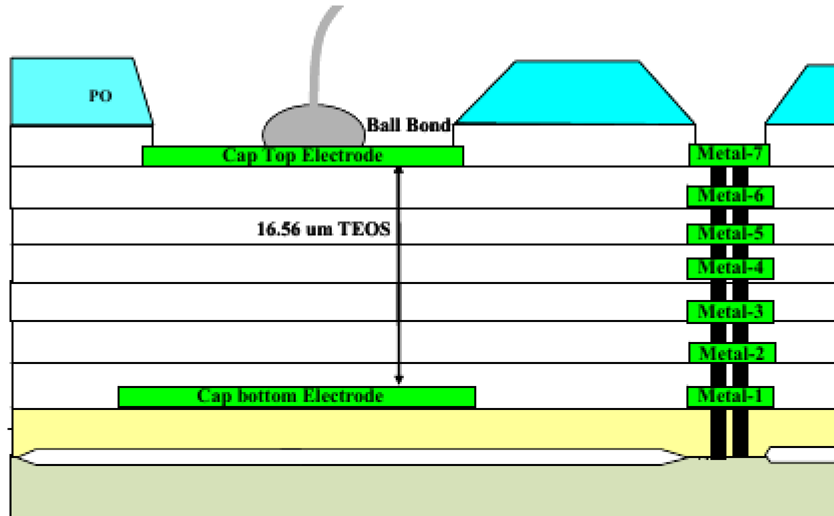

Figure 1.1: Schematic view of a typical TEOS stacked capacitor. The TEOS thickness is in the range $10-20\mu$ m. From [4].

to show a much larger density of preexisting defects with respect to the thermally grown SiO_2 on top of silicon bulks. The latter characteristic leads to higher leakage currents, when compared to thermally-grown oxides on silicon [5], [6], and the internal electric fields can be significantly modified by charge build-up, further limiting the expected device performance and reliability [7].

For this reason, a detailed knowledge of charge injection and transport mechanisms of such materials under high electric fields plays a key role in improving the reliability of such devices. Concerning conduction, since very few free charges are present in the conduction band of an insulator at equilibrium, electrons usually are supplied by the cathode contact and a high electric field is necessary for an appreciable leakage current to flow through the insulator. Thus, transport in the oxide is usually referred to as injection-limited conduction [8]. There are three most relevant mechanisms giving rise to the injection-limited current contribution. They are sketched in Fig. 1.2. The thermionic emission, which consists in the classical emission over the metal-insulator barrier and has an exponential increase with the temperature, is due to the classical contribution of electrons with energy larger than the barrier energy between the metal and the insulator. In metal-insulator interfaces, where a high energy barrier is typically present its contribution is negligibly small if compared to the other contributions. The Fowler-Nordheim tunneling is the injection through the energetic barrier, which usually becomes relevant at high electric fields and usually is the most relevant contribution in SiO_2 due to the quite high metal-insulator barrier. The last injection

mechanism is the thermionic-field emission which consists of a combination of a thermal excitation and subsequent tunneling through a thinner barrier.

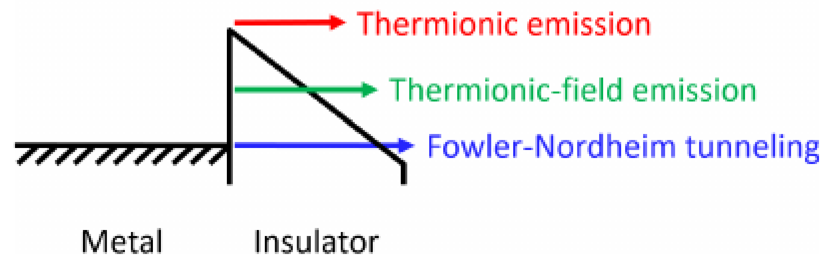

Figure 1.2: Energy band diagram representation of injection-limited conduction mechanisms: thermionic emission, thermionic-field emission and Fowler-Nordheim tunneling. From [8].

A second important contribution to the leakage current in insulators is the so called bulk-limited current [8], which is due to a combination of three mechanisms: ohmic conduction where the current is mainly driven by the mobile charge carriers being intrinsically present in the material, space-charge limited current (SCLC) which is due to fixed charges in the material and trap-assisted conduction which arises from the emission of carrier from traps lying in the energy band gap of the insulator. In particular, emission mechanisms from traps play an important role in amorphous materials like TEOS SiO_2 [8].

Concerning defects, in the last decades trapping phenomena have been investigated by different experimental techniques and many different types of traps in SiO_2 can be found in the literature [9]–[11]. Defects typically present in SiO_2 have been extensively investigated also theoretically [12]. However, it should be noted that the exact nature of the defects present in this material is process-dependent, so even if it was possible to have an overall estimation, it is difficult to determine their energy levels and cross sections unambiguously. Moreover, the majority of the analyses on oxide traps in the literature address the role of defects in thin gate oxides which feature the presence of silicon at least at one side of the oxide layer, thus Si/SiO_2 near-interface properties are investigated rather than bulk properties [13], [14]. Regarding bulk SiO_2, researchers had to rely on theoretical calculations in order to determine the density distribution and position of the traps as they are difficult to be measured [15].

In several models, the charge trapping process has often been treated using phenomenological approaches [16] for calculating the capture and emission rates, but their physical formulations often relies on simplified assumptions [17]. In order to obtain reliable physics-based results, an atomistic modeling approach for the defects must be adopted. For this reason, the defects in the dielectrics were also investigated theoretically in numerous density functional theory (DFT) studies [18]. Among them, the approach with the most interesting results is the one developed by Goes et al. [12] in the framework of the non-radiative multi-phonon (NMP) theory. In [12], atomistic DFT simulations were performed on realistic amorphous structures, where variations in the bond length and angles allow for new defect structures. Using these approaches, the authors were able to extract the parameters, such as the trap levels, to be used in a TCAD model and compare them with the findings from time-dependent dielectric spectroscopy (TDDS) measurements.

As far as the physical mechanisms responsible for the breakdown are concerned, the focus has been on very thin films ($1 - 10$ nm) [19], such as gate oxide structures in CMOS technologies, whereas, for low-k interconnect dielectrics, the thicknesses of interest are on the order of 100 nm [20]. It is widely accepted that breakdown in very thin oxides is due to the formation of percolation paths connecting cathode and anode caused by the generation of defects in the bulk oxide [21]. Viceversa, in thicker oxides it has been shown that impact ionization plays a relevant role in the definition of the breakdown. This is confirmed by some works on devices with oxide thickness in the range of $10 - 100$ nm [22], [23]. However, very limited data presently exist on the breakdown of very thick ($1 - 10\mu$ m) silicon oxide films deposited by state-of-the-art CVD techniques. The characteristics of such thick films are of great interest because they influence both the performances and the reliability of their intended applications where they must withstand several thousand volts [4].

Since stacked dielectrics have long been used in commercial products, the reliability of the technology is empirically well established. Specifically, the reliability of the technology for specific applications are well documented and validated by experimental data. This promising technology, however, will have new applications (or the voltage rating will be further increased for the emerging applications), provided that we can interpret the empirical data within a self-consistent theoretical and experimental framework. Indeed, a fundamental understanding of DC, AC, and thickness-dependent dielectric breakdown of stacked TEOS capacitors, will frame its properties

in the broader context of time-dependent dielectric breakdown (TDDB) characterization of dielectrics and will encourage the diversified use of the core technology.

Dielectric breakdown has a long history with broad implications for technology as it occurs in almost every device as a failure condition as it is an irreversible process. TDDB is a failure mechanism that occurs when a device breaks down as a result of a long-time application of a relatively low but constant electric field (as opposed to direct breakdown, which is caused by the increase of the electric field until the failure of the device). TDDB involves breaking Si-O bonds in a bulk insulator which does not relax and hence defects continue to build up accumulatively throughout the lifetime of the operation of the device. For this reason it has a stochastic nature and thus each device in a circuit may have different breakdown times. The net reliability of the circuit is then dependent on the reliability of the least reliable device. Hence, the understanding of the statistical distribution (Weibull distribution) of the failure times is very essential because the upper values may be orders of magnitude different from the lower values. For this specific reliability analysis, the average values have no meaning. Also, the measurement of TDDB and the application of accelerating stresses is difficult due to non-linear nature of the involved phenomena. Therefore an accurate physical model of dielectric breakdown mechanisms is essential along with accurate measurement techniques for the development of reliable dielectrics [24].

For such reasons, a TCAD-based model of charge transport capable of correctly handling charge injection, trapping and de-trapping mechanisms and avalanche onset in bulk SiO_2 oxides is highly desirable as it would be a key instrument for the development and optimization of ultra-compact capacitances in integrated high-voltage systems. The TCAD framework would allow for the study of the full stack of materials once they are appropriately modeled. Thus, the goal of this work is to provide an efficient TCAD model for SiO_2 which captures the most important physical mechanisms responsible for the leakage current. For this purpose, thick back-end MIM structures have been characterized under DC and AC regimes and the main transport features concerning traps have been extrapolated and modeled them in a TCAD setup.

In this thesis, a TCAD approach for the investigation of charge transport in amorphous silicon dioxide is presented for the first time. The core of my research has been to investigate and model the most relevant physical mechanisms responsible for conduction in silicon oxide. The role of charge

injection at contacts and charge build-up due to trapping and de-trapping mechanisms in the bulk of the oxide layer has been investigated to the purpose of understanding the oxide behavior under DC and AC stress conditions. Starting from a drift-diffusion model for charge transport, the role of defects has been extensively investigated and then modeled by using a first-order kinetic equation to account for trapping and de-trapping dynamics. The spatial and energetic distribution of traps have been also modeled and properly calibrated. In addition, oxide breakdown due to impact-ionization of carriers has been taken into account in order to have a complete representation of the oxide behavior at very high fields. Numerical simulations have been compared against experiments to quantitatively validate the proposed approach. Different models have been proposed in the past years, but the analysis were carried out on old-generation thermal oxides or were based on simplified approaches where particular physical processes dominate. To our knowledge, no attempts have been made to develop a complete model for charge transport in insulator for device simulation. Besides, the research work has focused on the study of the breakdown in realistic 2-D structures, which exhibit a peculiar stress- and thickness-dependent behavior. For this reason, the proposed approach has been applied to simulate the breakdown under different stress conditions. In particular, the effect of the geometry of the devices on the breakdown has been analyzed.

Therefore, this thesis is organized as follows:

- **Chapter 2** is divided in two parts. The first part presents the physical, chemical and transport properties of amorphous SiO_2. A section is dedicated to the high-field transport and breakdown in SiO_2. The second part provides a brief review of the theoretical models for charge transport in insulators and an introduction to the semiclassical transport in semiconductor devices. In particular, the drift-diffusion transport model, generation-recombination processes and trap dynamics are explained. A section is dedicated to a general introduction to numerical simulations of insulators.

- **Chapter 3** is dedicated to the experimental characterization of TEOS structures: in the first part the experimental setup is presented, while in the second part the measurements carried out both on simple test structures and on the target device are reported.

- **Chapter 4** presents the TCAD modeling of SiO_2 with particular focus on the most relevant physical mechanisms responsible for the breakdown in thick MIM structures. The first part is dedicated to the presentation of the models used in our TCAD setup to describe all the relevant physical mechanisms. In the second part the validity of the proposed approach is validated against experiments.
- **Chapter 5** provides a detailed analysis of the thickness-dependent breakdown in realistic 2D-structures with particular focus on geometry-related effects.
- **Chapter 6** finally summarizes the conclusions of the activity.

Chapter 2

Theory

The first part of this chapter is dedicated to the description of the main physical, chemical and transport properties of silicon dioxide. In the first section, the atomic structures of crystalline and amorphous SiO_2 are described in detail. The second section is dedicated to the presentation of the electronic structure of α-SiO_2 which is the crystalline form closer to the amorphous phase of SiO_2. In the third section, the most relevant features of high-field transport in SiO_2 are presented. In the second part of this chapter, a brief review of the of the theoretical models for the conduction mechanisms in insulator is presented. The third part of this chapter is dedicated to the description of transport the semi-classical description of charge transport in semiconductor devices that can be addressed by using the drift-diffusion (DD) model. This model can be derived from the Maxwell equations assuming that the current density is the sum of two contributions: a drift term which accounts for the Ohmic conduction and a diffusion term which takes into account the movement of charges due to a gradient of concentration from a region with higher carrier concentration to a region with lower concentration. The main generation-recombination processes are then discussed with a special focus on the impact-ionization generation which is responsible for the breakdown of MIM structures when a very high bias is applied. In the last part of this chapter the rate equations for traps are discussed and the detailed balance condition is presented.

2.1 Silicon Oxide

SiO_2 is widely used as thin film material in the electronic industry. It has many excellent properties such as anti-resistance, hardness, corrosion resistance, dielectric, optical transparency etc. Silicon dioxide is a material of very

considerable technological importance, including its application in microelectronic devices being widely used as the most common insulator. Continuing improvement in device density and performance has significantly impacted the feature size and complexity of the wiring structure for on-chip interconnects. The gate oxides and capacitor dielectrics have gone through various innovative changes over the years to follow the Moore's law of scaling in integrated circuits. As the minimum device dimensions constantly reduce, the increase in propagation delay, crosstalk noise, and power dissipation of the interconnect structure become limiting factors for ultra-large-scale integration (ULSI) of integrated circuits. To address these problems, new materials used as metal lines and alternative architectures are being developed, thus requiring the introduction of different kinds of insulating materials, like high-k oxides for the gate dielectric and low-k materials for the inter-layer dielectrics [25]. Inter-level dielectric materials need to meet stringent material property requirements for successful integration into the conventional interconnect structures. These requirements are based on electrical properties, thermal stability, thermomechanical and thermal stress properties, chemical stability and low costs. The desired electrical properties are not only low dielectric constant, but also low dielectric loss and leakage current, and high breakdown voltage. Many materials have been recently tested that satisfy these electrical criteria, but the dimensional stability, thermal and chemical stability, mechanical strength, and thermal conductivity are inferior to those of SiO_2 [26]. Finding realistic candidates meeting such requirements is still a major challenge by itself as they require ideal bulk properties as well as ideal interfaces with minimum amount of defects [25]. For these reasons, SiO_2 is expected to continue to be the main insulator in the next future, especially as thick inter-level dielectric layer for power applications. Hence, especially in recent years, experimental and theoretical investigations have focused on microscopic properties of this material and its reliability issues.

2.1.1 Atomic structure of SiO_2

Silicon dioxide (SiO_2) is a compound formed by an atom of silicon and two of oxygen. Due to the greater electronegativity of oxygen with respect to that of silicon, the Si-O bonds show characteristics of both covalent and ionic bonds. The molecular structure of SiO_2 is shown in Fig. 2.1. Since Si-O double bonds are relatively weak with respect to Si-O single bonds due to a poor overlap of the p-orbitals, SiO_2 is a polymeric solid containing four Si-O single bonds

per silicon atom; molecular SiO_2 containing two Si-O double bonds would polymerize [27].

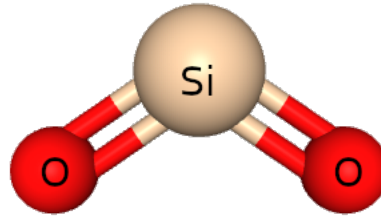

Figure 2.1: Schematic representation of the SiO_2 molecule.

SiO_2 is known to exist in more than ten allotropic modifications, including the amorphous state. With the exception of stishovite, with its silicon atom coordinated by six oxygen atoms, in all other modifications the silicon atom possesses a tetrahedral configuration [28]. The tetrahedral structure of SiO_2 is schematically represented in Fig. 2.2. The various forms of SiO_2 are obtained by linking the tetrahedra together in different ways.

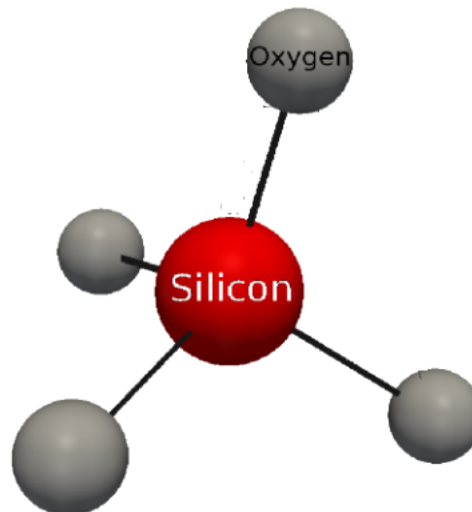

Figure 2.2: Schematic representation of the tetrahedral structure of SiO_2.

Experimental evidence shows that both in its crystalline and amorphous states the structure of tetrahedral modifications of SiO_2 is described by the octahedral Mott rule [29]:

$$\text{Coordination number} = 8 - N$$

According to this rule, the silicon atom is coordinated by four oxygen atoms, and the oxygen atom is coordinated by two silicon atoms. The valence shell configurations of the silicon and oxygen atoms are respectively as follows:

$$Si : 3s^2 3p^2 \qquad \text{and} \qquad O : 2s^2 2p^4$$

The Si-O bond is formed by Si $3sp^3$ bonding orbitals and O $2p$ orbitals. As follows from theoretical calculations, the top of the valence band of SiO_2 is formed by a narrow band of the O $2p_\pi$ non bonding orbitals. By now, it has been found that not only the Si $3s, p$ orbitals but also the $3d$ orbitals of silicon contribute to the formation of the top of the valence band of SiO_2.

The two forms which are the most common and the most studied are the crystalline α-quartz and the amorphous a-SiO_2. Crystalline quartz is characterized by the translational symmetry and long-range order in the arrangement of atoms. In amorphous SiO_2 there is only a short-range order. The experimental X-ray emission spectra and quantum yield spectra of the crystalline quartz and the amorphous phase are very similar [29]. The reflection spectra of α-quartz and amorphous SiO_2 are shown in Fig. 2.3. The two spectra are quite similar, which indicates that the overall electronic structures of α-SiO_2 and the amorphous phase are quite similar [30]. The only difference is that in amorphous SiO_2, Van Hove singularities are slightly broadened compared to crystalline α-quartz. Thus, although there is no long-range order in amorphous silicon dioxide, its electronic structure is similar to the electronic structure of crystalline quartz.

The atomic density radial distribution function (RDF) obtained from X-ray scattering suggests that the atomic arrangement remains correlated (or short-range ordered) within three coordination spheres. What mainly distinguishes the amorphous state from the crystalline state is that the values of the dihedral Si-O-Si angle, the tetrahedral O-Si-O angle, and the Si-O interatomic distance have a random distribution, but their mean values are about the same as in α-quartz. The basic short-range order characteristics of amorphous SiO_2 are the same no matter how oxides are obtained [30]. The Si-O bond length, O-O distance, and Si-Si distance in α-SiO_2 are 0.164 nm, 0.263 nm, and 0.310 nm, respectively. A fragment of the relative arrangement of silicon and oxygen atoms in the SiO_2 tetrahedral structure is shown in Fig. 2.4. The relative position of the oxygen atoms is characterized by the value of the O-Si-O tetrahedral angle Ψ. The relative position of tetrahedrons is specified by the value of the Si-O-Si dihedral angle θ. The average value of

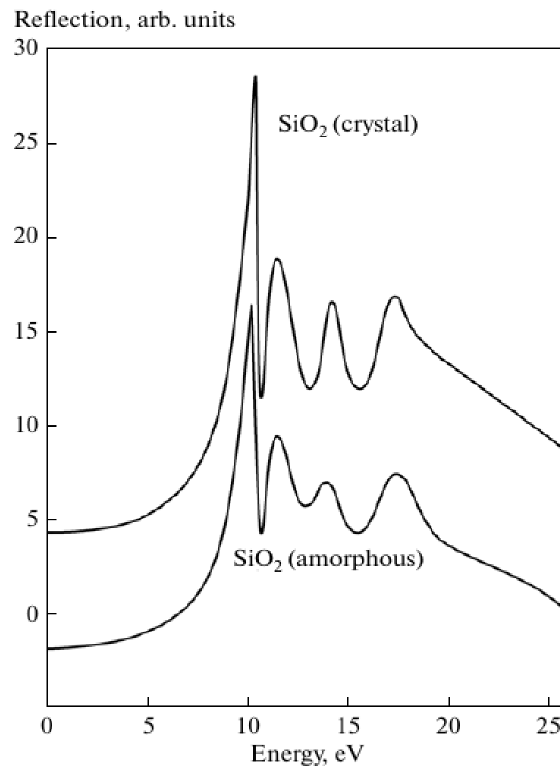

Figure 2.3: Reflection spectra of amorphous SiO_2 and α-quartz. From [31].

105° found for the O-Si-O tetrahedral angle Ψ in dry and wet thermal oxides (amorphous phase) is close to the value of 109° for an ideal tetrahedron. The dihedral angle θ (Si-O-Si angle) averages in the range of $110^\circ - 120^\circ$. The dihedral angle of SiO_2 fluctuates between 100° and 180°.

2.1.2 Electronic structure

There has been an extensive amount of experimental and theoretical work on SiO_2 in order to gain insight into its electronic structure. Nonetheless, some features of the electronic structure of SiO_2 remain unclear [29], [30]. Amorphous SiO_2 is believed to show similar band-structure properties to α-quartz, and techniques used for determining the behavior of α-quartz have also been applied to the more disordered structure of SiO_2 [32]. For a detailed understanding of the electronic structure of SiO_2 and the changes brought by disorder, it is clear that the theoretical calculations of its electronic structure and ad-hoc experiments are indispensable [30].

In Fig. 2.5, the first Brillouin zone of α-SiO_2 is shown.

According to experimental X-ray emission spectra and theoretical calculations, α-SiO2 is an indirect band-gap insulator with the valence band top at

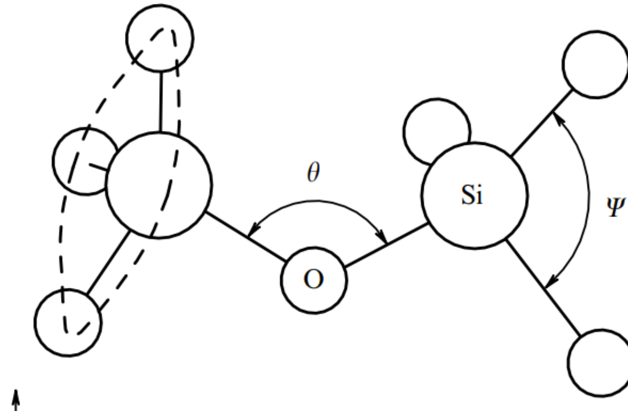

Figure 2.4: Fragment consisting of two SiO_2 tetrahedra: Ψ, O-Si-O tetrahedral angle; θ, Si-O-Si dihedral angle. From [28].

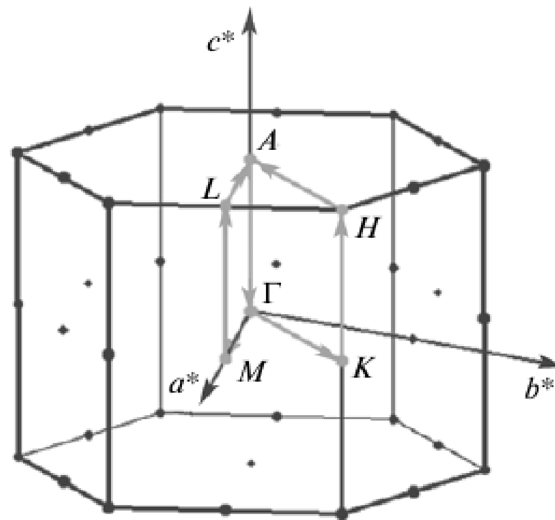

Figure 2.5: Representation of the first Brillouin zone in α-SiO_2. From [29].

the K point and with the conduction band bottom at the Γ point, as shown in Fig. 2.6. The valence band of silicon dioxide consists of two sub-bands separated by an ionic gap. The lower narrow band is formed from the O 2*s* states with an admixture of the Si 3*s* and Si 3*p* states [29]. A band gap of 8.9 eV has been deduced for *a*-SiO_2, and a comparison with α-quartz shows the band gap in α-quartz to be $\approx$ 0.5 eV larger than in *a*-SiO_2 [30].

Theoretical calculations shows that the electron effective mass tensor is isotropic; the electron effective mass is equal to $\approx 0.5m_0$. The hole effective mass tensor, on the contrary, is anisotropic. The hole effective mass along the prism of the first Brillouin zone is equal to $\approx 1.3m_0$; in the direction perpendicular to the axis of the prism, there are heavy holes with the effective mass

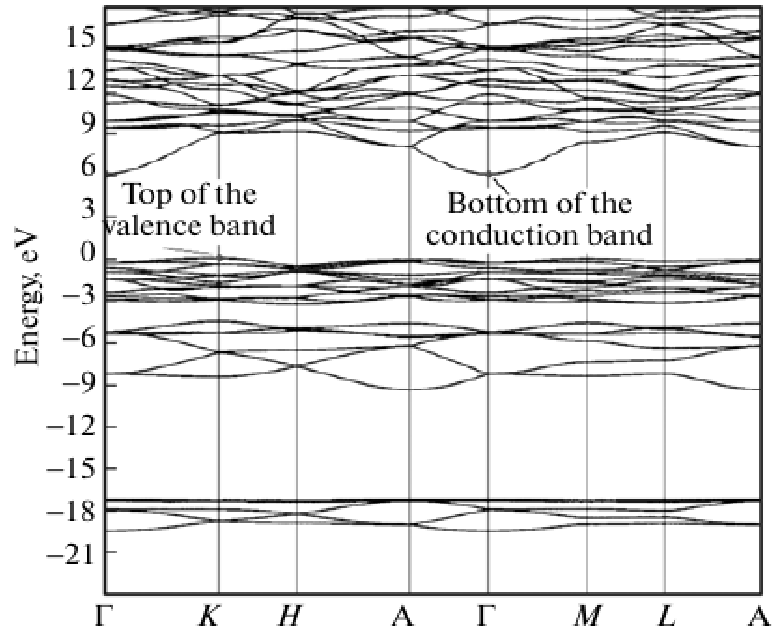

Figure 2.6: Dependence of the energy on the quasi-momentum in α-SiO_2. From [29].

of $\approx 7.0m_0$ [29].

2.1.3 High-field transport

Dramatic device failures such as dielectric breakdown, are probably related to the high flow of energetic electrons in the SiO_2 conduction band. Thus, the understanding of the mechanisms which lead to the degradation and breakdown of the devices is strictly dependent on the understanding of the mechanism of transport and energy loss of electrons in the SiO_2.

In a crystalline solid, the scattering mechanisms for electrons that are typically present are: the electron-phonon interaction, electron-electron scattering and the scattering from charged impurities. Among the various scattering mechanisms controlling the transport of electrons in a solid, typically only the electron-phonon interaction is considered [33]. The electron-electron scattering is negligible because of the very low concentration of carriers present in the SiO_2 conduction band even at very high electric fields. Scattering from charged impurities or defects may be significant, in principle. However, on one hand, it is very difficult to know the exact spatial distribution of these

ionized centers in the oxide. On the other hand, it has been observed experimentally that the average electron energy is independent of the concentration of negative charges trapped in the bulk oxide. Concerning the electron-phonon interactions, electrons can interact with the lattice via polar scattering with optical phonons and via non-polar scattering with both acoustic and optical phonons. The latter is usually dominant in covalent solids, the former in ionic crystals. SiO_2 has a mixed bonding character, so that both interactions should be considered. The major scattering process for electrons in the SiO_2 conduction band at low electric fields is the high-energy longitudinal optical (LO) phonon at 0.153 eV. A second LO phonon exists at a lower energy of 0.063 eV.

In the past, studies on the transport properties of electrons in SiO_2 in high electric fields in very thin gate structures showed that the maximum energy that these electrons can reach with respect to the bottom of the SiO_2 conduction band is about 4 eV [32]. DiMaria and Fischetti investigated the energy distributions of hot carriers in SiO_2 and, together with Monte Carlo simulations, concluded that the lattice interactions were strong enough to prevent the electrons from gaining energies more than 4 eV [34]. This means that the electrons cannot have sufficient energy for collision ionization and hence breakdown was not an impact-ionization phenomenon. However, the strong interaction between the electrons and the polar molecules of the dielectric was assumed to be the only significant mechanism of electron-energy loss. This mechanism is very effective for electron energies comparable to the energy of the longitudinal-optical (LO) phonons of the insulator.

In the last years, sufficient experimental data has been obtained to justify a reconsideration of the interactions taking place in the SiO_2 conduction band at very high electric fields [32]. Some authors have reported a series of experiments showing that electrons in the SiO_2 conduction band can easily gain more energy than predicted before [33]. Experiments have shown that at electric fields of the order of 1 MV/cm, electron scattering with non-polar or acoustic phonon modes must be considered. At sufficiently high electron velocities, the lattice can no longer follow the motion of the electrons and the rate at which the electrons lose their energy in polarizing the lattice decreases as the electron energy increases. There exists a critical field above which most of the electrons gain more energy from the electric field than they can lose to the lattice polarization waves. In this situation, usually referred to as "velocity runaway", the electron energy increases without limit to the maximum applied voltage; that is, there is no steady-state solution of

the electron-transport equation [33]. This is considered to be the threshold of dielectric breakdown, since the very energetic electrons can now impact-ionize the molecular bonds via impact-ionization scattering, thus causing an avalanche multiplication process which would eventually disrupt the lattice.

2.2 Conduction mechanisms in insulators

The conduction mechanisms in insulators are quite different from those in conductors. In insulators, electrons are tightly bound to their atoms and have very little mobility. Hence, very few free charges are present in the conduction band of an insulator at equilibrium and usually they must be supplied by a cathode contact in strong electric field for an appreciable current to flow in the insulator.

Among the conduction mechanisms being investigated, some depend on the electrical properties at the electrode-dielectric contact. These conduction mechanisms are called injection-limited conduction mechanisms. Injection-limited mechanisms include Fowler-Nordheim tunneling, thermionic emission, and thermionic-field emission. There are other conduction mechanisms which depend only on the properties of the dielectric itself. These conduction mechanisms are called bulk-limited conduction mechanisms [8]. Important bulk-limited conduction mechanisms include Ohmic conduction, space-charge limited conduction, trap-assisted conduction and ionic conduction. These conduction mechanisms are discussed next in the context of electron transport. Insulator hole transport is possible, but less common and will not be discussed herein.

2.2.1 Injection-limited conduction mechanisms

The injection-limited conduction mechanisms depend on the electrical properties at the electrode-dielectric contact. The most important parameter in this type of conduction mechanism is the barrier height at the electrode-insulator interface. Aside from it, another key factor in the injection-limited conduction mechanisms is the effective tunneling mass [35].

Thermionic emission

The thermionic (or Schottky) emission refers to electrons in the metal gaining enough thermal energy to surmount the energy barrier at the metal-insulator interface being inject into the insulator conduction band. Fig. 2.7 depicts an

energy band diagram for a metal-insulator interface exhibiting thermionic emission under an applied bias.

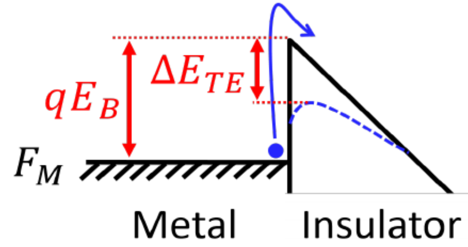

Figure 2.7: Energy band diagram of the thermionic emission in a metal-insulator-metal structure. The blue dashed line represents the barrier lowering due to the Schottky effect.

Depending on the magnitude of the applied voltage, the energy barrier height at the metal-dielectric interface may be lowered by the image force, an effect called Schottky effect. The thermionic emission becomes relevant especially at high temperatures because it has an exponential increase with temperature. It should be noted that, in typical metal-insulator interfaces, where a high energy barrier is typically present, its contribution is small and the tunneling mechanism is expected to dominate. The current density due to the thermionic emission, J_{TE} can be expressed as a function of the applied electric field F by [36]:

$$J_{TE} = A^* T^2 \exp\left(-\frac{E_B - \Delta E_{TE}}{k_B T}\right) \tag{2.1}$$

where A^* is the effective Richardson constant, E_B is the barrier height and ΔE_{TE} is the image-force barrier lowering which is calculated as:

$$\Delta E_{TE} = q\sqrt{\frac{qF}{4\pi\varepsilon_\infty}} \tag{2.2}$$

with ε_∞ the high-frequency dielectric constant of the insulator.

Fowler-Nordheim tunneling

At a high electric field, the thickness of the barrier between the cathode metal Fermi level and the insulator conduction band minimum becomes thin enough to allow the electron to tunnel through the barrier. Thus, Fowler-Nordheim tunneling depends strongly on the applied electric field. Figure 2.12 shows an energy band diagram representation of Fowler-Nordheim tunneling.

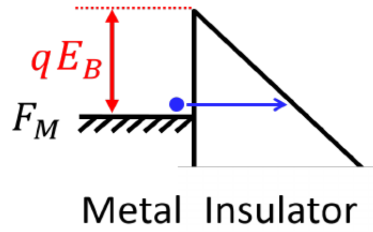

Figure 2.8: Energy band diagram of the Fowler-Nordheim tunneling mechanism in a metal-insulator-metal structure.

The current density due to Fowler-Nordheim tunneling is given by [37]:

$$J_{FN} = \frac{q^4F^2}{16\pi^2\hbar E_B}(\frac{m_0}{m_T})\exp\left(-\frac{4(2m_T)^{1/2}E_B^{3/2}}{3q\hbar F}\right) \tag{2.3}$$

where $\hbar$ is the reduced Planck constant, m_0 is the electron rest mass and m_T the electron tunneling effective mass in the dielectric. The Fowler-Nordheim current density is more sensitive to variation in E_B compared to m_T. It is worth noting that the tunneling effective mass m_T appearing in Eq. 2.3 converges to the electron effective mass in the dielectric for oxide thicknesses larger than few nm [38].

Thermionic-field emission

As schematically shown in Fig. 2.9, the mechanism of thermionic-field emission is most simply represented as a two-step process: it consists of a combination of a thermal excitation and subsequent tunneling through a thinner barrier. In the initial state, the electron has an energy between the Fermi level of the metal and the conduction band of the dielectric. Then it gains thermal energy moving to a higher energy state and subsequently tunnels through a thinner barrier into the insulator conduction band.

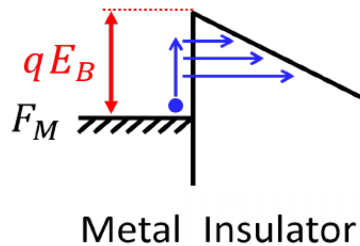

Figure 2.9: Energy band diagram of the thermionic-field emission mechanism in a metal-insulator-metal structure.

The analytical expression for the current density due to thermionic-field emission is given by [39]:

$$J_{TFE} = \frac{q^2(k_B T m_T)^{1/2} F}{8\hbar^2 \pi^{5/2}} \exp\left(-\frac{E_B}{k_B T}\right) \exp\left(-\frac{\hbar^2 q^2 F^2}{24 m_T (k_B T)^3}\right) \tag{2.4}$$

where the notations are the same as defined before.

2.2.2 Bulk-limited conduction mechanisms

The bulk-limited conduction mechanisms in dielectrics are complex and depend on several factors, including the density of states, the degree of disorder, the connectivity of conducting pathways, the presence of localized states, and the presence of traps or defects. Based on the bulk-limited conduction mechanisms, some important electrical properties of the dielectric films can be extracted, including the trap energy level and the trap density [35]. Several theoretical models have been proposed to explain these properties.

Ohmic conduction

Ohmic conduction is caused by the movement of mobile electrons in the conduction band. The well-known expression of the ohmic current density as a function of the electric field is given by [36]:

$$J_{Ohm} = q \mu_n n F \tag{2.5}$$

where μ is the electron mobility and n the free electron concentration in the conduction band, which can be expressed by:

$$n = N_C \exp\left(-\frac{E_C - E_F}{k_B T}\right) \tag{2.6}$$

with N_C the density of states in the conduction band and E_F the Fermi level of the insulator. A slope of one in a $log(J) - log(F)$ curve is indicative of Ohmic conduction. Since the energy band gap of dielectrics is by definition large, there will be a small number of carriers in the conduction band that may be generated due to the thermal excitation, hence the magnitude of this current is very small and is typically negligible with respect to other conduction mechanisms.

Space-Charge Limited conduction

When electrons are injected from the metal cathode into the insulator, the concentration of injected electrons into the insulator may become greater than the thermal equilibrium concentration of electrons within the insulator conduction band [40]. This results in a build-up of negative electronic charge in the insulator near the metal-insulator interface. This build-up of delocalized negative charge constitutes a space-charge region in the insulator. An electron injected from the metal Fermi level now experiences an electrostatic repulsive force due to the existence of this space-charge region, inhibiting further injection into the insulator conduction band. Experimentally, the signature of SCLC is a $J - V$ curve with a power-law behavior in which $J \propto V^{m+1}$, with $m \geq 1$ a fitting parameter [40]. The case of $m = 1$ corresponds to a trap-free insulator, for which the $J - V$ relationship is given by the Child's law [35]:

$$J_{SCLC} = \frac{9}{8}\varepsilon_r \mu \frac{V^2}{t_{OX}^3} \tag{2.7}$$

where ε_r is the static dielectric constant of the insulator and t_{OX} its thickness. In practice, as traps are typically present in an insulator, the J-V relationship becomes more complicate and the exact expression depends on the energetic and spatial distribution of traps in the insulator. However, in its most general form, the J-V relationship has always the form:

$$J_{SCLC} \propto \mu\varepsilon_r^m \mu \frac{V^{m+1}}{t_{OX}^{2m+1}} \tag{2.8}$$

From this expression, it is clear that the space-charge limited current (SCLC) contribution becomes negligible in thick oxides. Moreover, SCLC is somewhat a puzzling mechanism for contributing to insulator leakage current since the existence of an Ohmic contact at the cathode is required. The conventional definition of an Ohmic contact makes it difficult to ascertain how an Ohmic contact could be formed to a wide bandgap insulator.

Trap-assisted conduction

In its most general form, the term trap-assisted conduction indicates all the processes that involve the trap levels in the insulator band gap . In particular, it actually indicates several distinct physical mechanisms for the emission of the trapped electrons towards the conduction band of the insulator, such as

the Poole-Frenkel effect, the phonon-assisted tunneling and the direct tunneling. A detailed explanation of trapping and de-trapping dynamics and the escape mechanisms of carriers from traps is given in Section 2.5.

Among the trap-assisted conduction mechanisms it is worth mentioning the hopping conduction. Hopping conduction is due to the tunneling effect of trapped electrons "hopping" from one trap site to another one in dielectric films, not directly involving the conduction band. The complete theory of hopping conduction developed by Anderson and Mott takes the name of variable-range hopping theory [41] and takes into account several processes I will not discuss herein. In the case of an electron hopping between two nearby trap states placed at a distance a from each other, the expression of the hopping current density is [41]:

$$J_{Hop} = 2qak_B T n \nu_{ph} \exp\left(-2\alpha a \frac{E}{k_B T}\right) \sinh\left(\frac{qaF}{k_B T}\right) \tag{2.9}$$

where ν_{ph} is a factor depending on the phonon spectrum, α is a decaying factor and E is the difference between the energies of the two trap sites. As suggested by Eq. 2.9, this mechanism becomes relevant only at very high trap densities, i.e., small hopping distances, and for trap levels not distant in energy. In most cases, this process is suppressed by the tunneling emission of electrons from trap states to the conduction band and subsequent capture by another trap state.

Ionic conduction

Ionic conduction occurs when the electric field causes the ions to move through the insulator. Due to the influence of external electric field on defect energy level, the ions may jump over a potential barrier from one defect site to another. The ionic conduction current can be expressed as [35]:

$$J_{ion} = J_0 \exp\left(\frac{qdF}{k_B T} - \frac{E_B}{k_B T}\right) \tag{2.10}$$

where J_0 is the proportional constant, E_B is the potential barrier height and d is the distance between two nearby jumping sites. This mechanism of conduction is more common in materials such as ceramics, glasses, and polymers, which contain charged atoms or molecules that can move in response to an electric field due to their relatively weak inter-molecular bonds. Conversely, in compounds such as the oxides, where molecules are strongly bound

to each other and are not free to move across the material, this mechanism is usually not relevant.

2.3 Drift-Diffusion model

The drift-diffusion model can be derived from Maxwell's equations [42]:

$$\nabla \cdot \mathbf{D} = \rho \tag{2.11}$$
$$\nabla \times \mathbf{H} = \frac{\partial \mathbf{D}}{\partial t} + \mathbf{J} \tag{2.12}$$
$$\nabla \cdot \mathbf{B} = 0 \tag{2.13}$$
$$\nabla \times \mathbf{E} = -\frac{\partial \mathbf{B}}{\partial t} + \mathbf{J} \tag{2.14}$$

with:

$$\mathbf{B} = \mu \mathbf{H} \tag{2.15}$$
$$\mathbf{D} = \varepsilon \mathbf{E} \tag{2.16}$$

where ρ is the charge density, J is the current density and μ and ε are the magnetic permeability and dielectric permittivity in the material, respectively. Taking the divergence of Eq. (2.12) and remembering that $\nabla \cdot \nabla \times \mathbf{H} = 0$, we obtain the continuity equation of the carrier density:

$$\frac{\partial \rho}{\partial t} + \nabla \cdot \mathbf{J} = 0 \tag{2.17}$$

with $\rho = q(p - n + N_D - N_A)$, where N_D and N_A are the donor and acceptor dopant concentrations, respectively, and n (p) is the electron (hole) concentration in the conduction band. In writing the expression of ρ we are implicitly assuming that we are dealing with a crystalline semiconductor. However, as explained more in details in Sec. 2.1, an amorphous insulator like a-SiO_2 can be treated as a wide-band gap semiconductor. Total current density J is the sum of the electron and hole current densities, namely $\mathbf{J} = \mathbf{J}_n + \mathbf{J}_p$. Hence, one can split Eq. (2.17) in two different equations, one for each type of carriers [43], [36]:

$$\frac{\partial n}{\partial t} - \frac{1}{q}\nabla \cdot \mathbf{J}_n = W_n \tag{2.18a}$$

$$\frac{\partial p}{\partial t} + \frac{1}{q}\nabla \cdot \mathbf{J}_p = W_p \tag{2.18b}$$

W_n is the total generation rate for the electrons, namely the difference between the number of electrons entering and leaving the conduction band. It can be expressed as the difference between the generation and recombination rates of the electrons $W_n = G_n - U_n$. Similar considerations can be applied to $W_p = G_p - U_p$ for holes. Assuming that the different generation-recombination processes are uncorrelated and taking the steady state approximation for the trap populations, one finds:

$$U_n - G_n = U_p - G_p = U_{SRH} + U_A + U_{II} + U_D \tag{2.19}$$

where U_{SRH}, U_A, U_{II} and U_D represent the net recombination rates associated to thermal recombination, the Auger recombination, impact-ionization generation and photon- and phonon- induced direct transitions, respectively. Further details about U_{SRH} and U_{II} will be provided in the next Sections. U_D will be neglected since ptical direct transitions are not considered in this study. In addition, it has been assumed that direct phonon-induced transitions are negligible when compared to the trap-assisted counterpart (SRH) due to the large band gap of the material.

In the drift-diffusion picture, the electron and hole current densities can be expressed as:

$$\mathbf{J}_n = q\mu_n n\mathbf{E} + qD_n\nabla n \tag{2.20a}$$

$$\mathbf{J}_p = q\mu_p p\mathbf{E} - qD_p\nabla p \tag{2.20b}$$

where μ_n (μ_p) is the electron (hole) mobility and D_n (D_p) is electron (hole) diffusion coefficient and, in principle, both depend on the electric field. Under non-degenerate conditions (the Boltzmann statistics can be used as an approximaton of the Fermi-Dirac distribution), the Einstein relationship relates these two quantities:

$$D_{n(p)} = \mu_{n(p)}\frac{k_B T}{q} \tag{2.21}$$

where k_B is the Boltzmann constant and T the absolute temperature.

In writing Eq. (2.20) we are implicitly neglecting the magnetic effects ($B = 0$), as no specific role is assumed to be given to the magnetic field application. Otherwise, there would be an additional term containing the magnetic field in the expression of the current densities. The set of equations (2.11), (2.16), (2.17), (2.20) are non-linear first-order partial differential equations in the unknowns $\mathbf{E}$, $\mathbf{D}$, n, p, $\mathbf{J}_n$, $\mathbf{J}_p$. In order to be solved, they must be recast in a more compact form. To do so, we introduce the quasi-static approximation writing the electric field as follows:

$$\mathbf{E} = -\boldsymbol{\nabla}\varphi \tag{2.22}$$

where φ is the electric potential. This approximation is valid in semiconductor devices at the typical operating frequencies. Secondly, we introduce the quasi-Fermi potentials φ_n and φ_p. They are auxiliary functions that generalize the concept of Fermi potential under non-equilibrium conditions. In the equilibrium limit they coincide with the Fermi potential φ_F. In this way we can express the electron and hole concentrations in terms of the quasi-Fermi potentials:

$$n = n_i \exp\left[\frac{q(\varphi - \varphi_n)}{k_B T}\right] \tag{2.23a}$$

$$p = n_i \exp\left[\frac{q(\varphi_p - \varphi)}{k_B T}\right] \tag{2.23b}$$

where n_i is the intrinsic carrier concentration.

Using the Einstein's relations (2.21) and the definitions (2.23), the Poisson equation and the current density equations for electron and holes can be recast in a more suitable form for the numerical simulations of semiconductor devices:

$$-\varepsilon\nabla^2\varphi = q(p - n + N_D - N_A) \tag{2.24}$$

$$\frac{\partial n}{\partial t} + \boldsymbol{\nabla}\cdot(\mu_n n \boldsymbol{\nabla}\varphi_n) = W_n \tag{2.25}$$

$$\frac{\partial p}{\partial t} - \boldsymbol{\nabla}\cdot(\mu_p p \boldsymbol{\nabla}\varphi_p) = W_p \tag{2.26}$$

The set of these three equations constitute the drift-diffusion model.

2.3.1 Boundary conditions

In order to solve the equations of the drift-diffusion transport model, the boundary conditions must be evaluated. A simple closed domain representing a parallel-plate capacitor in which the equations are solved is depicted in Fig. 2.10. There are two types of boundaries: the insulating boundaries (black lines in Fig. 2.10) and the conducting boundaries (magenta lines in Fig. 2.10).

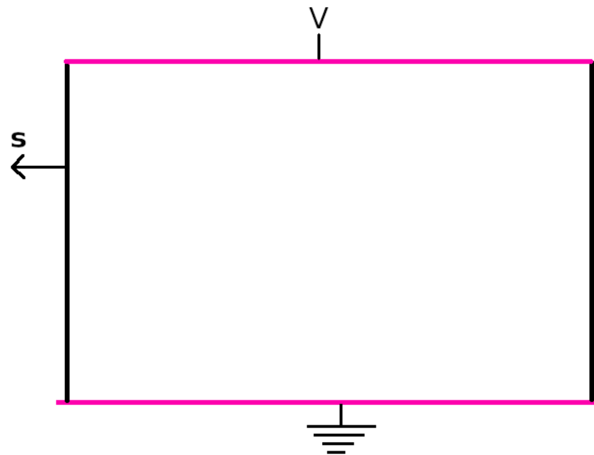

Figure 2.10: Boundary conditions in a device. Black: insulating boundaries. Magenta: conducting boundaries.

There are many possible ways to choose the insulating boundaries. A good choice is such that the electric field normal to them must be zero. These boundaries are also characterized by the fact that no current flows into them, so, calling s a vector perpendicular to an insulating boundary, the scalar product of the electric field E and of the electron and hole current densities J_n and J_p with s must be zero:

$$\mathbf{E} \cdot \mathbf{s} = \mathbf{J_n} \cdot \mathbf{s} = \mathbf{J_p} \cdot \mathbf{s} = 0$$

They are called homogeneous Neumann type boundary conditions.

Concerning the conducting boundaries, unless we are very far from an equilibrium condition, they are able to keep charge neutrality at contacts. Since the contacts are typically connected to voltage generators, as shown in Fig. 2.10, the electric potentials at the contacts φ_C are prescribed and from that it is possible to calculate the electron and hole concentrations at the contacts so that the Poisson and the transport equation can be solved with a unique solution. These boundary conditions are called Dirichlet type.

2.4 Generation Recombination processes

Inter-band generation-recombination processes allow the transition of electrons from the valence to the conduction band and vice-versa. We can distinguish between trap-assisted and direct processes. In the former case, the transition is assisted by the presence of trap levels into the band gap which originate from defects in the bulk of the semiconductor (Schockley-Read-Hall theory), while the latter occurs directly between the two bands (Auger recombination, impact-ionization generation).

2.4.1 Schockley-Read-Hall recombination

The Schockley-Read-Hall (SRH) recombination describes the trap-assisted thermal recombination assuming the presence of a single trap level with energy E_T and a steady-state condition. If more than one level is present, the contributions of the individual levels should be summed at the end of the calculation. However, it can be shown that the most efficient value of E_T is located approximately at the mid-gap and the other trap levels can be neglected. It is usually expressed as:

$$U_{SRH} = \frac{np - n_{eq} p_{eq}}{\tau_{p0}(n + n_B) + \tau_{n0}(p + p_B)} \tag{2.27}$$

where n_{eq} (p_{eq}) and τ_{n0} (τ_{p0}) are the electron (hole) equilibrium concentration and lifetime, respectively, and n_B and p_B are given by the following expressions:

$$n_B = \frac{n_{eq}}{d_T} \exp\left(\frac{E_T - E_F}{k_B T}\right) \tag{2.28a}$$

$$p_B = p_{eq} d_T \exp\left(\frac{E_T - E_F}{k_B T}\right) \tag{2.28b}$$

where E_F is the Fermi energy and d_T the degeneracy coefficient of the trap. An excess of np with respect to equilibrium indicates that recombinations prevails over generation, and vice-versa.

2.4.2 Auger recombination

Two electrons into the conduction band may collide and exchange energy. If at the end of the collision one of the electrons exhibits a loss of energy equal or greater than the energy gap, it experiences a transition into an empty state

of the valence band. The other electron acquires the same amount of energy and goes into a higher energy state in the conduction band. This process is usually called Auger recombination initiated by electrons. Analogue considerations can be made for a collision between two holes into the valence band. The Auger recombination for electron and holes can be written as:

$$U_{An} = c_n n^2 p \tag{2.29a}$$

$$U_{Ap} = c_p p^2 n \tag{2.29b}$$

Where c_n (c_p) is the Auger recombination coefficient for electrons (holes) The probability that two electrons in the conduction band or equivalently two holes in the valence band can collide is usually low at room temperature since the probability of a collision of a charge carrier with phonons is much higher. The Auger recombination becomes relevant only when the carrier concentration is very high. Hence Auger recombination is dominant in heavily doped regions with a high charge density, and as a consequence, low electric field. For this reason it is neglected in our analyses since the electron and hole concentrations are always low due to the large band gap of SiO_2, while the electric fields of interest are very high.

2.4.3 Impact-ionization generation

Impact-ionization transitions occur when an electron whose initial state is in the conduction band at high energy, collides with another electron in the valence band. After the collision, the first electron is still in the conduction band but with a lower energy, while the second one acquires enough energy to a transit into the conduction band. This process is called impact-ionization initiated by electrons. The impact-ionization generation for electron and holes can be written as:

$$U_{IIn} = -I_n n \tag{2.30a}$$

$$U_{IIp} = -I_p p \tag{2.30b}$$

I_n (I_p) is called impact-ionization generation coefficient for electrons (holes). The carrier generation due to impact-ionization occurs only when an electron or a hole acquires an energy larger than the energy gap. This happens only in presence of a strong electric field which provides a sufficient amount of

energy to the charge carrier over a distance much shorter than the mean free path in the material. As a consequence, impact-ionization is dominant in regions with a low doping concentration and a high electric field and for this reason it plays a relevant role in our analyses as discussed in the next Chapters.

Electron-hole pair production due to avalanche generation requires a certain threshold field strength and the possibility for the carriers to accelerate, that is, wide space-charge regions. If the width of a space-charge region is greater than the mean free path between two ionizing impact, charge multiplication occurs, which can cause the electrical breakdown. The reciprocal of the mean free paths are called impact-ionization coefficients α_n and α_p, for electrons and holes, respectively. Their mathematical definition follows by assuming a condition far from equilibrium, when impact-ionization dominates over the other generation-recombination processes. Hence, $U_n - G_n = U_p - G_p \approxeq U_{II} \approxeq -I_n n - I_p p$. Under steady-state conditions, the continuity equations become:

$$\nabla \cdot \mathbf{J}_n = -qnI_n - qpI_p \tag{2.31a}$$

$$\nabla \cdot \mathbf{J}_p = qnI_n + qpI_p \tag{2.31b}$$

Assuming that the conduction term is dominant over the diffusion term due to the high electric field yields to $\mathbf{J}_n \approxeq q\mu_n n\mathbf{E}$ and $\mathbf{J}_p \approxeq q\mu_p p\mathbf{E}$. Rewriting the current densities as $\mathbf{J}_n = J_n\mathbf{e}$ and $\mathbf{J}_p = J_p\mathbf{e}$ where $\mathbf{e} = \mathbf{E}/|\mathbf{E}|$, Eqs. 2.31 become:

$$-\nabla \cdot \mathbf{J}_n = \alpha_n J_n + \alpha_p J_p \tag{2.32a}$$

$$\nabla \cdot \mathbf{J}_p = \alpha_n J_n + \alpha_p J_p \tag{2.32b}$$

where the impact-ionization coefficients are:

$$\alpha_n = \frac{I_n}{\mu_n|\mathbf{E}|} \tag{2.33a}$$

$$\alpha_p = \frac{I_p}{\mu_p|\mathbf{E}|} \tag{2.33b}$$

2.5 Trap dynamics

Traps are important in device physics because they provide doping, enhance recombination, and increase leakage through insulators. Several models, such as the Schockley-Read-Hall (SRH) net recombination, depend on traps implicitly, but do not actually model them. In an amorphous material, like the SiO_2 used in gate structures or in the back-end, energy bands arise instead of discrete trap levels, hence SRH recombination cannot provide a complete description of trap dynamics which can be fully taken into account only using a kinetic equation for the traps occupation. This section is dedicated to the description of the models that take the occupation and the space charge stored on traps explicitly into account.

In Fig. 2.11 a schematic representation of a deep-level impurity in the band gap of an insulator or a semiconductor is reported showing the four different types of recombination event. The event (a) represents the electron capture (or electron trapping) from the conduction band, (b) represents the electron emission in the conduction band, (c) is the hole capture (or hole trapping) from the valence band and (d) represents the hole emission in the valence band. Let us consider the deep-level impurity in Fig. 2.11 with an energy E_T and concentration N_T. The following analysis is carried out for a single impurity level, but in principle it can be extended to multiple energy levels by simply summing all contributions due to each single trap.

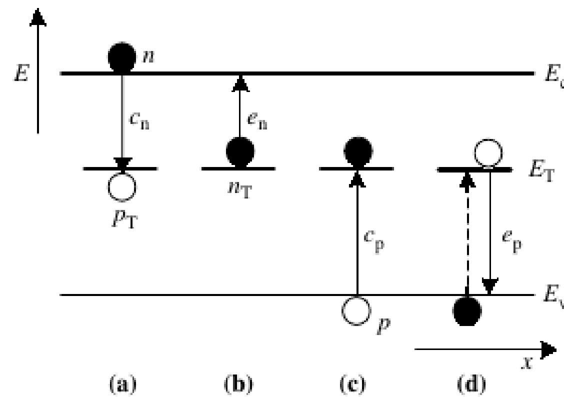

Figure 2.11: Electron energy band diagram for an insulator or a semiconductor with deep-level impurities. From [37].

A recombination event is given by an event (a) followed by (c) and a generation event is (b) followed by (d). Both the conduction and valence bands participate in recombination and generation. Differently, a trapping event is (a) (electron capture from the conduction band) or (c) (hole capture from

the valence band), while a de-trapping event is (b) (electron emission in the conduction band) or (d) (hole emission in the valence band). In either case a carrier is captured or alternatively emitted back to the band from which it came. Only one of the two bands and the defect participate and the impurity is a trap. In the following we will derive the appropriate equations for electrons. The equations for holes are analogous, and their derivation is similar. Hence, we will neglect the processes (c) and (d) of Fig. 2.11. It is a reasonable assumption if trap centers are acceptor-like and the hole concentration p is negligible with respect to the electron concentration n. The electron density in the conduction band is diminished by electron capture and increased by electron emission and the continuity equation for traps is given by [37]:

$$\frac{\partial n}{\partial t} = e_n n_T - c_n n (N_T - n_T) \tag{2.34}$$

Where e_n represents the emission coefficient, c_n is the capture coefficient and n_T is the concentration of filled traps, i.e., the traps that are occupied by an electron. It follows that $N_T - n_T$ represents the concentration of empty defects. It should be highlighted that the emission term does not contain n because the probability to find an empty state in the conduction band for the emitted electron is almost 1, whereas the electron density n in the capture term is important because, to capture electrons, there must be an electron leaving the conduction band.

The capture coefficient c_n is defined by [37]:

$$c_n = \sigma_n v_{th} \tag{2.35}$$

Where v_{th} is the electron thermal velocity and σ_n is the electron capture cross-section of the defect. A physical explanation of c_n can be derived from Eq. 2.35. We know that electrons move randomly at their thermal velocity and that defects remain almost fixed in the lattice. That is equivalent to a the frame of reference in which the electrons are immobile and the defects move at velocity v_{th} . The centers then sweep out a volume per unit time of $\sigma_n v_{th}$. Those electrons that find themselves in that volume have a very high probability of being captured.

Whenever an electron or hole is captured or emitted, the center occupancy changes, and that rate of change is:

$$\frac{\partial n_T}{\partial t} = n v_{th} \sigma_n (N_T - n_T) - n_T e_n \tag{2.36}$$

Eq. 2.36 states that the time rate of change of filled traps n_T is equal to the

difference between the capture and the emission rate. The capture rate is proportional to the density of free electrons, their thermal velocity, the density of unfilled traps and the trap capture cross section. The emission constant e_n can be determined, at least in thermal equilibrium, by assuming the detailed balance in Eq. 2.36, giving [44]:

$$e_n = N_C v_{th} \sigma_n \exp\left(-\frac{E_T}{k_B T}\right) \quad (2.37)$$

Here N_C is the density of conduction-band states. The pre-factor is often referred to as the attempt-to-escape frequency ν_0.

Nearly all the parameters in Eq. 2.37 are affected by high electric fields. In particular, the cross-section σ_n strongly depends on the electric field, and as a consequence the emission rate is field-dependent. Indeed, in the absence of a field, the only escape mechanism for the traps is the thermal emission over the entire trap depth.

The presence of an electric field causes the lowering of the energetic barrier, an effect known as Poole-Frenkel (PF), as shown in Fig. 2.12. The Poole-Frenkel effect is a classical mechanism in which the electron is thermally emitted over the top of a potential barrier which has been lowered by the presence of an electric field. Thus any change in the barrier height is assumed to enter as a correction of E_T in Eq. 2.37. For example, for a Coulombic potential in an electric field F aligned with the z-axis, the potential energy is:

$$V(r) = -\frac{q^2}{4\pi\varepsilon_r\varepsilon_0 r} - qFr\cos(\theta)$$

The well-defined potential maximum is found at $r = r_{max}$:

$$r_{max} = \sqrt{\frac{q}{4\pi\varepsilon_r\varepsilon_0 F\cos(\theta)}}$$

Hence the change in the potential barrier due to the presence of the field ΔE_T is given by:

$$\Delta E_T = V(r_{max}) = -q\sqrt{\frac{qF\cos(\theta)}{\pi\varepsilon_r\varepsilon_0}} \quad (2.38)$$

the well-known one-dimensional result is given by setting $\theta = 0$, whereas the three-dimensional calculation requires an integration over θ which gives rise to a more complicate expression presented in Chapter 4.

Moreover, in the presence of an electric field, carriers can also be emitted by thermal excitation over only a part of the trap followed by tunneling through the remaining potential barrier (PAT in Fig. 2.12). This mechanism is called phonon-assisted tunneling (PAT). The tunneling probability across a potential barrier is given by the following expression in the Wentzel-Kramers-Brillouin (WKB) approximation [45]:

$$\Gamma = \exp\left(-\frac{2}{\hbar}\int_0^r \sqrt{V(x)}dx\right) \tag{2.39}$$

where $V(x)$ is the potential energy relative to the energy of the electron. A trapped electron which absorbs a phonon can tunnel through the barrier at a higher energy, with an enhanced probability Γ_C:

$$\Gamma_C = \exp\left(-\frac{E}{k_B T}\right)\exp\left(-\frac{2}{\hbar}\int_0^r \sqrt{V(x)+E_T-E}dx\right) \tag{2.40}$$

with E_T is the ionization energy of the trap and E is the phonon energy. The total emission probability Γ_{PAT} is given by integrating 2.40 over all phonon energies E:

$$\Gamma_{PAT} = \int_0^{E_T} \Gamma_C dE \tag{2.41}$$

In principle, $V(x)$ can have an arbitrary form, hence the integral over the position x cannot be solved analitically. However, approximate expressions can be obtained for known potentials, giving rise to different models for the PAT emission probability, as explained more in details in Chapter 4.

Alternatively, the electrons can even directly tunnel out of the trapping center across the energetic barrier (TU in Fig. 2.12). At low temperatures and/or for deep trap levels de-trapping may occur by tunneling rather than field-assisted thermal emission, in that case, a field-emission description is appropriate.

These three kinds of electric field-related effects compete during emission, depending on electric field and temperature conditions and they are shown in Fig. 2.12.

To conclude, I would like to point out that, due to these considerations, the analytical solution of Eq. 2.36 is possible only in very simple cases where one or more of the emission-enhanced effects are negligible and in a situation where capture processes are dominant over the emission or vice-versa. Moreover the model can be generalized to include two carriers and multiple traps or a continuous distribution of trap levels. Hence, the numerical

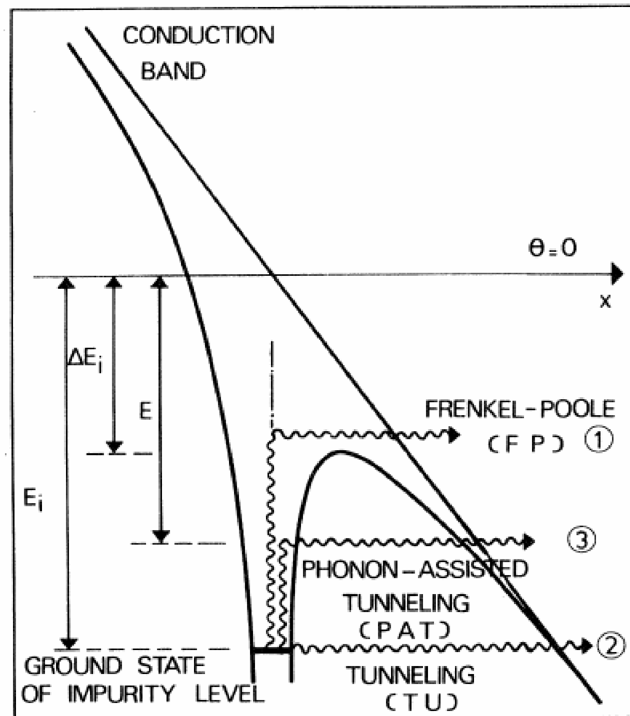

Figure 2.12: Schematic representation of the electric-field-assisted emission mechanisms from a Coulombic well. From [46].

solution of these equations is fundamental to solve these equations.

2.6 TCAD-based numerical simulations

The drift-diffusion model described so far can be solved analytically only in a few simple cases. On the contrary, when the complexity of the device geometry increases, numerical simulations are fundamental to understand the effects of each physical model on the behavior of the device. Different software suites are today available to reproduce the different levels of abstraction, including: process, device and circuit simulations. Process simulations allow to reproduce ion implantation, dopant diffusion and oxidation, etching and lithography steps. However, when the details of the fabrication processes are not relevant to the device analysis and the doping is not present, as in our case, the structure of the device can be recreated in the simulator without process simulations, provided that the geometry is known. This is usually achieved by using specific tools available into the software suite. The recreated device geometry is then used as input for the device simulations in which the drift-diffusion model is solved numerically. The device is divided

into a discretized structure called mesh. Thus each differential equation of the system is solved at each vertex of the mesh. The Poisson equation (Eq. 2.24), the transport equations for electrons and holes (Eq. 2.25 and Eq. 2.26, respectively) and the rate equation for the traps (eq. 2.36 are solved iteratively until the convergence is achieved. The current-voltage (I-V) characteristics can thus be simulated and compared against measurements performed on real devices. In this work, the commercial suite provided by Synopsys Inc. has been used [47]. Process simulations have not been considered since all the information about geometry were already available. Sentaurus Structure Editor has thus been used to define the device and the mesh structure. The electrical characteristics have been simulated through Sentaurus Device which solves numerically the drift-diffusion model.

In conclusion, the most relevant transport mechanisms in amorphous SiO_2 are expected to be the charge injection at the contacts through the tunneling mechanism, charge trapping in defect sites of the bulk oxide and avalanche generation due to the electron impact-ionization which is ascribed to be the physical mechanism causing the breakdown of thick MIM structures. The TCAD tool allows us to have a complete physical representation of the transport properties since many models are already implemented. Concerning the charge injection, tunneling models are already available for metal-semiconductor interfaces. Trapping and de-trapping mechanisms can be taken into account by using a first-order detailed balance equation for each trap as available in the TCAD tool: the model explicitly takes into account the occupation rate of each trap by coupling the capture and emission rates to the conduction and valence band of the SiO_2. In order to properly account for the trapping and de-trapping effects, the Poisson equation can be solved along with the transport and continuity equations of electrons and holes. The trapped charge is explicitly accounted for in the Poisson equation. This approach requires to explicitly define each type of defect, as it will be described in more details in the next chapters, by fixing their energy dependence, their concentration and local distribution and their capture cross-sections. Concerning traps, in principle, also trap-to-trap transport (or hopping) can be modeled in the TCAD tool. However, the available models require a great computational effort, hence they are not suitable for thick-oxide simulations, whereas they can be useful for very thin gate structures. Concerning impact-ionization, several models are implemented in the TCAD tool. Despite they are calibrated for silicon and some other semiconductors and not for insulators, they are a good starting point also for semi-insulating or insulating materials. Among them,

the most relevant for our analyses are the Van Overstraeten-De Man and the Okuto-Crowell models, as discussed in more details in the next chapters.

Chapter 3

Characterization of TEOS MIM structures

The SiO_2 films grown at low temperature have preferably been used as an interlayer dielectric and a final passivation layer in VLSI circuits. PE-CVD has been proved to be a good low-temperature, fast and high-growth rate deposition technique for the growth of SiO_2 films. The most widely used precursors to deposit SiO_2 films are silane and tetraethylorthosilicate (TEOS). However, the handling of silane is very difficult as it is pyrophoric, flammable and toxic. Therefore, TEOS is preferably used as a source of Si, because it is safe and easy to handle as it is in liquid form and chemically stable [48]. The quality of the deposited SiO films is mainly decided by the process parameters chamber pressure, substrate temperature, RF power, mass flow rates, interelectrode spacing and TEOS bubbler temperature. However, deposited dielectrics are generally inferior to thermally grown SiO_2 in terms of electrical properties. Actually, TEOS-SiO_2 is known to provide a high leakage current, substantial oxide fixed charge, and interfacial trapped charge [49]. In order to understand the transport properties of high-voltage capacitors, MIM structures have been realized and characterized. All structures have been provided and characterized by STMicroelectronics. In the first part of this chapter, simple test structures, consisting of parallel plate capacitors, are characterized, in order to gain insight on the most relevant physical mechanisms responsible for conduction in thick oxides. In the second part, the characterization of more complex structures with a 2-D geometry is presented along with a thickness- and stress- dependent breakdown analysis.

3.1 Experimental setup

Measurements on the simple test structures have been carried out at the wafer level. A Keysight B1505 semiconductor parameter analyzer, equipped

with high-voltage (HV) source measurements units (SMU), has been used for the electrical characterization. Bottom electrode has been invariably kept grounded through the wafer chuck. The top electrode of the capacitor is instead connected by a single HV probe and a high voltage triaxial cable to the HV SMU. Trials have been carried on at a controlled temperature at the wafer chuck ranging from 25 °C to 150 °C. Statistical measurements have been performed through an automated probe dedicated to HV measurements (Tesla System for HV, Cascade Microtech inc.). Different stress trials have been performed, as explained more in details in the next sections. Concerning the more complex structures with a 2-D geometry, measurements have been carried out at package level on dedicated chipboards.

3.2 Test structures characteristics

Fig. 3.1 shows a cross section of the high-voltage MIM capacitor. Two planar electrodes define the capacitance: the bottom metal is in titanium nitride (TiN) and is deposited on silicon and grounded, the top metal is in tantalum nitride (TaN) and is grown on top of the sub-sequential inter-metal dielectrics forming the thick insulating region and is biased to positive/negative high voltages. TEOS processes are used for the oxide deposition. The nominal thickness of the capacitor is $t_{OX} = 0.9\ \mu$m. No relevant issues concerning with device variability were observed, thus the characteristics of single samples are used as references for the analyzed curves.

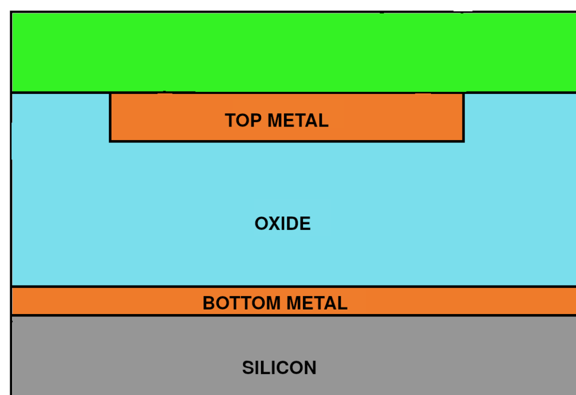

Figure 3.1: Schematic view of the TEOS test structure.

Contacts have a circular shape with a diameter $d \approx 150\ \mu$m. Since $d >> t_{OX}$, one can assume that the device behaves as a parallel plate capacitor. In order to validate this assumption, devices with different perimeter to area

ratio have been measured to obtain the bulk and perimeter current densities at different biases. The comparison between the total current and the areal contribution is reported in Fig. 3.2 where the current density is represented as a function of the applied electric field $F_{OX} = |V|/t_{OX}$, with V the voltage applied at the top electrode. At electric fields over 5.5 MV/cm, the areal contribution dominates over the perimeter one. The areal current contribution has been extracted from the total one by comparing several devices with very different perimeter to area ratios. For this reason, the MIM structure can be modeled as a simple 1-D planar capacitance neglecting the perimeter contribution to the current.

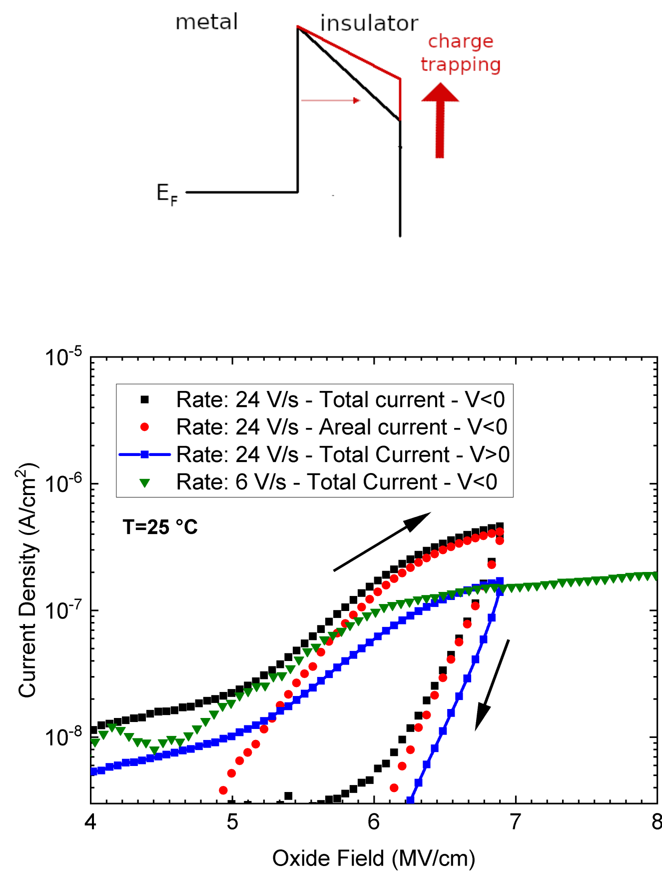

Figure 3.2: Top: Oxide band diagram modifications due to the trapped charge. Charge trapping modifies the internal electric field distribution leading to different injection probabilities between the forward and the backward ramp.
Bottom: Measured current densities as a function of the electric field. Two voltage ramp-rates have been applied, namely 24 V/s and 6 V/s. For the faster ramp measurements with both the polarities are represented.
Black curve(squares): total measured current with negative bias; blue curve (squares): total measured current with positive bias; red curve (circles): areal contribution with negative bias; green curve (triangles): negative bias with ramp rate of 6V/s.

A forward and backward negative voltage ramp has been applied at the top metal with a relatively slow rate: it allows for the study of electron injection from top metal and of charge trapping effects. Measurements with positive and negative biases allow us to study the asymmetry between bottom- and top-contact injection due to the different materials the contacts are made up of. Measurements with two different ramp rates, namely 6 V/s and 24 V/s, have been performed to study the transient charge trapping. The voltage ramp rate has an impact on the filling probability of the traps due to the trapping time constants, which are proportional to the capture cross-sections [37]. A shorter sweeping can avoid or minimize injected carriers to be trapped leading to a larger injection current.

One can observe that the slower ramp of Fig. 3.2 features a significant reduction of the current density at high fields, which can be ascribed to a larger trapping with respect to the faster one. The slow current increase is mostly due to the electric field pinning due to charge trapping at the injecting electrode, reducing the tunneling through the barrier. A relevant hysteresis loop is observed in the curves of Fig. 3.2. The presence of a relevant hysteresis indicates that a great amount of charge has been trapped in the oxide and suggests that the energetic position of the trap levels is placed deep in the oxide band gap. In fact, the electron emission probability from shallower traps would be greater, giving rise to a larger current and resulting in a less pronounced (or even absent) hysteresis. Charge injection slightly changes between the forward and the backward ramp due to the trapped charge which can significantly modify the electric field distribution within the oxide and consequently the band diagram, as shown in the upper diagram of Fig. 3.2. The extracted bulk contribution is compared with the total one: a steep increase of the curves is shown at low fields, in accordance with the expected tunneling injection. The high current in the fast ramp at low fields is a hint that charge injection from the metal contact is dominant over charge trapping effects, which would significantly limit the current level. The lower current measured in the slow ramp case at higher electric fields ($F_{OX} > 5.5$ MV/cm) is ascribed to an enhanced charge trapping mechanism: the slower increase of the voltage bias allows a larger charge trapping within the oxide.

In order to gain insight on the contribution of the thermionic emission to the injected current, the slow ramp characteristics has been measured also at a temperature $T = 100$ °C and $T = 150$ °C. Fig. 3.3 shows the current curves measured at different temperature conditions from $T = 25$ °C to $T = 150$ °C. The temperature dependence is weak, with a limited shift at low electric

fields where the injection contribution is expected to be the dominant one with respect to charge trapping as indicated by Fig. 3.2. Thus, the injected current by tunneling mechanisms plays the main role up to $F_{OX} = 6$ MV/cm.

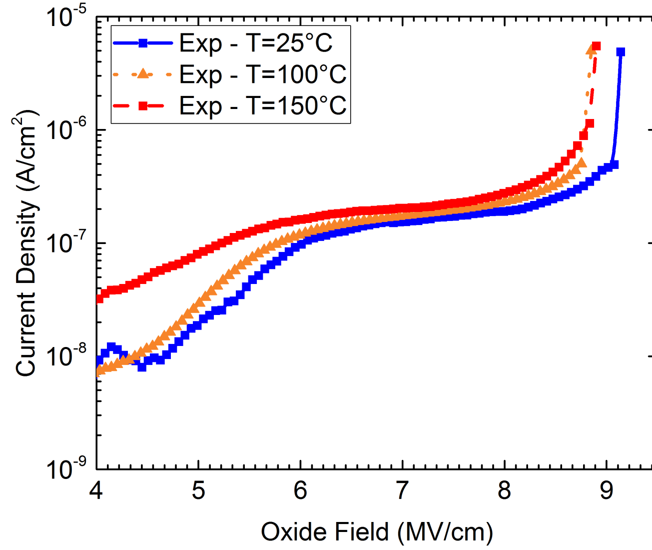

Figure 3.3: Slow voltage ramp measurements at different temperature conditions up to breakdown: $T = 25$ °C, $T = 100$ °C and $T = 150$ °C.

It should be noted that several measurements have been performed on different samples, hence the curves reported in Fig. 3.3 represent an average of the whole set. However, no relevant variability concerning the leakage current has been observed. Concerning the breakdown voltage, the corresponding normal distribution of the breakdown voltage (and field) are shown for the measurements carried out at room temperature in Fig. 3.4.

Finally, measurements under DC and AC stress conditions were carried out in order to assess the role of trapping/detrapping effects in such kind of structures (see Fig. 3.5). The negative DC voltage of -650 V is applied to the MIM structure for a stress time up to 10^4 s. By observing the measured DC current in log scale (Fig. 3.5, inset) a decreasing curve was found, which can be ascribed to charge-trapping transient mechanisms depending on the characteristic capture cross-sections. The DC characteristics are strictly related to the trapping rate, i.e. the capture cross-sections and trap densities, as well as to the trap energy levels: the more charge is trapped, the faster the current will decrease over time. It can be used as a further verification of the calibration of trap parameters after the fitting of the voltage ramp characteristics.

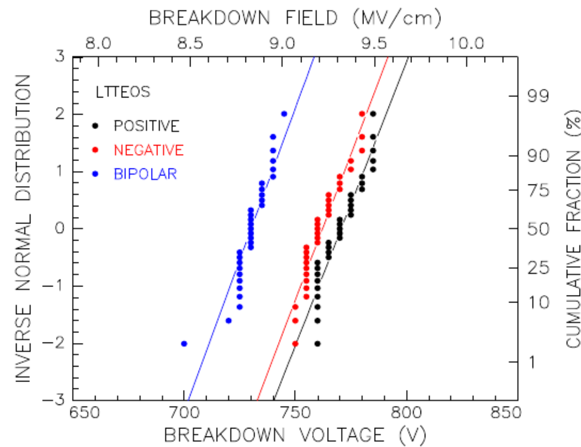

Figure 3.4: Inverse normal distribution of the breakdown voltage (and field) at $T = 25$ °C under DC negative (red), DC positive (black) and AC bipolar (blue) ramps.

The bipolar AC square voltage, with pulses of 650 V and period of 14 s (reported in the leftmost part of Fig. 3.5), is applied to the MIM under study for 120 s. The time delay of the first recorded point after the bias switch has been kept constant to 1 s for the duration of the measurement process. The recorded current transients are reported in Fig. 3.5, the first half-period is negative. In this case, the same trapping transient observed in the DC case appears at the beginning of the first half-period, followed by a relevant detrapping transient significantly increasing the current at the beginning of the positive half-period. A clear asymmetry is observed in the trapping transients, which can be ascribed to different metal/oxide interfaces for the top and bottom electrodes. An average current density at long stress times is found which seems to reach a regime condition in the last few periods.

We cannot exclude that defect generation may be present during the applied stress. Nevertheless, the regular periodic behavior reached after the first few periods is a clear hint that the defects eventually generated at the longest stress times produce negligible effects in the current transients. Detrapping mechanisms show a fast recovery which needs to be accurately accounted for.

3.2.1 Breakdown under different stress conditions

In order to gain insight on the main physical mechanisms responsible for the breakdown of TEOS capacitors, constant current stresses have been applied to the test structure under study at different temperatures until the breakdown condition was reached measuring the voltage at the top contact. For

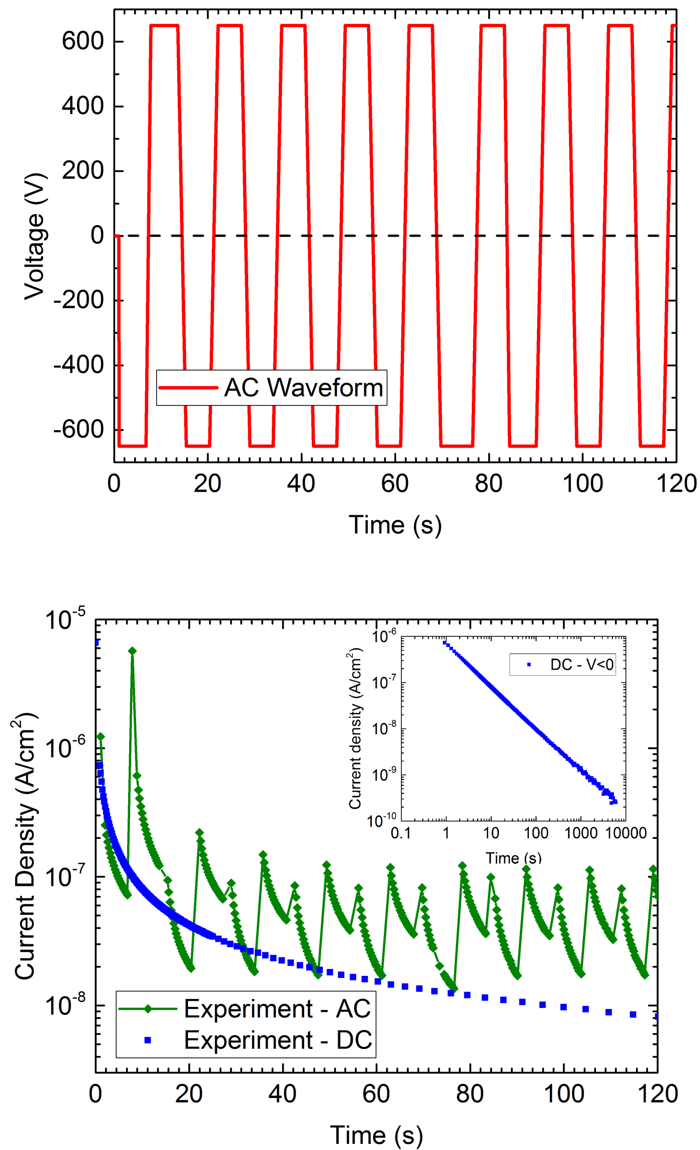

Figure 3.5: Left: AC stress applied voltage. The amplitude is 650 V and the period is 14 s.
Right: Current versus time semi-log plot of the AC (lines+symbols) and negative polarity DC (symbols) characteristics. The first semiperiod of the AC characteristics has negative polarity. Inset: log-log current plot of the DC measurements.

each temperature, three targets of current density have been used as reported in Table 3.1.

Forcing current directly through the capacitor leads to very long voltage rise-times, as $dV/dt = I/C$, with I the current flowing through the insulator which is very low, C the capacity of the MIM and V the applied bias. To avoid this issue, the following approach is used: at $t = 0$, a constant voltage

Table 3.1: Temperature conditions and current density targets used in experiments.

Temperature	J_1 (A/cm^2)	J_2 (A/cm^2)	J_3 (A/cm^2)
T=25 °C	$1.4 \cdot 10^{-8}$	$3.0 \cdot 10^{-8}$	$6.3 \cdot 10^{-8}$
T=150 °C	$1.6 \cdot 10^{-8}$	$3.6 \cdot 10^{-8}$	$7.5 \cdot 10^{-8}$

is applied to the capacitor, the current is measured and considered as the target current level. In order to avoid current reduction due to charge trapping, a small voltage ramp is applied at fixed time intervals of 10s, as shown in Fig. 3.6. The new voltage required to force the target current I_t is thus found and set. Between two consecutive voltage settings, the current flowing through the capacitor slightly deviates from I_t. However, it was checked that deviations from I_t are small and this approach fully overcomes the problem of the long charging transients of standard constant-current stress experiments.

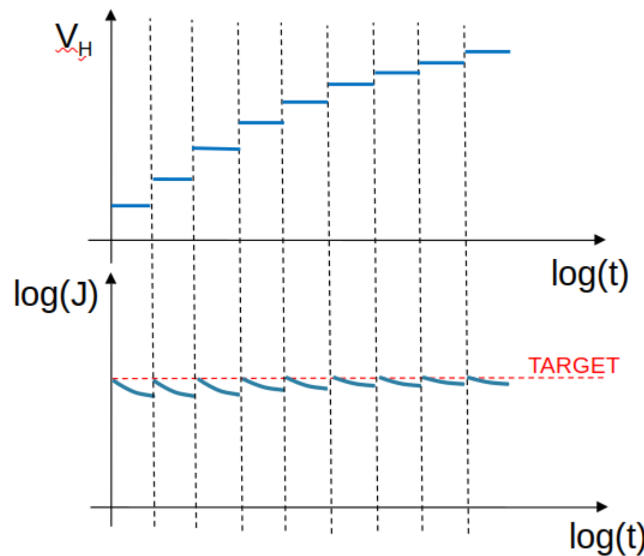

Figure 3.6: Voltage applied to the capacitor as a function of stress time (top) and current density flowing through the insulator as a function of time (bottom) during the constant-current stress. The target current is represented by the red dashed line.

In Fig. 3.7, the applied electric field calculated as $F_{OX} = |V|/t_{OX}$, with V the voltage applied at the top electrode and t_{OX} as given by the analysis of a scanning electron microscope (SEM) measurement, is reported as a function of the stress time for each current stress and temperature under study.

The application of a constant current stress substantially allows to keep constant the flux of carriers injected into the oxide during time. The oxide-field increase is an indication of the charge trapping in the oxide. The voltage

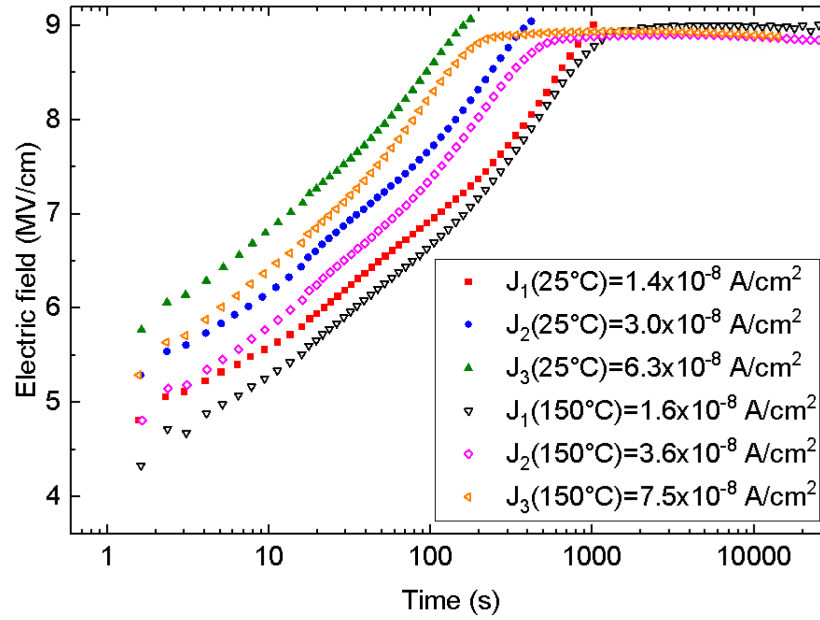

Figure 3.7: Constant current measurements performed on the SiO_2 TEOS thick capacitor. Two temperature conditions have been tested, namely $T = 25$ °C (close symbols) and $T = 150$ °C (open symbols).

increase stops when an electric field of about 9 MV/cm is reached, and saturates for longer stress times as shown in Fig. 3.7. The voltage saturation is a clear indication of the onset of avalanche condition leading to breakdown. It should be noted that the blocking field is almost independent of the current forced in the device and temperature with a value of $F_{\mathrm{OX}}^{\mathrm{BD}} \approx 9$ MV/cm.

An additional investigation on the physical mechanisms involved in the breakdown of such devices has been carried out through voltage-ramp measurements under AC and DC stress conditions. The DC stress was performed by applying a stair-case voltage ramp at a constant rate of 6 V/s (4.92 V voltage step performed in 0.82 s) to the sample until the breakdown condition was reached (red and black lines in Fig. 3.8). The AC stress consists of a train of pulses of alternating polarity with increasing amplitude up to the breakdown, the waveform is depicted in detail in Fig 3.8. The AC signal has a period of 0.82 s. In order to fairly compare the outcomes of the different DC and AC stress conditions, the amplitude difference of successive pulses of the same polarity of the AC signal has been also fixed to 4.92 V, so that the voltage increase rate per period is the same as the DC one, namely 6 V/s, which is slow enough to lead to a significant charge trapping, as shown in the previous section. Injection current is measured after any voltage step. Moreover, in order to reduce undesired displacement current effects, after

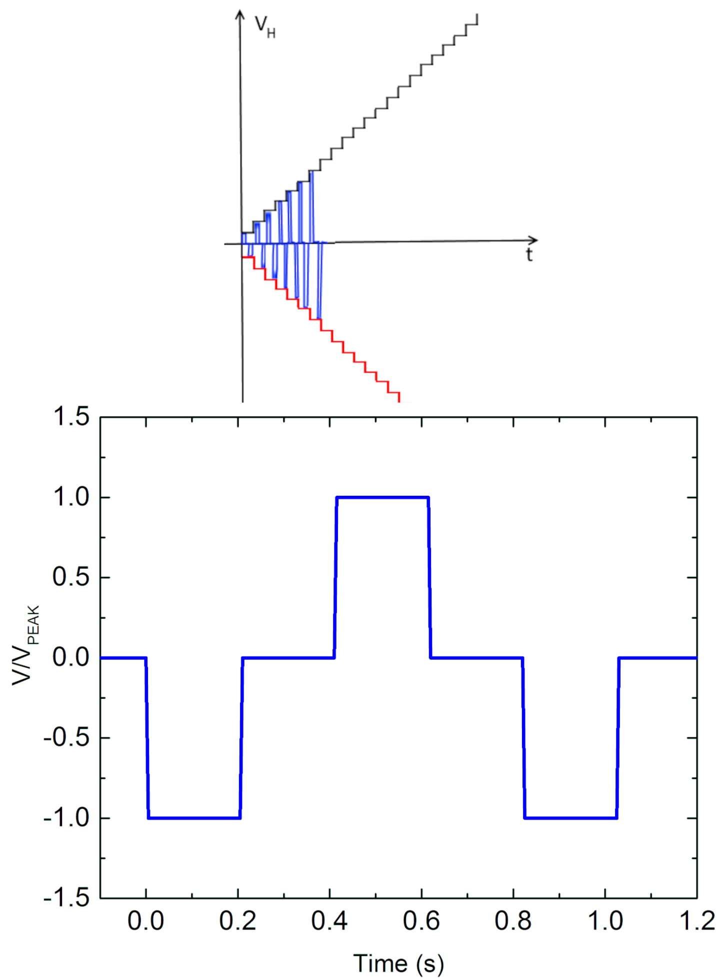

Figure 3.8: Top: AC square wave signal and negative and positive stair-case DC ramps (black and red lines) applied to the MIM under study.
Bottom: Magnification of the applied AC signal. The applied voltage to the peak voltage ratio is plotted as a function of time. The period is $T = 0.82$ s.

each positive or negative ramp, the voltage was kept constant to $V = 0$ for 0.2 s, as shown in Fig. 3.8, bottom.

In Fig. 3.9, the current density is reported as a function of the applied electric field for the AC and DC voltage-ramp stresses. Concerning the AC measurement, the plotted data have been extracted at the center of the time interval at the voltage peak for each period, so that the greatest current recorded for each period is reported. The two characteristics show a similar trend. The first part of the characteristics at low fields, up to about $F_{OX} = 6$ MV/cm, shows a relevant increase of the current due to charge injection at contacts, as explained more in details in the previous section. The current saturation observed at $F_{OX} > 6$ MV/cm is a clear indication that charge trapping is the

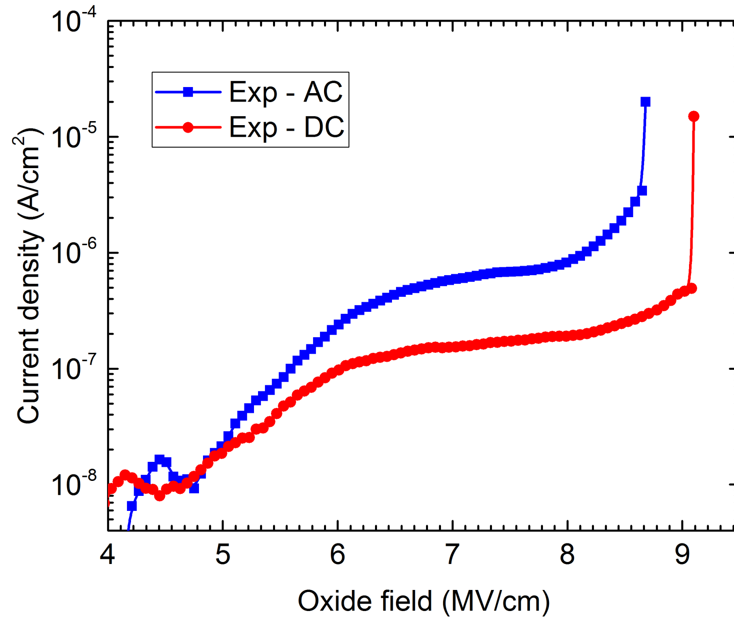

Figure 3.9: Current density as a function of the applied electric field for the AC and DC stresses.

predominant physical effect in this region. The current is greater in the case of an AC stress because the polarity change allows for de-trapping at the anode contact, thus maintaining the electric field higher at the cathode with respect to the DC stress allowing for a larger charge tunneling. At higher fields (greater than 8 MV/cm) traps become filled and the current starts increasing again up to the breakdown, with a slight anticipation in the AC regime: the AC breakdown field is $F_{\mathrm{AC}}^{\mathrm{BD}} = 8.6$ MV/cm, while the DC one is $F_{\mathrm{DC}}^{\mathrm{BD}} = 9.1$ MV/cm. Impact ionization should play a relevant role in this portion of the characteristics.

3.3 Thickness dependence of the breakdown in realistic structures

In order to have a realistic representation of the breakdown regime in thick oxides for galvanic insulation under different stress conditions, the physical mechanisms responsible of charge trapping and failure of the device must be taken into account, extending the analysis also to geometry factors which can further limit the device lifetime. Among them, the most relevant one is

the oxide thickness, but also the electrode area and the corresponding corner effects should be taken into account. A more realistic 2D structure (very similar to the real one) has been used in this part of the work.

In Fig. 3.10, the schematic cross section of the high-voltage MIM capacitor used in this work is shown. The top electrode is in tantalum nitride (TaN), the bottom electrode is in titanium nitride (TiN). The high voltage is applied to the circular top metal electrode (diameter $d \approxeq 150\mu$m), while the bottom metal electrode is grounded. The ring contact ensures protection of the device from external disturbances and acts as a lateral boundary condition at ground. The distance between the ring contact and the top metal is at least 8 times the oxide thickness in order to prevent lateral breakdown and is the same in every measured structure. The oxide thickness (t_{OX}) is defined as the distance between the top metal and the bottom metal.

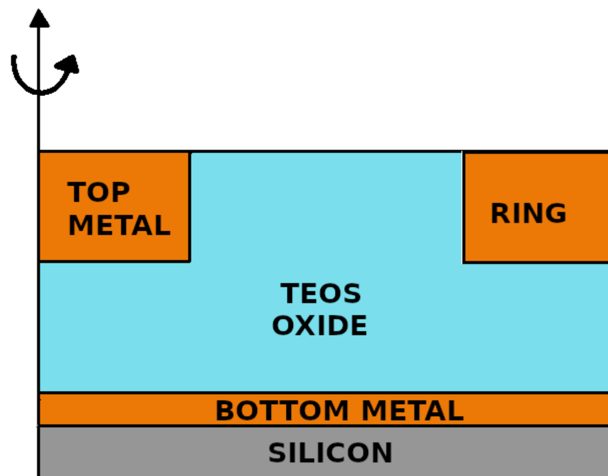

Figure 3.10: Schematic view of the 2D structure of the TEOS capacitor (not in scale).

Capacitors with different oxide thicknesses (t_{OX}) in the range between 0.6μm and 17μm have been investigated. Voltage-ramp measurements have been carried out under AC and DC stress conditions. The DC voltage stress was performed by applying a stair-case voltage ramp at a constant rate until the breakdown condition was reached, as described more in detail in the previous section (see Fig. 3.8 and the description in the text). For samples with oxide thickness less than 1μm, the AC stress consists of a train of pulses of alternating polarity with increasing amplitude up to the breakdown and is depicted in detail in Fig. 3.8. The AC signal has a period of 0.82 s. After each polarity change, a current measurement is triggered allowing to measure the oxide leakage current without any contribution related to the displacement

current. For thicker oxides with $t_{OX} > 1\mu$m, leakage current measurements are not performed and only hard-breakdown measurements have been performed.

In order to apply the same stress conditions to all the samples, different voltage-ramp rates ($R_V = dV/dt$) have been used for each device in order to have the same oxide electric field, defined as $E_{OX} = |V|/t_{OX}$ with V the voltage applied at the top electrode.

In order to fairly compare the outcomes of the different DC and AC stress conditions, the amplitude difference of successive pulses of the same polarity of the AC signal has been chosen so that the voltage increase rate per period is the same as the DC one. As far as DC ramps are concerned, the top metal acts as a cathode while the bottom metal acts as anode. The oxide field ramp used for all samples is $R_E = dE_{OX}/dt = 0.073$ MVcm^{-1}s^{-1}. All measurements have been carried out at room temperature, namely $T = 25$°C. The nominal thickness of the devices under study, the corresponding voltage-ramp and the oxide-field ramps are reported in Table 3.2.

Table 3.2: Nominal oxide thickness, voltage ramp rates and oxide field ramp rates applied to the MIM structures used in experiments.

t_{OX} (**μm**)	$\lvert R_V\rvert$ (V/s)	R_E (MVcm^{-1}s^{-1})
0.6	4.4	0.073
0.9	6.6	0.073
7.0	51	0.073
10.0	73	0.073
15.0	110	0.073
17.0	124	0.073

In Fig. 3.11 the current density J is reported as a function of the oxide electric field for some representative examples of AC- and DC-stress conditions. For the AC-stress, the current was measured only during the negative half-wave. Measurements were performed up to the breakdown with the technique shown in Fig. 3.8 for the devices with thickness 0.6μm and 0.9μm. The AC and the DC breakdown of the thicker oxides was investigated by hard-breakdown measurements performed at package level in silicon oil with the same ramp-rate up to breakdown. The J-E characteristics show a similar trend: at low electric fields (up to 6 MV/cm), the characteristics are strictly related to the charge injection due to tunneling effect; at intermediate electric fields, namely between 6 and 8 MV/cm, the current is mainly limited by charge trapping effects. The significant reduction of the current increase

in this portion of the characteristic has to be ascribed to the trap filling, as explained more in detail in the previous section. In the high-field regime, namely between 8 and 10 MV/cm, one can notice the effect of impact ionization. Our analysis will mainly focus on oxides with thicknesses larger than 0.6μm.

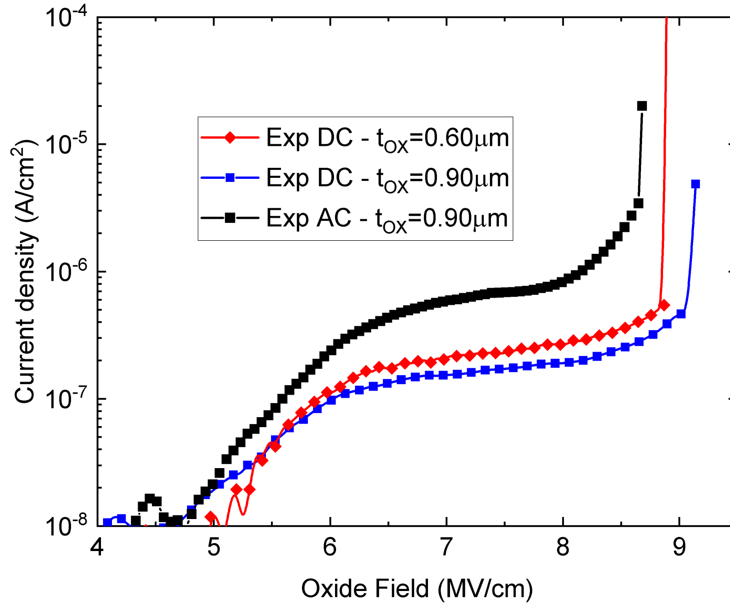

Figure 3.11: Measurements of the current density as a function of the oxide field up to the breakdown for the devices with thickness 0.6μm and 0.9μm.

Fig. 3.12 shows the breakdown field as a function of the film thickness for each device under study. The breakdown field dependence on the oxide thickness is strongly correlated to the type of stress applied to the sample. In the case of a DC stress a weak dependence is observed. The breakdown field slightly increases with t_{OX} for the thinner oxides (with thicknesses up to 0.5μm) indicating that different mechanisms other than impact ionization may play a role in the breakdown onset of such devices. More specifically, the formation of a percolation path between the contacts is expected to be the relevant effect, as reported in [50]. Differently, the breakdown field decreases for larger t_{OX}. This reduction in E_{BD} with increasing t_{OX} can be interpreted by a simple theoretical model of impact ionization, as explained in [1]. One can note that the thickness-dependent critical field for impact ionization is defined by the condition:

$$\alpha_1(E_{BD,1})t_{OX,1} = \alpha_2(E_{BD,2})t_{OX,2} \approx 1 \tag{3.1}$$

where the field-dependence of the impact ionization coefficient α is defined by the Chynoweth formula: $\alpha(E) \approx \alpha_0 e^{-E_0/E}$. By substituting this expression in Eq. 3.1 and solving for $1/E_{BD,2}$, we obtain:

$$\frac{1}{E_{BD,2}} = \frac{1}{E_{BD,1}} + \frac{1}{E_0} \ln\left(\frac{t_{OX,2}}{t_{OX,1}}\right) \tag{3.2}$$

dropping the subscripts for the thickness $t_{OX,2}$ and taking the thickness $t_{OX,1}$ as a reference, we obtain the following relationship:

$$\frac{1}{E} = \frac{1}{E_{\text{ref}}} + \frac{1}{E_0} \ln \frac{t_{\text{OX}}}{t_{\text{ref}}} \tag{3.3}$$

In Fig. 3.12, the DC-experimental data of the breakdown field (green symbols) have been fitted using Eq. 3.3 (black line) with parameters: $E_{\text{ref}} = 9.09$ MV/cm; $E_0 = 298$ MV/cm; $t_{\text{ref}} = 1\mu$m. In the AC stress the breakdown field rapidly decreases for thicker oxides, suggesting that the breakdown in these conditions may not be caused by impact ionization alone, but other factors could influence the observed behavior.

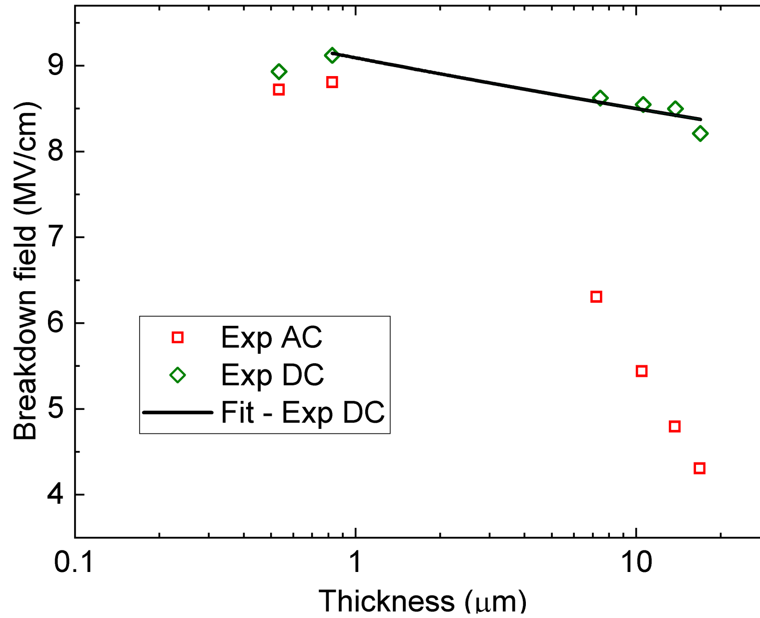

Figure 3.12: Breakdown field as a function of the oxide thickness for samples with thicknesses up to 17μm under AC and DC stresses. The black line has been obtained by fitting the DC-stress data with Eq. 3.3. $E_{\text{ref}} = 9.09$ MV/cm; $E_0 = 298$ MV/cm; $t_{\text{ref}} = 1\mu$m.

Chapter 4

TCAD modeling of the SiO_2

From a theoretical point of view, amorphous materials, such as the TEOS SiO_2, cannot be modeled as crystalline semiconductors since the absence of a periodic lattice makes the Bloch's theorem no longer valid. In addition, charge transport is dominated by capture and emission processes from defect sites in the oxide layer, hence the local distribution of trapped charges and the local field in the bulk of the oxide play a relevant role in determining the electric characteristics of MIM structures.

Different models have been proposed in the past years, but the analyses were carried out on old-generation thermal oxides. The first serious effort to take account of local field and local trapped charge variations was by O'Dwyer [51] who assumed either Schottky or Fowler-Nordheim emission at the contact and thermal de-trapping in the bulk. Frank and Simmons [52] considered instead Poole-Frenkel emission from a single trap level in the bulk with Schottky emission at the contact. Their results were later extended by Pulfrey [53] to include trap states distributed in energy and either positive or negative trapped charge. They also considered trap occupancy to be determined by the dynamic balance of trapping and de trapping rates. However at high fields, field-dependent detrapping becomes important. Arnett [44] proposed a model capable of describing the dynamics of the trapped charge distribution from a single-level trap. Analytical solutions were derived under conditions in which particular physical processes dominate (either trapping, de-trapping or steady-state) obtaining equations that relate the trapped charge distribution to the measurable current.

A second example of modeling approach was shown in [54] where the tunneling current, the impact-ionization generation and the effect of capture and emission of traps were used to describe the leakage current characteristics of metal-insulator-silicon devices. As far as traps are concerned, Si/SiO_2 interface traps were considered to be dominant with respect to SiO_2 bulk ones. Interface traps were calibrated against thermally grown SiO_2 and used

to predict the leakage current of an annealed TEOS SiO_2 showing very similar J-E characteristics. The non-annealed TEOS SiO_2, which is the subject of this study, was not simulated and no indications on the specific modeling of bulk traps, which are expected to play the main role in MIM structures, were reported in the work.

The first section of this chapter describes the TCAD setup used to simulate the test device, namely a simple parallel plate MIM capacitor with a nominal thickness of 0.9μm. The electronic structure, charge injection at the contacts, the presence of distributed defects and the breakdown mechanisms are discussed together with the TCAD models implemented. In the second section the validity of the model is checked against experiments.

4.1 Modeling approach

The conduction model in amorphous materials can be described by using a drift-diffusion (DD) transport model with suitable physical parameters, such as the energy structure, the presence of distributed defects in the material band gap and proper boundary conditions, in order to correctly account for charge injection at the contacts [32], [44]. The oxide region of interest was treated as a wide-band gap semiconductor with appropriate physical parameters in order to simulate the generation, transport, and trapping of carriers. Trapping and de-trapping mechanisms have been taken into account by using a first-order detailed balance equation for each trap as available in the TCAD tool [47]: the model explicitly takes into account the occupation rate of each trap by coupling the capture and emission rates to the conduction and valence band of the SiO_2. In order to properly account for the trapping and de-trapping effects, the Poisson equation is solved along with the transport and continuity equations of electrons and holes. The trapped charge is explicitly accounted for in the Poisson equation. This approach requires to explicitly define each type of defect, as it will be described in more details in the next sections, by fixing their energy dependence, densities and capture crosse-sections. Any field-enhanced effect on the capture and emission rates has been assumed to be modeled in the capture cross-section of each trap. Hence, the DD transport equations for electrons, holes, the trap rate equations for different traps and the Poisson equation have been calculated self-consistently on the full domain.

In Fig. 4.1, the possible conduction mechanisms in an insulator are represented. In the proposed modeling approach, the tunneling to the conduction band and directly to defects sites are taken into account, as well as the exchange of carriers (emission and capture mechanisms) between the traps and the conduction band of SiO_2. We would like to point out that in principle other conduction mechanisms can contribute to the leakage current of an amorphous insulator, such as defect-to-defect tunneling, also called multi-trap assisted tunneling (multi-TAT), as shown in Fig. 4.1. Nevertheless it has been recently shown that this contribution is not relevant especially for very thick oxides and if the defect density is lower than $N_T = 10^{20}\text{cm}^{-3}$ [55], thus we expect it not to appreciably impact on our simulation setup.

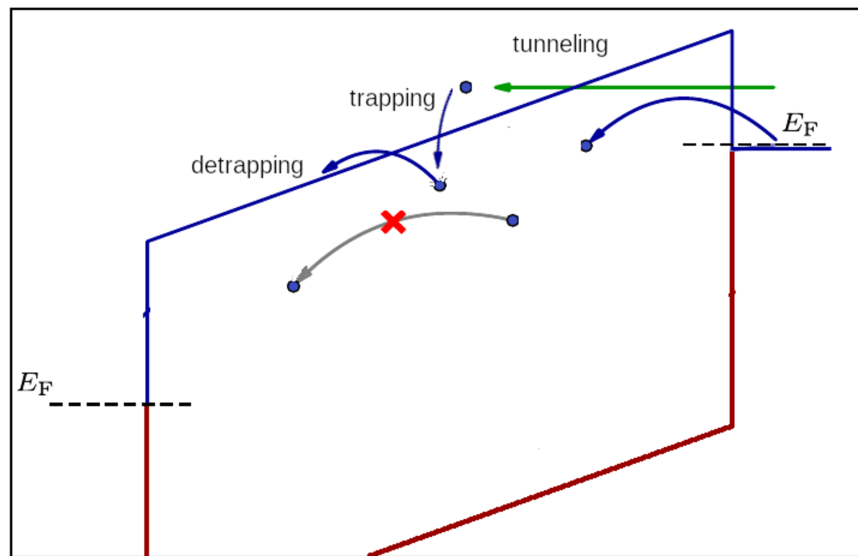

Figure 4.1: Conduction mechanisms in an insulator. In the proposed modeling approach, tunneling and trapping and detrapping of electrons are taken into account. Trap-to-trap conduction (hopping, or multi-TAT) is expected not to be relevant, hence it is not taken into account.

It is worth noting that, since very high fields are involved, so that electrons may become hot, other conduction model for transport, such as the hydrodynamic model (HD), may prove effective, in principle. The hydrodynamic model is a more complex and detailed model that takes into account additional effects such as momentum transfer, energy exchange, and carrier-carrier scattering [56]. This model is typically used for simulating high-speed devices, where carrier transport is strongly affected by the motion of the carriers themselves and their interactions with each other. However, since very small carrier concentrations are involved in an insulator, such mechanisms

are negligible and the DD model is expected to provide a good approximation of the behavior of carriers. Moreover, the hydrodynamic model is computationally expensive and requires high-performance computing resources to solve, making it less practical for routine device simulations.

4.1.1 Electronic structure

The electronic structure of SiO_2 has been intensively investigated experimentally and theoretically. In [29], the properties of thermal SiO_2 on silicon were reported, showing that the band gap, according to the experiments on internal photoemission, can be as low as 8.06 eV [57].

Moreover, the theoretical band calculations show that the electron effective mass tensor is isotropic and the electron effective mass is equal to 0.5 m_0, where m_0 is the electron rest mass. The hole effective mass tensor, on the contrary, is anisotropic and shows two mass values, 1.3 m_0 (light holes) and 7.0 m_0 (heavy holes) [29]. For this reason, the energy gap, the density of states and the carriers effective masses in the conduction and in the valence band and the intrinsic hole and electron mobility of the semiconductor material have been modified and set to the corresponding values for silicon oxide.

The energy gap has been set to the commonly accepted value $E_G = 8.9$ eV [58]. However, given the recent works on TEOS indicating a possible reduction of the gap, we checked the role of the band gap value by simulating the same devices with $E_G = 8.0$ eV. No significant variations have been observed due to the specific value of E_G. The conduction and valence band density of states are $N_C = 9 \cdot 10^{18}$ cm^{-3} and $N_V = 2.6 \cdot 10^{19}$ cm^{-3}, respectively. These values have been calculated from the classical formula for isotropic parabolic bands with effective masses m_e^* and m_h^*:

$$N_C = \frac{1}{4\pi^3} \left(\frac{2\pi k_B T m_e^*}{\hbar^2} \right)^{3/2} \tag{4.1}$$

$$N_V = \frac{1}{4\pi^3} \left(\frac{2\pi k_B T m_h^*}{\hbar^2} \right)^{3/2} \tag{4.2}$$

As reported by [6], [59] experiments show that TEOS-based structures exhibit an energy barrier at the contact as low as 2.5 eV, leading to a significant increase of the leakage current with respect to thermally-grown SiO_2. In our simulations the energy barrier at the contact has been kept fixed to 2.5 eV, equal to the reported values for TaN [59]. The same energy barrier has been defined for the two contacts.

4.1.2 Electron and hole mobility

Electrons and holes in SiO_2 exhibit significantly different mobilities. Hole mobility ranges from 10^{-11} to 10^{-4} $cm^2V^{-1}s^{-1}$ depending on electric field and temperature [60], [61], while electron mobility ranges from 20 to 40 $cm^2V^{-1}s^{-1}$ [62], [63]. The transport of electron and holes through the oxide is believed to be due to mechanisms such as trap-mediated conduction and valence band conduction or hopping transport by tunneling between localized trap sites in the SiO_2 bandgap [64]. However, simplified drift-diffusion based models have been successfully used to approximate carrier transport in SiO_2 films [65], [66]. We implemented constant mobility models for both electrons and holes, with the effective mobilities equal to $\mu_e = 21$ $cm^2V^{-1}s^{-1}$ [32] and $\mu_h = 1 \cdot 10^{-4} cm^2V^{-1}s^{-1}$ [61] for electrons and holes, respectively. Those values are also reported in Table 4.1.

At high electric fields, the carrier drift velocity is no longer proportional to the electric field, but instead the velocity saturates to a finite speed called saturation velocity v_{sat}. Hence, according to the semi-empirical Canali model, the carrier mobility is field-dependent [67]:

$$\mu(F) = \frac{\mu_0}{\left(1 + \left(\frac{\mu_0 F}{v_{sat}}\right)^{\beta}\right)^{1/\beta}} \tag{4.3}$$

where μ_0 denotes the low-field mobility, F is the electric field and the exponent β and v_{sat} are temperature dependent according to a power law:

$$\beta = \beta_0 \left(\frac{T}{T_0}\right)^k \tag{4.4}$$

$$v_{sat} = v_{sat,0} \left(\frac{T}{T_0}\right)^l \tag{4.5}$$

where T_0 is the reference temperature, namely $T_0 = 300$K and β_0 and $v_{sat,0}$ the values of β and v_{sat} at T_0, respectively. Thus, the Canali model as available in the TCAD tool has been activated for the high-field mobility of electrons and holes.

In Fig. 4.2, the electron drift velocity is plotted as a function of the electric field at $T = 300$K. The TCAD parameters of the Canali model for the electron mobility have been calibrated against the experimental data from [68] so that the calculated drift velocity matches the measured one. A saturation velocity $v_{sat} = 1.6 \cdot 10^7 cm/s$ can be deduced from the experimental data.

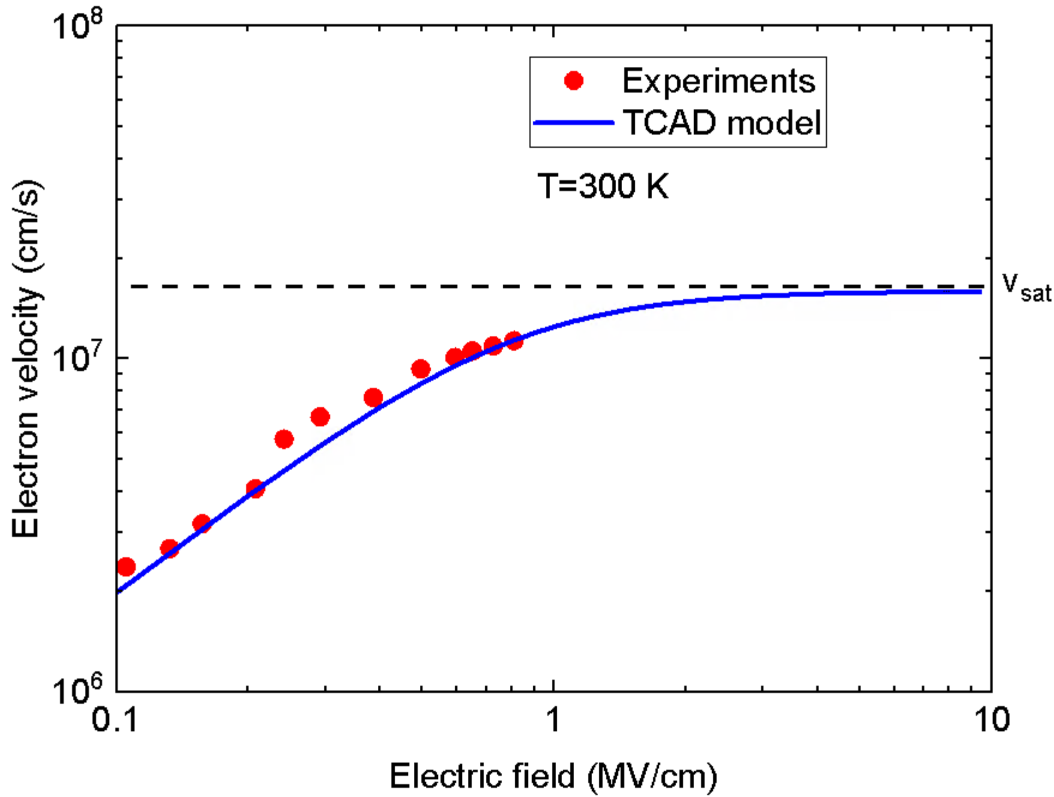

Figure 4.2: Electron drift velocity as a function of the electric field at room temperature, namely $T = 300$K. Symbols: experiments from [68]. Solid line: TCAD model. The black dashed line represents the saturation velocity $v_{sat} = 1.6 \cdot 10^7$cm/s.

4.1.3 Charge injection

Concerning charge injection from the electrodes, it has been properly taken into account by defining a Schottky barrier at the contacts with an energetic barrier $E_B = 2.5$ eV [59]. Voltage ramp simulations with ramp rate of 24 V/s with no traps have been performed at different temperatures in order to investigate charge injection at contacts. As a first hypothesis, we assumed that the measured current increase as a function of the oxide field was due to the barrier lowering effect. For this reason, simulations have been performed by activating the barrier lowering model with default parameters for both electrons and holes. Fig. 4.3 shows the current density as a function of the applied electric field. The current is many orders of magnitude lower than its experimental counterpart (see experiments reported in Fig. 4.8). In addition, a strong temperature dependence is observed, in contrast with the experiments that showed a weak temperature dependence, indicating that the emission over the barrier is not the most relevant physical mechanism related to charge injection at the contacts.

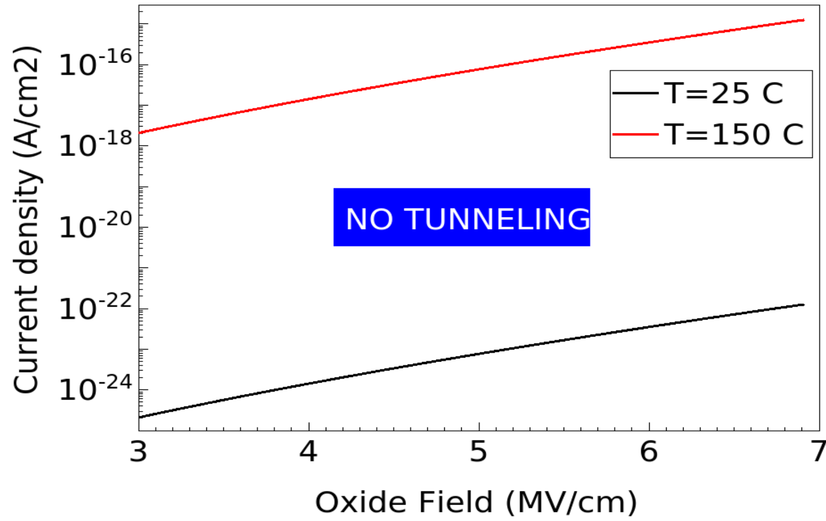

Figure 4.3: Analysis of charge injection: current density as a function of the oxide field at two temperature conditions, namely $T = 25$ °C and $T = 150$ °C. Simulations have been performed with no traps and by activating the barrier lowering model.

For this reason, we used the standard nonlocal tunneling model for both electrons and holes available in the TCAD based on the Wentzel-Kramers-Brillouin (WKB) approximation [69]. The electron tunneling current from the metal to the insulator $J_{\mathrm{M-I}}$ and the tunneling current from the insulator to the metal $J_{\mathrm{I-M}}$ are given by:

$$J_{\mathrm{M-I}} = A^* T^2 \int_{\varepsilon}^{\infty} \Gamma(r) \ln\left(\frac{1}{1+\exp((\varepsilon' - E_{Fn})/k_B T)}\right) d\varepsilon' \tag{4.6}$$

$$J_{\mathrm{I-M}} = A^* T^2 \int_{\varepsilon}^{\infty} \Gamma(r) \ln\left(\frac{1}{1+\exp((\varepsilon' - E_{Fm})/k_B T)}\right) d\varepsilon' \tag{4.7}$$

where A^* is the Richardson constant, E_{Fn} is the electron quasi-Fermi energy in the insulator, E_{Fm} is the Fermi level of the metal and $\Gamma(r)$ is the position-dependent tunneling probability. The net tunneling current can be expressed as the difference between these two currents:

$$J_{\mathrm{tun}} = J_{\mathrm{M-I}} - J_{\mathrm{I-M}} \tag{4.8}$$

The tunneling probability of the carriers is calculated using the WKB approximation through:

$$\Gamma(r) = \exp\left(-\frac{2}{\hbar}\int_0^r \sqrt{2m_T(E_C(x) - \varepsilon)}dx\right) \tag{4.9}$$

where the integrand represent the local imaginary wave number of the particles with energy ε, m_T is the tunneling mass in the conduction band and E_C is ts the conduction band energy. Similar equations can be obtained for the holes, provided that E_{Fn} is substituted with E_{Fp} and that the valence band takes place of the conduction band.

Fig. 4.4 shows the current density as a function of the applied electric field. The current temperature dependence is very weak, indicating that tunneling dominates over Schottky emission.

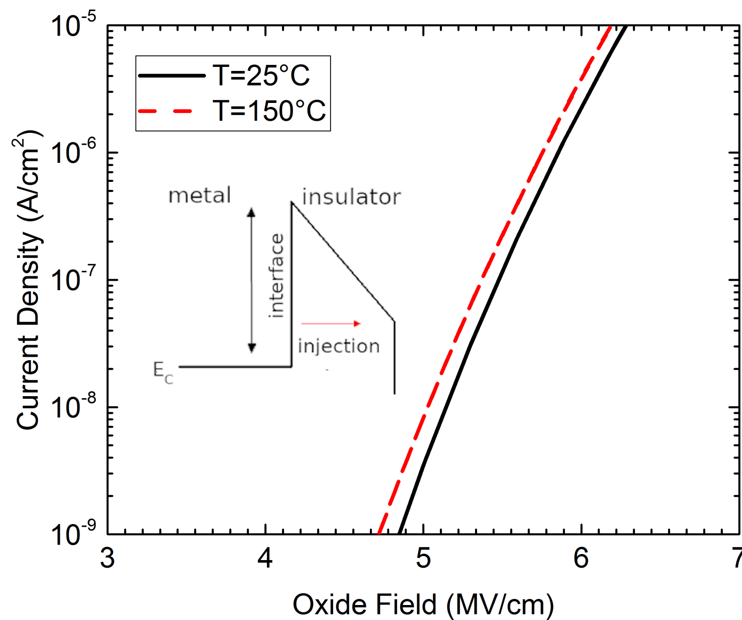

Figure 4.4: Analysis of charge injection: current density as a function of the oxide field at two temperature conditions, namely $T = 25$ °C and $T = 150$ °C. Simulations have been performed with no traps. Inset: Metal-insulator band diagram.

As both contacts are metal electrodes forming a Schottky barrier with the oxide interface much lower for electrons than for holes, in this contribution electron injection is expected to dominate. For this reason, in order to improve the convergence speed of the simulations, in the following only the nonlocal tunneling model for electrons has been used. Hence, the only free parameter of the model is the electron tunneling mass which has been properly adjusted to 0.5 m_0. It is worth noting that this value corresponds to that reported in [54] for the electron tunneling from n-Si to TEOS SiO_2.

In Table 4.1 the parameter set for SiO_2 and TaN is reported.

Table 4.1: TCAD parameter set for SiO_2 and TaN: metal Work Function (Φ_m), metal-oxide Energy barrier (E_B), Energy bandgap (E_G), conduction and valence band denstity of states (N_C and N_V) and electron and hole mobility (μ_e and μ_h) are reported.

Parameter	Value
Φ_m (eV)	4.4 [70]
E_B (eV)	2.5 [59]
E_G (eV)	8.9
N_C (cm^{-3})	$9 \cdot 10^{18}$
N_V (cm^{-3})	$2.6 \cdot 10^{19}$
μ_e ($cm^2V^{-1}s^{-1}$)	21
μ_h ($cm^2V^{-1}s^{-1}$)	$1 \cdot 10^{-4}$

4.1.4 Defects

As mentioned in the previous sections, despite the type of defects typically present in SiO_2 are well known and extensively studied [12], many results can be applied only to very thin oxides featuring the presence of silicon at the interface.

Both acceptor and donor traps are usually present in silicon oxide. However, the implementation of both electron and hole traps would make our model much more difficult to handle without giving appreciable contributions. Anyway the injection of holes is negligible as shown in Fig. 4.5 where the electron and hole current densities are reported as a function of the applied electric field, thus only acceptor traps have been implemented, i.e. defects that are neutral when empty and carry a negative charge when occupied by an electron. A uniform spatial distribution is assumed for all traps.

Concerning the energy level of the traps, it should be pointed out that, being SiO_2 an amorphous material, energy bands arise instead of discrete trap levels. For this reason we have defined two uniform distributions with a width of 0.5 eV each with mean energies $E_1 = 6.3$ eV and $E_2 = 6.5$ eV, where the oxide valence band has been taken as the reference level. These values are in quite good agreement with the results reported in [12] corresponding to the four-state hydrogen bridge and hydroxyl center defects, respectively. The energy distribution of traps is reported in Fig. 4.6, showing also the different distribution functions adopted for the bands. No significant sensitivity to the energetic function was observed when comparing simulation results carried out with the uniform distribution and the equivalent Gaussian functions.

The determination of trap cross-sections requires a special attention for

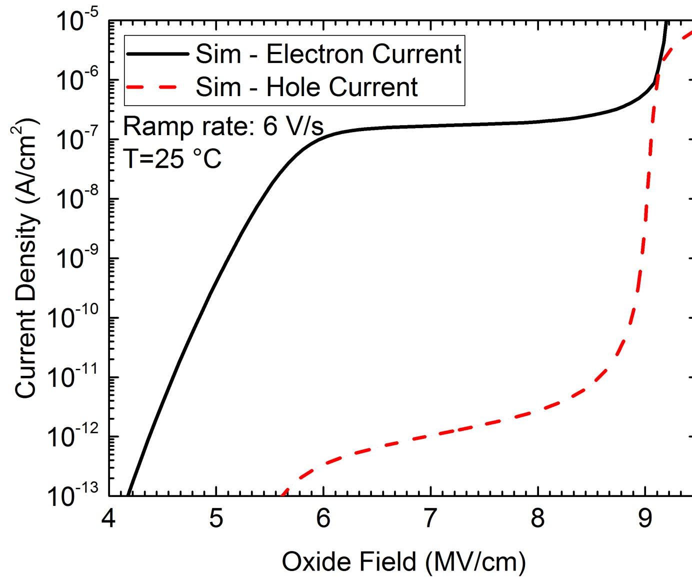

Figure 4.5: Electron and hole current densities as a function of the applied electric field from simulations for a voltage ramp stress with ramp rate of 6 V/s.

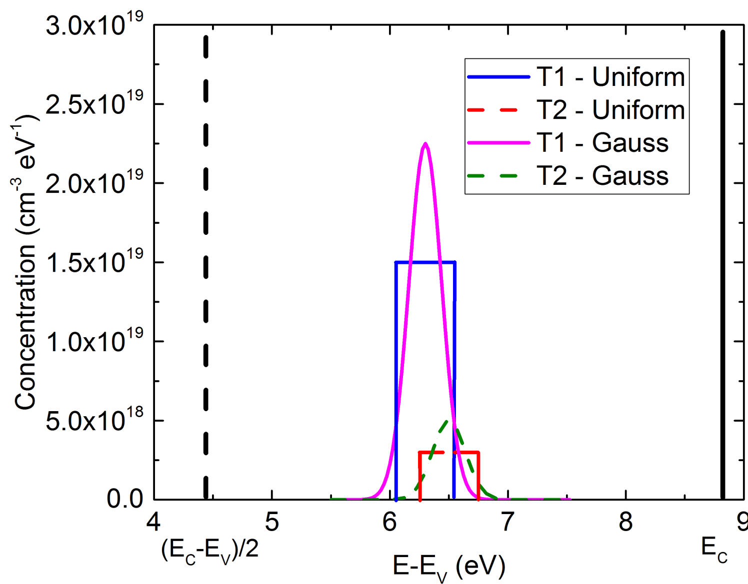

Figure 4.6: Energy distribution of traps. Both the uniform distribution adopted and the equivalent densities with Gaussian functions are plotted. The valence band has been taken as the reference level, i.e. $E_V = 0$. The point $(E_C - E_V)/2$ represents the mid-band gap and corresponds to the Fermi level. A band-gap $E_G = 8.9$ eV is assumed for SiO_2.

transient responses. In the past years, many authors have reported measurements of electron capture cross sections [71]–[74], with values ranging from 10^{-13} cm^2 to 10^{-18} cm^2, so cross sections are not unambiguously determined. We have used two different cross sections of, respectively, $\sigma_1 = 1.1 \cdot 10^{-15}$ cm^2 and $\sigma_2 = 9 \cdot 10^{-15}$ cm^2, in fair good agreement with the values reported in [75], where it has been shown that two different electron cross sections exist which differ by as much as 1-2 orders of magnitude. This choice allows us to better describe the transient response of the DC stress characteristics on the full time range covering 4 orders of magnitude. A summary of the trap parameters used for the two trap distributions is reported in Table 4.2.

Table 4.2: Trap parameters used for the two trap distributions. Mean energy of the trap level, trap width, electron capture cross section and trap density are reported for each type of trap. The parameter E_T is referred to the top of the conduction band, taken as the reference level.

Parameter	Trap 1	Trap 2
E_T (eV)	6.3	6.5
ΔE (eV)	0.5	0.5
σ_e (cm^2)	$1.1 \cdot 10^{-15}$	$9 \cdot 10^{-15}$
N_T (cm^{-3})	$7.5 \cdot 10^{18}$	$1.5 \cdot 10^{18}$

The second important aspect to take into account in order to have a complete representation of the physics of the device, is the definition of the emission-enhancement mechanisms from traps which play a relevant role at high fields. Two kinds of electric field effects are generally considered: the lowering of the potential barrier (Poole-Frenkel effect) and the tunneling effect. The enhanced emission cross section can be expressed in terms of the enhancement factors Γ_{PF} and Γ_{tun} as follows:

$$\sigma = \sigma_0(1 + \Gamma_{PF} + \Gamma_{tun}) \tag{4.10}$$

where σ_0 is the cross section when no electric field is applied.

Poole-Frenkel model

The well-known Poole-Frenkel effect describes the increase of the thermal emission rate of carriers in an external electric field due to the lowering of the barrier associated with their Coulomb potential. The emission cross section enhancement factor is calculated as follows :

$$\Gamma_{PF} = \frac{1}{\alpha^2}[1 + (\alpha - 1)e^{\alpha}] - \frac{1}{2} \tag{4.11}$$

$$\alpha = \frac{1}{kT}\sqrt{\frac{q^3 F}{\pi\varepsilon_0\varepsilon_{\text{PF}}}} \tag{4.12}$$

where F is the electric field, q is the electron charge, T the temperature and ε_{PF} the Poole-Frenkel permittivity of SiO_2. It should be noted that the typical square-root dependence is valid only if one assumes a coulombic potential for traps [45]. Other potentials lead in some cases to integrals which cannot be solved analytically. By using this model we are implicitly assuming that we are dealing with a coulombic potential, which is a reasonable hypothesis. At a strong electric field this effect is much weaker than the tunneling effect, but at a weak field and/or for shallow levels it can greatly enhance the emission probability.

Hurkx model

At strong electric fields tunneling becomes relevant. The Hurkx model [76] describes the field-enhanced emission of carriers by the phonon-assisted tunneling effect from traps. Pure tunneling is not considered since it becomes relevant only at very high fields ($F > 10$ MV/cm) [76]. The expression for the enhancement factor of the emission probability is given by an integral of the product of a Boltzmann factor, which gives the excitation probability of a carrier at the trap level to an excited level E, and the tunneling probability at that energy level from the trap to the band [77]. The integral is calculated over all the possible phonon-assisted transitions, hence from the trap energy E_T to to the conduction band energy E_C.

$$\Gamma_{TAT} = \int_0^{(E_C - E_T)/k_B T} \exp\left[z - \frac{4}{3}\frac{F_0}{F} z^{3/2}\right] dz \tag{4.13}$$

where $z = (E_T - E)/k_B T$, F is the electric field and F_0 is a constant given by the following expression:

$$F_0 = \frac{q\hbar}{\sqrt{2m_T (k_B T)^3}} \tag{4.14}$$

with m_T the tunneling mass of the carriers, the only free parameter of this model. It should be pointed out that this model is derived assuming a Dirac well and a linear potential. An approximate expression of the emission enhanced factor for tunneling from a Coulombic well has been derived in [46]. However, it differs from the model used only by a multiplication factor

$1 - (\Delta E_T/E)^{5/3}$ in the exponential, which is expected not to give a relevant contribution. Moreover, the model is not implemented in the TCAD.

The phonon-assisted tunneling emission from traps is expected to play a key role in the AC stress conditions. This hypothesis has been checked by extracting the total trapped charge during a square-wave AC stress with pulses of 650 V and period of 14 s, where the impact of charge trapping and detrapping is supposed to be dominant. In Fig. 4.7 we report a comparison of the trapped charge in the proximity of the top electrode between a simulation obtained by activating both the Hurkx and the Poole-Frenkel models and an analogous one in which only the Poole-Frenkel model has been used. It is clear that by activating the Hurkx model it is possible to have an appreciable charge de-trapping during the stress.

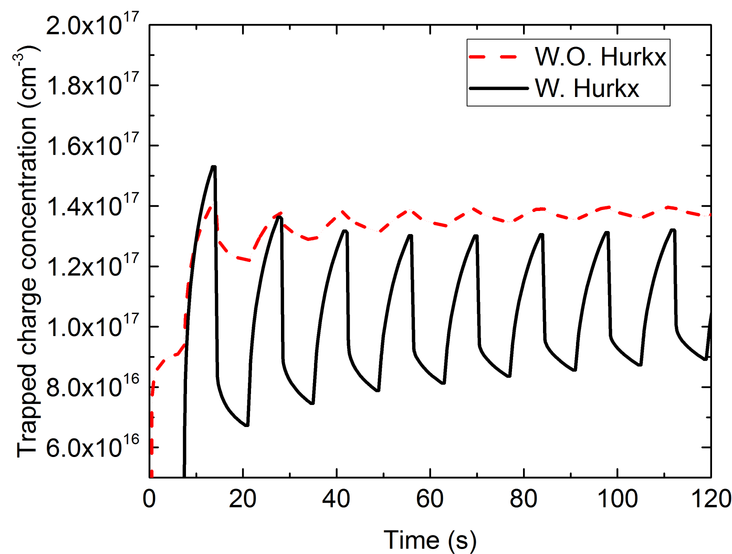

Figure 4.7: Trapped charge concentration as a function of time for a square wave AC stress near the top contact. Continuous line: simulation performed activating the Hurkx model; Dashed line: simulation performed without the Hurkx model.

4.1.5 Impact-ionization

As far as high electric fields (greater than 7MV/cm) are concerned, the effect of avalanche due to impact ionization cannot be neglected in a complete picture of the relevant physical mechanisms [78]. Several models have been proposed to describe the dependence of the impact-ionization coefficients as a function of the electric field.

Van Overstraeten-De Man model

The impact ionization coefficients α_n and α_p can be modeled as exponential functions of the electric field as predicted by the Van Overstraeten-de Man model [79] which is based on the Chynoweth law [80]. Dropping the subscript for electron and holes, the model reads:

$$\alpha = \gamma a \exp\left(\frac{\gamma b}{F}\right) \tag{4.15}$$

where a and b are fitting parameters with the dimensions of an inverse of a length and of an electric field, respectively. The temperature dependence of the model is contained in the factor γ which is:

$$\gamma = \frac{\tanh\left(\frac{\hbar\omega_{\mathrm{OP}}}{2k_B T}\right)}{\tanh\left(\frac{\hbar\omega_{\mathrm{OP}}}{2k_B T_0}\right)} \tag{4.16}$$

where T_0 is a reference temperature, namely $T_0 = 300$K and $\hbar\omega_{\mathrm{OP}}$ represents the optical phonon energy.

Okuto-Crowell model

Okuto and Crowell [81] proposed a nonlocal model for the calculation of the ionization coefficients. However, since the exact expressions are too complicated for easy use in practical device characterization, they suggested the following empirical analytic expression:

$$\alpha = a(1 + c(T - T_0))F^{\gamma} \exp\left[-\left(\frac{b[1 + d(T - T_0)]}{F}\right)^{\delta}\right] \tag{4.17}$$

where $T_0 = 300$K is a reference temperature and a, b, c, d, γ and δ are fitting parameters. These values apply in a wide range of electric fields.

4.2 Simulation results

The TCAD results are compared against J-V experiments in different regimes to check the validity of the proposed transport model. Fig. 4.8 shows the slow voltage ramp stress current densities as a function of the applied electrical field up to breakdown at different temperatures, namely $T = 25$ °C, $T = 100$ °C and $T = 150$ °C.

At low electric fields, the characteristics is strictly related to the charge injection due to tunneling effect. At intermediate electric fields, the current is

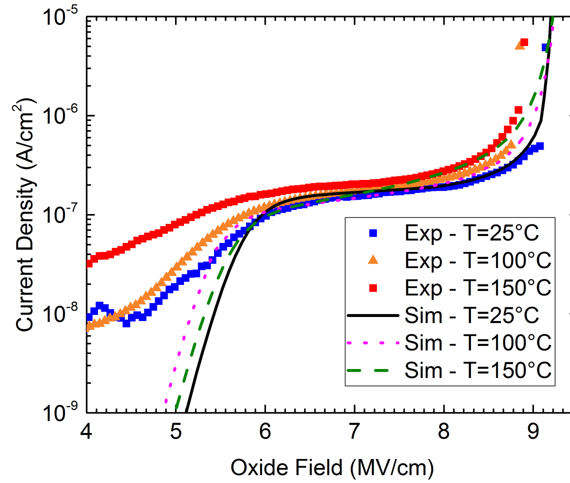

Figure 4.8: Current density as a function of the applied electric field for voltage ramp stress up to breakdown. Three temperature conditions are represented, namely $T = 25\ ^{\circ}\mathrm{C}$, $T = 100\ ^{\circ}\mathrm{C}$ and $T = 150\ ^{\circ}\mathrm{C}$. Symbols: experiments; Solid and dashed lines: simulations.

mainly limited by charge trapping effects: this indicates that the cathode field is decreasing due to significant electron trapping in the bulk of the oxide, which in turn limits the tunneling current. In the high-field regime, namely between 8 MV/cm and 10 MV/cm, one can notice the effect of impact ionization which will be described more in detail in the next part of this report. The slight difference observed in the current levels at different temperatures in the intermediate-field regime can be ascribed to the effect of temperature on the trapping rates.

Concerning the faster ramp shown in Fig. 4.9, despite the peak current slightly differs from the experimental value (by about a factor of 2), the hysteresis is very well reproduced, indicating that the amount of trapped charge during the stress is in quite good agreement with the experimental data. Moreover, the slope of the decreasing part of the ramp is nicely captured by simulations. We would like to point out that at low fields (lower than 5MV/cm) the difference between the experimental data and simulations for the slow ramp (6V/s) can be ascribed to the contribution of the perimeter current which is not taken into account in our simulations. Concerning the faster ramp, the low field deviation from the tunneling contribution might be due to defect-related conduction, as a trap assisted tunneling from contacts [5], [6]. However, at high fields the latter is not relevant with respect to the tunneling contribution. In the backward ramp the trap assisted tunneling

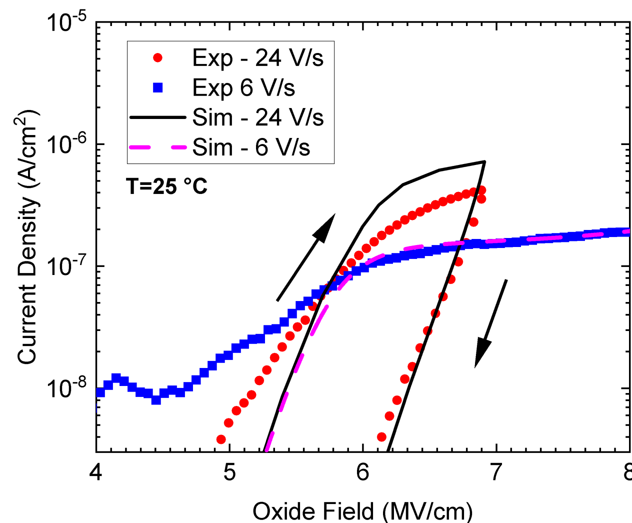

Figure 4.9: Current density as a function of the applied electric field for voltage ramp stress up to F_{OX} = 6.75 MV/cm. Two ramp rates have been used, namely 24 V/s and 6 V/s. Red Symbols: experiments, areal current (fast ramp); Blue symbols: experiments, total current (slow ramp); Lines: simulations.

is suppressed because traps are charged and the WKB tunneling behavior is observed.

The trap parameters, such as energy distribution and cross section, can be investigated by analyzing the DC-stress characteristics. In Fig. 4.10, the current density is shown versus the stress time for the constant voltage stress at $F_{OX} = 6.65$ MV/cm. Simulations with different sets of trap parameters are reported. The solid black lines of Fig. 4.10 are in fair good agreement with the experimental results. Changing either the mean energy of the traps or the electron capture cross section can have a great impact on the current. In particular, setting a smaller cross section for both traps (blue dashed curves of Fig. 4.10) leads to a nearly rigid shift of the log-log characteristics: the less charge is trapped, the greater the current is. It should be noted that the slope of the straight line in the log-log plot is directly related to the trap depth within the energy band gap of the insulator, as demonstrated by the dot-dashed curves of Fig. 4.10 which feature a modification of the mean energy of the traps with respect to the best choice of trap parameters. Thus we can conclude that our choice of the energy levels can capture the relevant mechanisms.

In addition to this, in order to determine the impact of each trap on the DC-stress characteristics, simulations with a single trap distribution with the

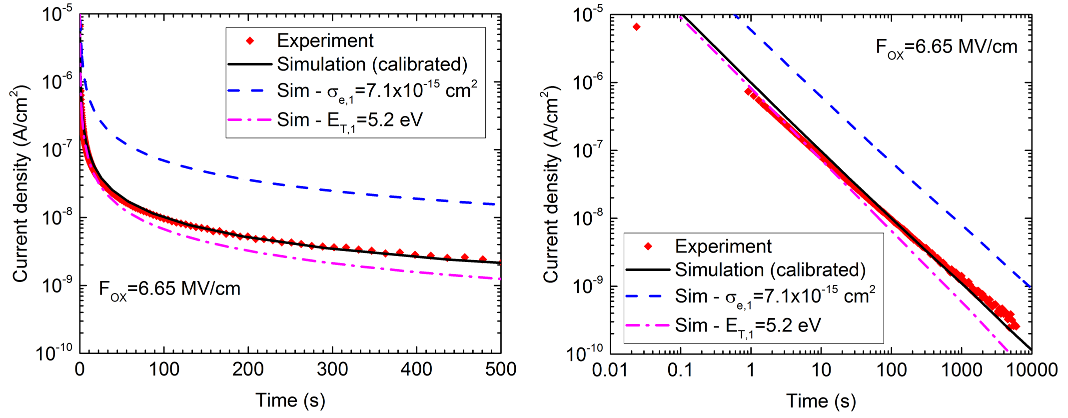

Figure 4.10: Left: Semi-logarithmic current plot comparison of experimental data (symbols) and simulation results (lines) for a constant voltage stress performed at $F_{\mathrm{OX}} = 6.65\ \mathrm{MV/cm}$.
Right: Log-log current plot comparison of experimental data (symbols) and simulation results (lines) for a constant voltage stress performed at $F_{\mathrm{OX}} = 6.65\ \mathrm{MV/cm}$.
The black solid lines were obtained with the calibrated parameters for all the traps (reported in Table 4.2), while the blue dashed and red dash-dotted lines were obtained by changing either the capture cross section or the trap level of the first trap, respectively.

same parameters for each trap as those reported in Table 4.2 are reported in the top chart of Fig. 4.11, where T1 denotes Trap 1 and T2 denotes Trap 2. It can be noted that both distributions are necessary in order to fairly reproduce the experimental data: T1 dominates over T2 at long stress times, being the concentration of T1 greater than that T2, while, on the contrary, the contribution of T2 is more appreciable at short stress times due to its much greater cross section than that of T1. Moreover, simulations have been carried out with a single trap distribution (T1) but with different sets of trap parameters than those reported in Table 4.2. They are shown in Fig. 4.11, left. Each curve has been obtained by changing either the concentration (N_{T}), the mean energy of the trap (E_{T}) or the electron capture cross section (σ_{e}). The modification of those parameters can have a great impact on the current, leading to an inaccurate prediction of experimental data. The same analysis has been carried out on the single trap T2 obtaining similar results (not shown here). For these reasons, along with the possibility of fairly reproducing other stress conditions and the fact that the chosen distributions are in quite good agreement with the ones reported in [12], we can conclude that our choice of the trap distributions can capture the relevant mechanisms.

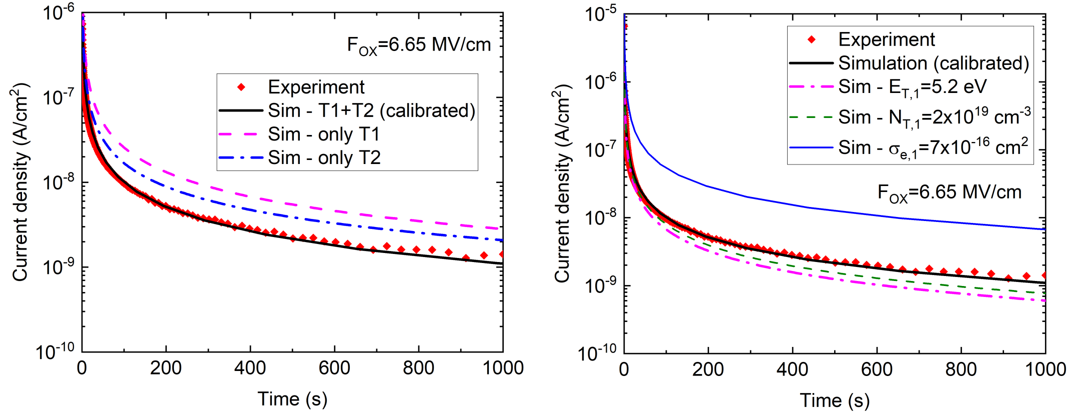

Figure 4.11: Semi-logarithmic current plot comparison of experimental data (symbols) and simulation results (solid and dashed lines) for a constant voltage stress performed at $F_{OX} = 6.65$ MV/cm and room temperature.
Left: The black solid line was obtained with the calibrated parameters for all the traps (reported in Table 4.2), while the magenta dashed and the blue dash-dotted lines were obtained by defining only one distribution of traps, T1 and T2 respectively, with the calibrated parameters.
Right: The black solid line was obtained with the calibrated parameters for all the traps (reported in Table 4.2). Other simulations were performed by defining only one distribution of traps (T1) and changing only one parameter at a time (with respect to those reported in Table 4.2): the energy level of the trap (magenta dash-dotted line), the total concentration (green dashed line) and the capture cross section (blue solid line).

In order to assess the role of de-trapping mechanisms, the AC-stress characteristics have been taken as the main reference. Fig. 4.12 shows the experimental versus simulated AC current characteristics obtained with two different setups: in the first one (dashed line of Fig. 4.12) the Poole-Frenkel model has been activated and the Hurkx model has been turned off; in the second one (solid line of Fig. 4.12) both models have been activated. The Poole-Frenkel model alone is not capable of reproducing the observed recovery of the current at each half-wave, which is strictly related to de-trapping mechanisms. However, the current recovery can be at least qualitatively captured by activating also the Hurkx model for the emission cross section enhancement. This is a hint that trap-assisted tunneling is not negligible at the electric fields under consideration and has to be properly modeled as well as the Poole-Frenkel effect.

Finally, in order to gain further insight on the charge trapping and de-trapping dynamics, Fig. 4.13 and 4.15 show the trapped charge across the

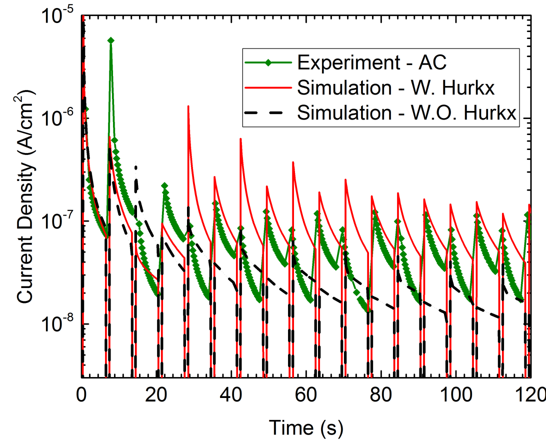

Figure 4.12: Current density as a function time for a square wave AC stress with period $T = 14$ s and amplitude $F_{OX} = 6.65$ MV/cm. Symbols+line: experiments; Solid lines: simulations with the Hurkx model; Dashed line: simulations without the Hurkx model.

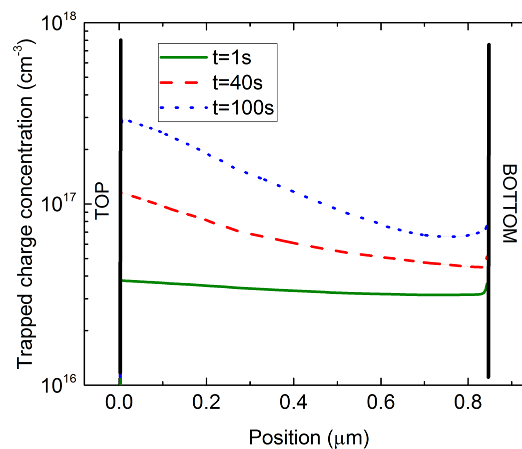

Figure 4.13: Trapped charge as a function of the position across the oxide layer for the DC-stress. Three instants are represented: $t = 1$ s (solid line), $t = 40$ s (dashed line), $t = 100$ s (dotted line).

device at different instant of the DC and AC transient simulations, respectively. For the DC stress condition, also the electric field distribution across the insulator has been reported in Fig. 4.14. The two stress conditions show very different behaviors. In the DC stress (Fig. 4.13), even if the great majority of the total charge is trapped in the first instants of the simulation, charge buildup in the oxide continues for hundreds of seconds up to a saturation condition. In addition, one can observe that more charge is trapped near the top contact, as expected, as it is the cathode, thus causing charge accumulation in its proximity. As clearly shown by Fig. 4.14, the trapped charge is responsible for a consistent modification of the electric field, which increases

near the the anode and decreases in proximity of the cathode. Differently, in the AC stress (Fig. 4.15) the saturation condition seems to be reached at shorter times with respect to the DC counterpart. Moreover, charge buildup is significantly enhanced near the two contacts, while a slight emptier region is formed in the center of the device. In fact, the two electrodes act in succession as cathodes leading to a greater charge trapping which is not possible in the center of the oxide due to a different balance between trapping and de-trapping mechanisms.

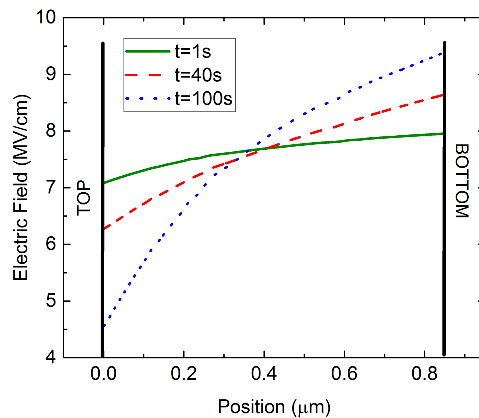

Figure 4.14: Electric field distribution across the oxide layer for the DC-stress. Three instants are represented: $t = 1$ s (solid line), $t = 40$ s (dashed line), $t = 100$ s (dotted line).

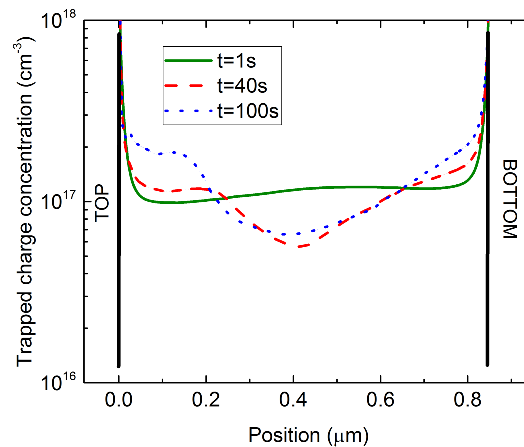

Figure 4.15: Trapped charge as a function of the position across the oxide layer for the AC-stress. Three instants are represented: $t = 1$ s (solid line), $t = 40$ s (dashed line), $t = 100$ s (dotted line).

4.2.1 Breakdown

As far as high electric fields (greater than 7MV/cm) are concerned, the effect of avalanche due to impact ionization cannot be neglected in a complete picture of the relevant physical mechanisms. Thus, the impact-ionization generation has been taken into account in our simulation setup using the Van Overstraeten-De Man model fitted against the experimental and theoretical data reported in [78]. Fig. 4.16 shows the calibrated ionization coefficient against experimental data as a function of the electric field. The phonon energy was fixed to 153 meV, consistently with the indications in [78] showing a limited temperature dependence of the electron impact-ionization coefficient.

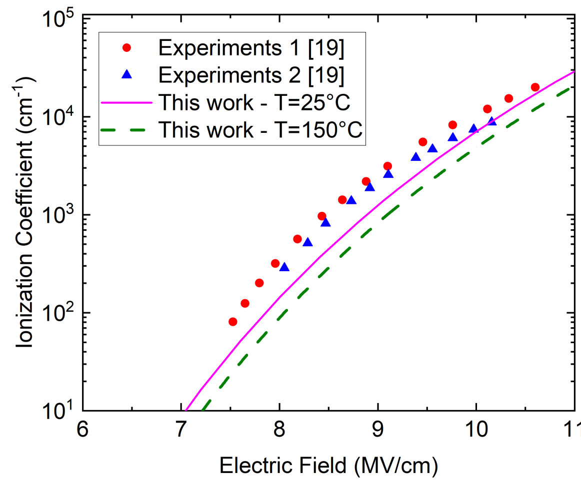

Figure 4.16: Electron avalanche coefficient as a function of the electric field at room temperature. Symbols: experimental data in [78]. Solid line: calibrated TCAD model at room temperature. Dashed line: calibrated TCAD model at $T = 150°C$.

As expected, a significant number of electron-hole pairs is generated by electron impact ionization at high electric fields, as reported in Fig. 4.17 where it can be noted that the avalanche generation rate in the intermediate-field regime ($F_{OX} = 6.5$ MV/cm) is up to 10 orders of magnitude greater than its low-field regime ($F_{OX} = 4$ MV/cm) counterpart. At large fields, namely $F_{OX} = 8.7$ MV/cm, the electron avalanche scattering rate is even greater and the ionization integral approaches the value of 1 corresponding to the breakdown condition.

The TCAD setup has been applied to reproduce the experimental data of the constant-current and the AC and DC stresses. To this purpose, a quasi stationary current ramp during which traps are forced to stay empty has been

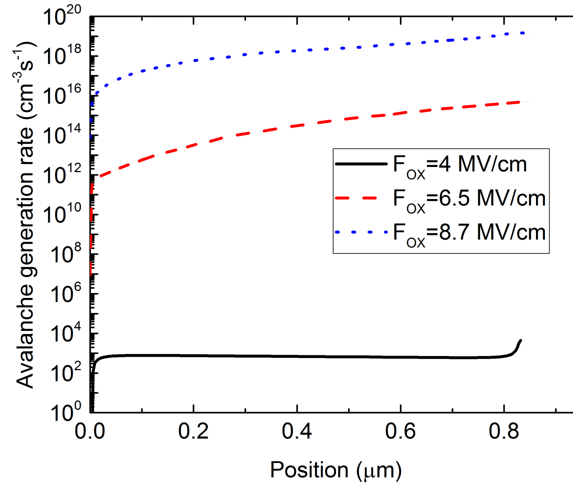

Figure 4.17: Electron avalanche scattering rate as a function of the position across the device thickness at $F_{0X} = 4$ MV/cm (low field regime), $F_{0X} = 6.5$ MV/cm (intermediate field regime) and $F_{0X} = 8.7$ MV/cm (high field regime).

applied up to the desired current level, then a constant-current stress is directly applied to the simulated device. Fig. 4.18 shows the TCAD results of the oxide field versus time at $T = 25$ °C and 150 °C. Experiments are qualitatively reproduced, indicating that the rate at which charge is trapped is in agreement with the experimental data, predicting E_{OX}^{BD} and the corresponding time to breakdown.

In order to gain insight on the internal phenomena producing the observed breakdown, the electric field distribution across the device is plotted at $T = 25$ °C, $J = 6.3 \cdot 10^{-8}$ A/cm^2 for three stress times, namely $t_1 = 1$s (at the beginning of the stress), $t_2 = 100$s (during the voltage increase) and $t_3 = 1000$s (after the breakdown condition is reached), as shown in Fig. 4.19. Charge injection from the top electrode ($x = 0$) leads to a charge trapping dynamics and a clear increase of the internal field towards the bottom contact. The maximum field reached near the bottom electrode at the longest time is as large as 10.5 MV/cm, comparable with the breakdown strength of bulk SiO_2 [78].

In order to further assess the role of trapping mechanisms in the observed constant-current TDDB dynamics, the trapped charge across the device has been extracted from simulations at $T = 25$ °C, $J = 6.3 \cdot 10^{-8}$ A/cm^2 at $t_1 = 1$, 100 and 1000 s, as shown in Fig. 4.20. It can be noted that at short stress times the trapped charge distribution is substantially flat across the device and simply tends to increase uniformly. Differently, at $t = 1000$ s the trapped charge is higher near both contacts with respect to the central portion of the

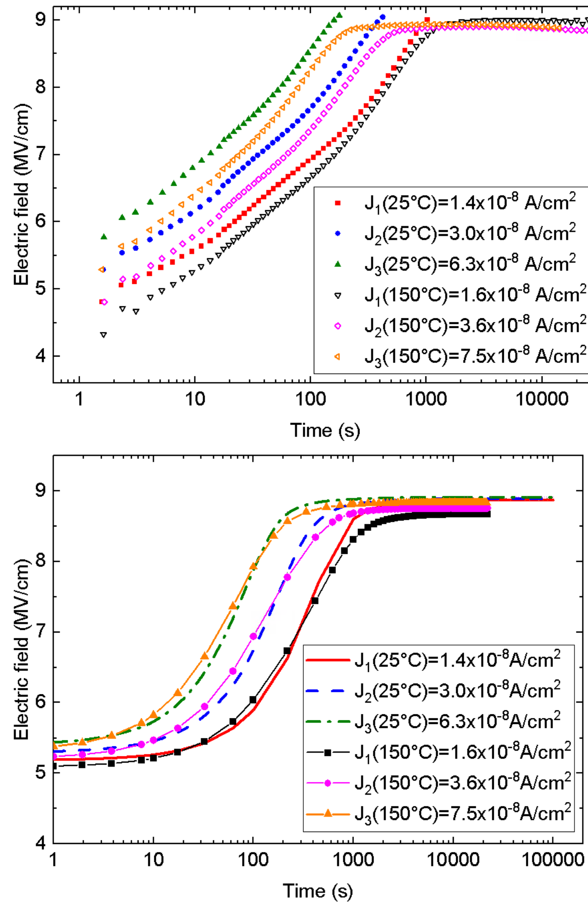

Figure 4.18: Experiments (left) and simulations (right) of the oxide field plotted as a function of time at different temperatures, namely $T = 25\ ^\circ\text{C}$ and $T = 150\ ^\circ\text{C}$ during the constant-current stress.

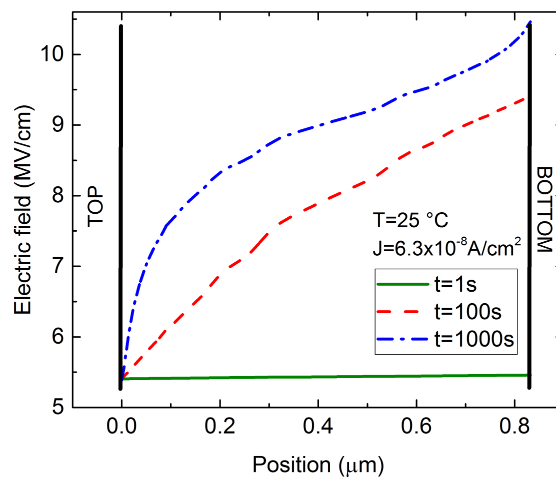

Figure 4.19: Electric field distribution across the device at $T = 25\ ^\circ\text{C}$ and $J = 6.3 \cdot 10^{-8}\ \text{A/cm}^2$ for three different stress times.

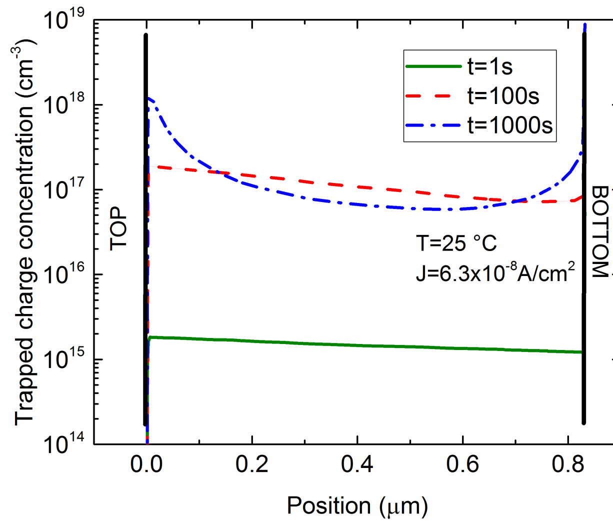

Figure 4.20: Total trapped charge across the device at $T = 25$ °C and $J = 6.3 \cdot 10^{-8}$ A/cm^2 for three different stress times.

device. The trapped charge in the proximity of the top contact is mainly due to electron injection from it: an accumulation of charges trapped in the defects is found in the region where the lowest electric field is observed, while a significant trapped-charge emission is expected to play its role at larger electric fields in the middle of the layer. On the other hand, the enhanced trapping near the bottom contact is an effect of avalanche generation which becomes relevant at long stress times due to the even larger field. In fact, the electrons are generated by impact ionization across the device especially near the anode. Those excess electrons can either be emitted from the bottom contact or be trapped, leading to an enhanced trapping concentration in the proximity of the bottom electrode.

This is further confirmed by the avalanche generation rate plotted in Fig. 4.21, where it can be noted that, for long stress times, the generation of electrons gradually increases moving towards the bottom contact. This means that the largest number of generated electrons is close to the bottom electrode.

Concerning the AC and DC stresses, a train of pulses with increasing amplitude as those shown in Fig. 3.8 (blue line) and a voltage ramp at a constant rate of 6 V/s have been applied to the simulated device, respectively. Fig. 4.22 shows the TCAD results of the current density versus the oxide field for the two stress conditions. The low-electric field ($F_{OX} < 6$ MV/cm) part of the characteristics is strictly related to the charge injection due to tunneling effect. The difference between simulations and measurements might be ascribed to

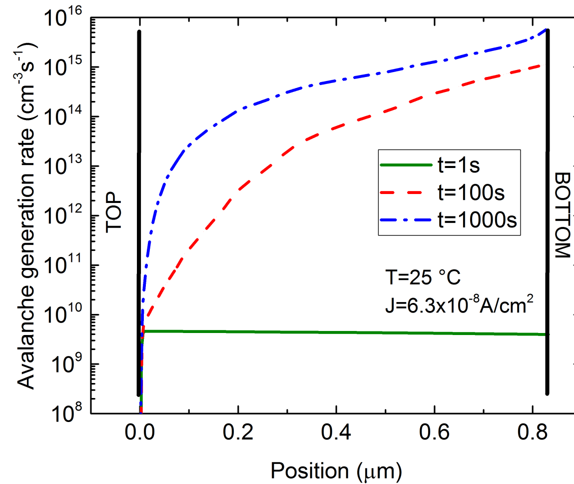

Figure 4.21: Avalanche generation rate across the device at $T = 25\ ^\circ\mathrm{C}$ and $J = 6.3 \cdot 10^{-8}\ \mathrm{A/cm^2}$ for three different stress times.

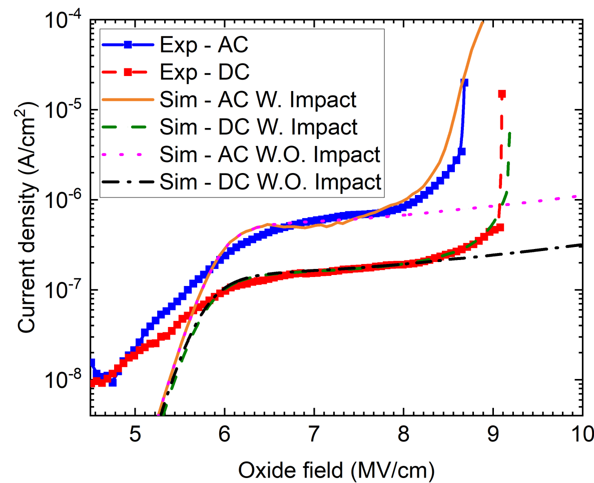

Figure 4.22: Current density as a function of the oxide field for the AC and DC voltage ramp stresses. Dots: Experiments. Solid lines: simulations with impact ionization (solid and dashed lines) and without (dotted and dash-dotted lines).

a perimeter contribution to the total current and trap assisted tunneling effects from the electrodes which are not taken into account in simulations. At intermediate electric fields (up to 8 MV/cm) the current is mainly limited by charge trapping effects. Simulations are in good agreement with experiments, indicating that the relevant charge trapping mechanisms are properly modeled and calibrated. In the high-field regime, namely over 8 MV/cm, the effect of impact ionization can be noted. The slight anticipation of the observed breakdown field in the AC regime with respect to the DC stress condition is nicely captured by simulations. Moreover, the breakdown is not

reproduced in the simulations performed without the avalanche model (dotted and dash-dotted lines of Fig. 4.22), confirming that impact ionization is the main cause of failure mechanisms in such devices.

The total trapped charge and the electric field across the device have been plotted in Fig. 4.23 and Fig. 4.24 at two different oxide fields, namely $F_{OX} = 6$ MV/cm (in the charge-trapping portion of the J-E characteristics) and $F_{OX} = 8.5$ MV/cm (just before the AC breakdown). The two stress conditions show different behaviors with some common features. In both stresses, even if the great majority of the total charge is already trapped at $F_{OX} = 6$ MV/cm ($N_T \approx 10^{16}$ cm^{-3}), charge buildup in the oxide continues until the breakdown condition is reached (Fig. 4.23). However, while the charge distribution in the DC regime is substantially flat at low fields, in the AC regime more charge is accumulated near both contacts, as expected, because charge is injected from both of them alternately. At high fields, the distribution in the DC case shows more trapped charge near the top contact as it is the cathode, while for the AC regime the distribution is similar to the low-field case with the trapped charge being greater near the two contacts with respect to the DC case.

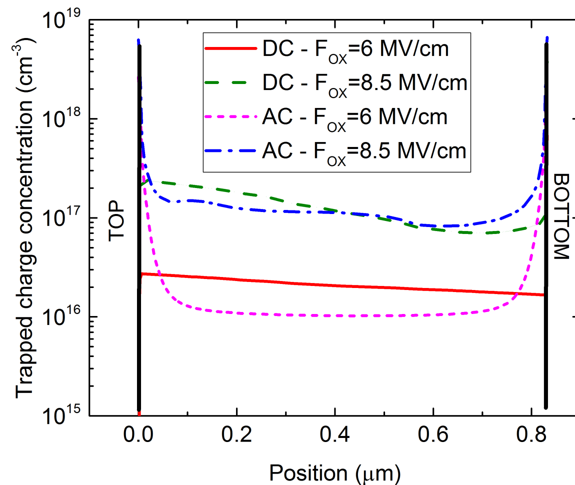

Figure 4.23: Trapped charge across the device under AC and DC regimes at two different oxide fields, namely $F_{OX} = 6$ MV/cm (in the cherge-trapping portion of the J-E characteristics) and $F_{OX} = 8.5$ MV/cm (just before the AC breakdown).

Concerning the electric-field distribution (Fig. 4.24), at low biases a nearly flat distribution for both the AC and DC regimes is observed, while at greater biases the trapped charge causes a modification of the local electric field, and

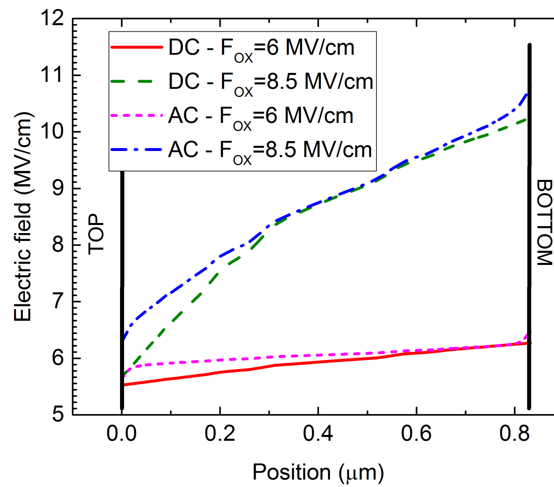

Figure 4.24: Electric field distribution across the device under AC and DC regimes at two different oxide fields, namely $F_{OX} = 6$ MV/cm (in the charge-trapping portion of the J-E characteristics) and $F_{OX} = 8.5$ MV/cm (just before the AC breakdown).

a greater field is observed in the AC regime with respect to the DC one especially near the contacts explaining why the AC breakdown is slightly anticipated.

Chapter 5

Thickness dependence of the breakdown in realistic structures

In order to have a realistic representation of the breakdown regime in thick oxides for galvanic insulation under different stress conditions, the physical mechanisms responsible of charge trapping and failure of the device must be taken into account, extending the analysis also to geometry factors which can further limit the device lifetime. Among them, the most relevant one is the oxide thickness, but also the electrode area and the corresponding corner effects should be taken into account. A more realistic 2D structure (very similar to the real one) has been used in this part of the work. The conduction model for SiO_2 is exactly the same as the one presented in the previous chapter of this thesis. Only a slight modification was necessary, that is the model of impact-ionization, as explained in the first section of this chapter. In the second section, the main results concerning the breakdown of thick TEOS 2-D structures under different stress conditions are presented and an extensive analysis on the mechanisms responsible of the observed effects is carried out.

5.1 2-D TCAD structure

In this part of the work a realistic 2-D structure, which is schematically shown in Fig. 5.1, has been used. The most relevant distances in the structure have been indicated in Fig. 5.1. An ideal insulator layer is placed on the top of the TEOS oxide. The distance between the ring contact and the top metal is at least 8 times the oxide thickness. Capacitors with different oxide thicknesses (t_{OX}) in the range between 1μm and 17μm have been investigated. A cylindrical symmetry has been assumed in order to predict the realistic 3-D circular structure, in particular the circular top metal electrode.

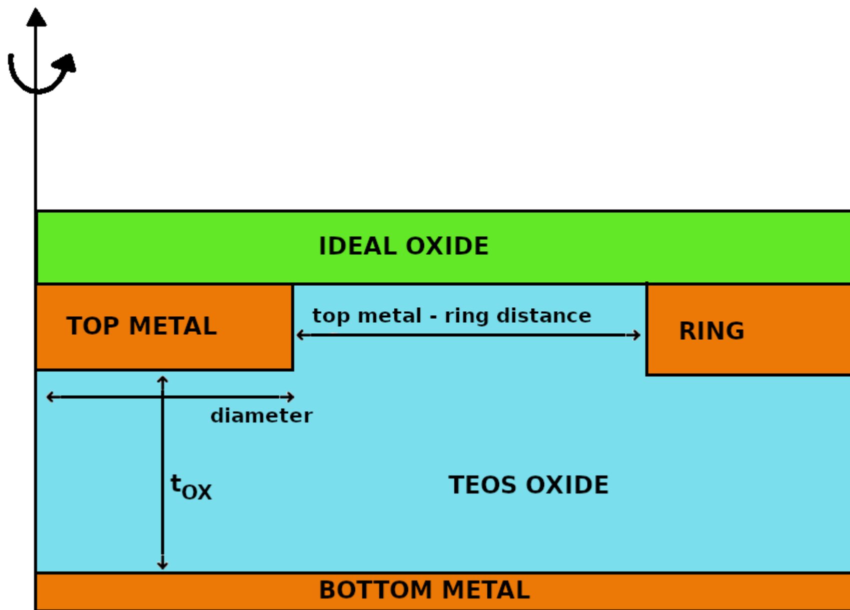

Figure 5.1: Schematic view of the 2D simulated structure of the TEOS capacitor (not in scale).

5.2 Modifications to the impact ionization model

Simulations on the 2-D structure have been performed using the same TCAD approach as that reported in Chapter 4 for the 1-D MIM structure. As a preliminary step, the Van Oververstraeten - De Man model has been activated to model the impact-ionization, but this led to several convergence issues. For this reason, simulations have been carried out in order to gain an insight of the role of the empirical impact ionization model. A detailed microscopic analysis has shown that the very large increase of the electric field in the proximity of the top metal corner (due to sharp-edges effects) leads to a non-limited increase of the exponential ionization-coefficient function when using the Van-Overstraeten model. Hence, the analysis has been extended to other impact ionization models available on the TCAD tool. In particular, the Okuto - Crowell model [81] has proven to give good results in terms of convergence as it allows to limit the increase of the ionization coefficient at very high fields. Moreover, the Okuto model is more accurate than the Van Overstraeten model from a physical point of view. Namely, the Van Overstraeten model has an empirical origin being based on the assumption that the functional dependence of the impact ionization coefficient α on the electric field F satisfies the Chynoweth's law:

$$\alpha = A(T) \exp\left(\frac{B(T)}{F}\right) \tag{5.1}$$

where the temperature-dependent coefficients A and B must be adjusted to match the measured data. Actually, also the Okuto model has an empirical origin, as the analytical expression of the avalanche coefficient is a trial function with the form:

$$\alpha = A(T)F^n \exp\left[-\left(\frac{B(T)}{F}\right)^m\right] \tag{5.2}$$

where A and B are temperature-dependent parameters to be adjusted and the choice of $n = 1$ and $m = 2$ was found to be the best for various semiconductor materials and temperatures [81]. However, the following analytic expression has been derived in [82] for the impact-ionization coefficient in silicon at high fields in terms of the electric field and lattice temperature:

$$\alpha \propto F \exp\left[-k(T)\left(\frac{F_{crit}}{F}\right)^2\right] \tag{5.3}$$

where k is a temperature-dependent factor and F_{crit} is the critical field. The derivation was made basing on physical grounds, without introducing a priori relations among the parameters. In [82], the microscopic impact-ionization scattering rate was derived from the solution of the Boltzmann transport equation (BTE) and only an approximation was made, that is, on the form of the electron distribution function $f(E)$. This validates existing models whose parameters were determined empirically, demonstrating that the Okuto model is more physically based than the Van Overstraeten model. It should be highlighted that, despite this change, the physics of the model remains substantially unaltered and also the results do not show appreciable changes.

In Fig. 5.2 the electron ionization coefficient is compared with the experimental data reported in [78]. Slight differences are observed between the experimental data and the calibrated Okuto TCAD model, especially at high electric fields. However, it should be pointed out that TEOS oxides tend to show different electrical properties with respect to thermally grown SiO_2, thus affecting also the impact ionization mechanism. No specific indication was found for the impact-ionization coefficient of holes, as avalanche is mostly due to electrons in SiO_2 [22]. The same ionization coefficient is thus used also for holes, assuming no relevant role given by asymmetric behavior.

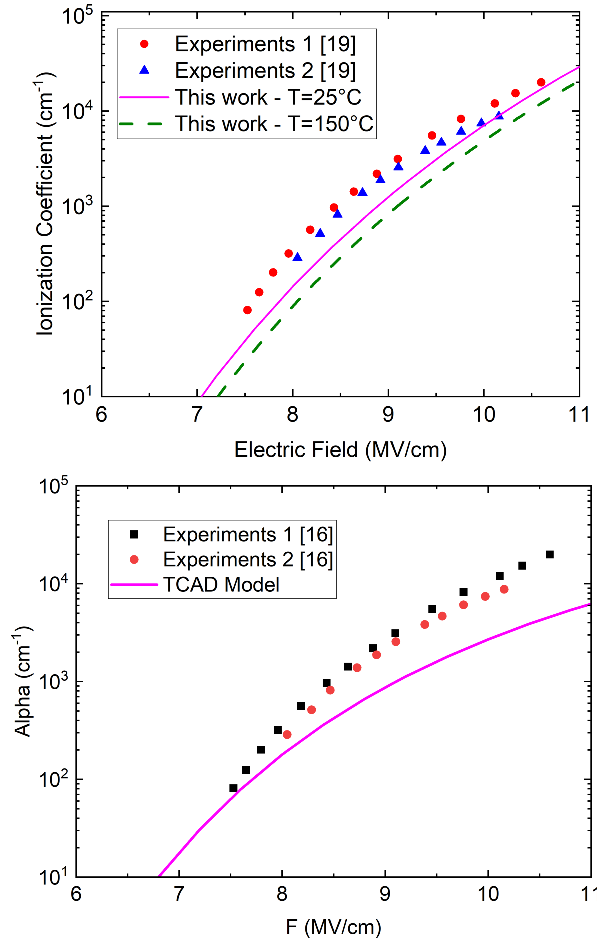

Figure 5.2: Electron avalanche coefficient as a function of the electric field.
Left: Experimental data in [78] and the calibrated Van Overstraeten model at room temperature (solid line) and at T = 150°C (dashed line).
Right: Experimental data in [78] and the calibrated Okuto model at room temperature.

5.3 Simulation results

Fig. 5.3 shows the TCAD results of the current density versus the oxide field at T = 25°C for the DC stress only. Experiments are qualitatively reproduced: the current level in the intermediate-field portion of the characteristics, the breakdown field and its slight dependence on the oxide thickness are correctly captured by simulations, indicating that the most relevant physical mechanisms have been taken into account and properly modeled. The slight underestimation of the current in the low-field portion of the characteristics with respect to the experiments can be ascribed to trap assisted tunneling from the electrodes which is not taken into account in simulations. The much

more abrupt onset of the avalanche breakdown of the thicker oxide with respect to the thinner one might be ascribed to very different spatial distributions of the trapped charges within the bulk of the oxide, in particular in the proximity of the top metal corner: a larger amount of trapped charge leads to a greater electric field in that region and thus to a less smooth behavior of the avalanche onset.

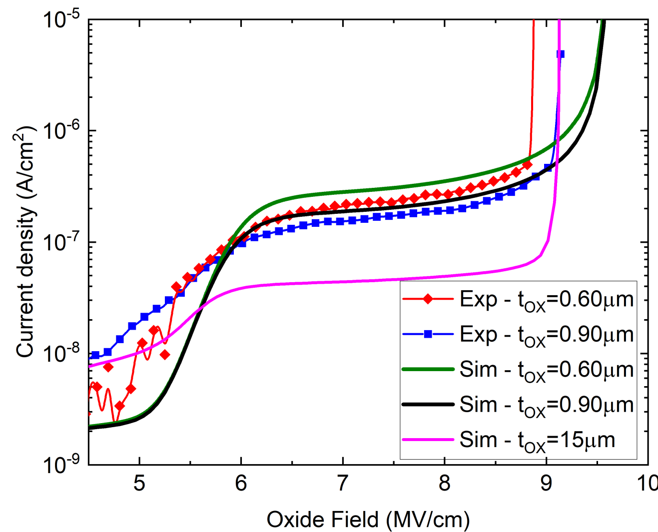

Figure 5.3: Current density as a function of the oxide field up to the breakdown for different oxide thickness. Symbols and lines: experiments. Lines: Simulations at $t_{OX} = 0.6\mu$m, $t_{OX} = 0.9\mu$m and $t_{OX} = 15\mu$m.

The predicted breakdown fields for both the AC and the DC stresses are reported in Fig. 5.4. Even if slight differences are found with respect to the experimental data, the overall dependence on the oxide thickness is fairly captured by simulations in a wide range of thicknesses and for both the stress conditions, indicating that impact ionization plays a relevant role in the breakdown of such devices along with the 2D effects at the corner of the structure as discussed in the following. In particular, the peculiar behavior under AC stress is fairly well reproduced by simulations allowing to gain further insight on the mechanisms responsible for the anticipated breakdown of the device under AC stress.

An analysis on the most relevant physical quantities such as the electric field and the trapped charge across the devices has been carried out through the TCAD results. In Fig. 5.5(A-C)(dimensions not in scale) the electric field during the DC stress at the biases corresponding to the onset of the avalanche breakdown are reported for the oxides with thicknesses 0.9μm and 15μm.

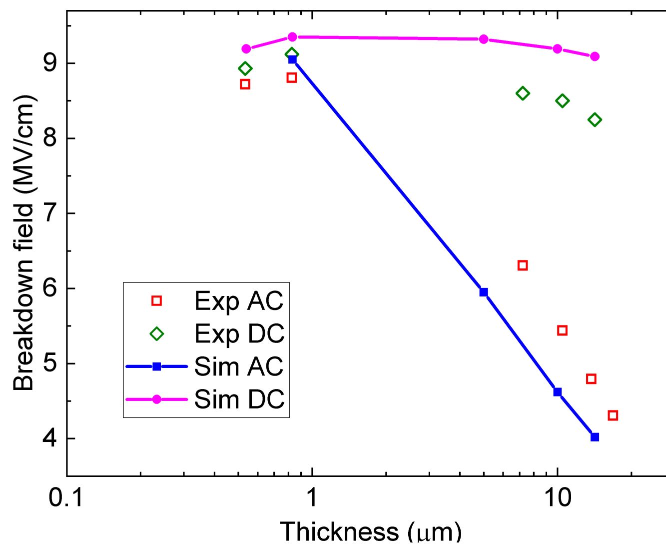

Figure 5.4: Breakdown field as a function of the oxide thickness for samples with thicknesses up to 15μm under AC and DC stresses. Dots: experiments. Lines and dots: Simulations.

The same scale is used on the Y axis of the different devices, while different scales have been used for the X axes due to the different thicknesses.

Firstly, it should be noted that the electric field distribution of the thinner oxide (Fig. 5.5 A) notably differs from that of the thicker oxide (Fig. 5.5 C). The thinner oxide approximately behaves like a one-dimensional parallel-plate capacitor, with the electric field being smaller near the cathode and becoming greater moving towards the anode due to the accumulated trapped charge. The onset of the breakdown is given by the critical electric field that reaches its maximum value in the proximity of the top metal corner and rapidly laterally decreases far from it. The maximum field sustained by the thinner oxide at the onset of the avalanche breakdown is about $E =$ 11MV/cm when an external nominal electric field $E_{OX} = 9.4$MV/cm is applied. The impact-ionization generation shows its maximum value at the corresponding maximum electric field. Avalanche is thus initiated by electrons flowing in the high field at the anode. The thicker oxide is characterized by having two electric field peaks: the first one is in the same position as the one of the thinner oxide, i.e., in the proximity of the anode (Fig. 5.5 C), while the second one is close to the top metal corner, with the high-electric field profile extending over a wide region of the device. The cutlines in the longitudinal direction at the top side of the capacitance show that the second peak gives rise to a significant impact-ionization generation, leading to a large amount of current density (Fig. 5.5 B-D). As a consequence, the breakdown field is substantially modulated by the electric field profile in the proximity of the

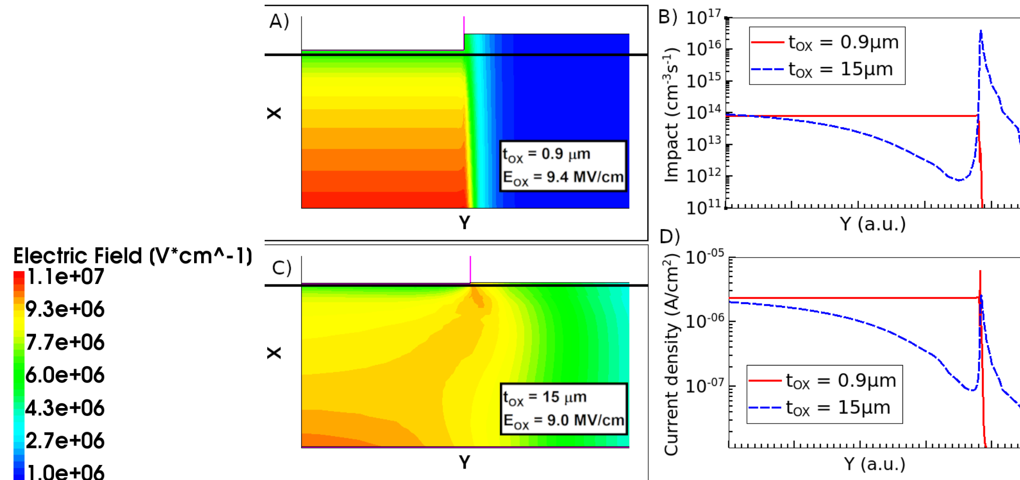

Figure 5.5: Electric field within the oxide layer for two thicknesses and cutlines of the impact-ionization generation rate and the current density along the Y axis (black lines in the leftmost figures).
A. Electric field distribution for $t_{OX} = 0.9\mu$m at $E_{OX} = 9.4$MV/cm (onset of avalanche breakdown).
B. Impact-ionization generation rate along the Y coordinate in proximity of the top metal contact.
C. Electric field distribution for $t_{OX} = 15\mu$m at $E_{OX} = 9.0$MV/cm (onset of avalanche breakdown).
D. Current density along the Y coordinate in proximity of the top metal contact.
X and Y axes have arbitrary units. The same scale is used on every Y axis, while different scales have been used for the X axes due to the different thicknesses. The distances from the two cutlines to the respective top metal contacts are the same. For the schematic of the structure, see Fig. 3.10.

corner.

5.3.1 TCAD analysis of the AC breakdown at different oxide thicknesses

In the same way, the electric field during the AC stress at different polarities and for different thicknesses is shown in Fig. 5.6. In order to fairly compare the two thicknesses, the same oxide field has been used, choosing the value of $E_{OX} = 3.8$MV/cm which is in the proximity of the breakdown of the thick oxide. The electric field profile of the thinner oxide resembles that of a one-dimensional parallel-plate capacitor for both the negative and positive polarity (Fig. 5.6 A-B). The high field region around the corner decreases of orders of magnitude far from it along the Y axis. Differently, in the thicker oxide, a geometry-related effect can be noted: the high-field region around

the corner extends for a wider region of the device for both polarities (Fig. 5.6 C-D).

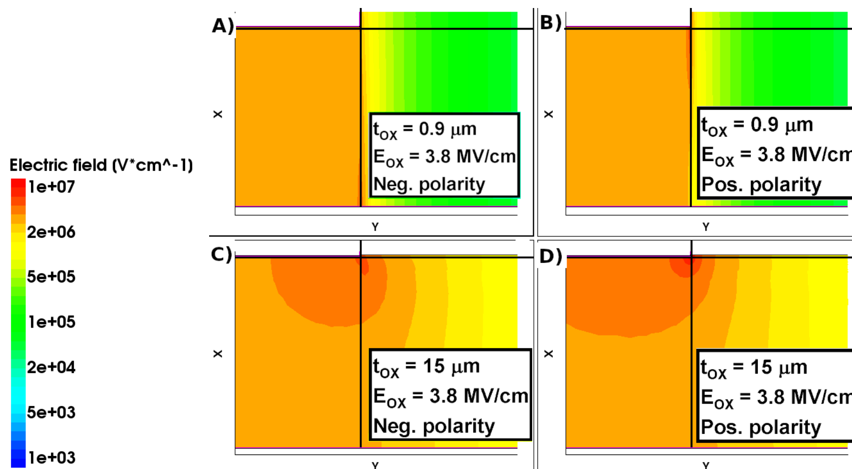

Figure 5.6: Electric field within the oxide layer for the oxides with thicknesses: $t_{OX} = 0.9\mu$m (A-B) and $t_{OX} = 15\mu$m (C-D) at positive and negative polarity during the AC stress. X and Y axes have arbitrary units. The same scale is used on every Y axis, while different scales have been used for the X axes due to the different thicknesses.

The difference is further highlighted in Fig. 5.7, where the electric field is plotted against the position along the Y axis, following the horizontal black line of Fig. 5.6: while the electric field in the thin oxide decreases of orders of magnitude for distances larger than the corner position (represented by the peak), in the thick oxide the electric field is still in the order of 1 MV/cm at several microns of distance from the corner along the Y axis (approximately 18μm from the peak). In addition, it can be noted that the electric field in the proximity of the corner is larger during the positive half-wave than during the negative half-wave.

In order to further investigate this aspect, in Fig. 5.8, the electric field profile along the X-axis cut line indicated Fig. 5.6 is reported in the case of the thick oxide ($t_{OX} = 15\mu$m). During the positive stress, the electric field peak at the top metal corner is much higher and more extended than during the negative stress, reaching the value of 14 MV/cm, exceeding the intrinsic breakdown strength of SiO_2. It is a hint that the breakdown is driven by the positive half-wave: the top metal, and thus the region in the proximity of the corner acts as the anode during the positive half-wave, thus featuring an increase of the electric field. During the negative half-wave, on the contrary, the high electric field region is in the proximity of the bottom metal, and it is reduced near the top metal which now acts as a cathode. However, being

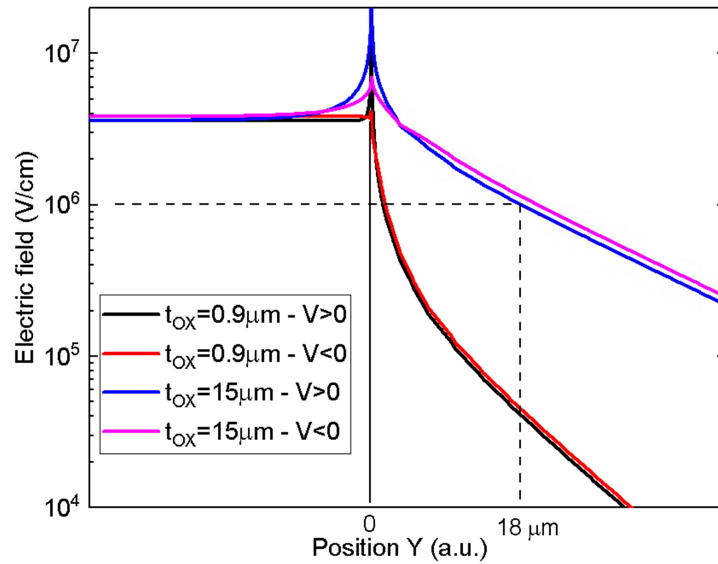

Figure 5.7: Electric field along the Y axis for two thicknesses at positive and negative polarity during the AC stress.

the bottom metal a simple plane contact, the increase of the electric field is limited and not enhanced by the presence of a corner, thus the electric field cannot be high enough to trigger the onset of the breakdown.

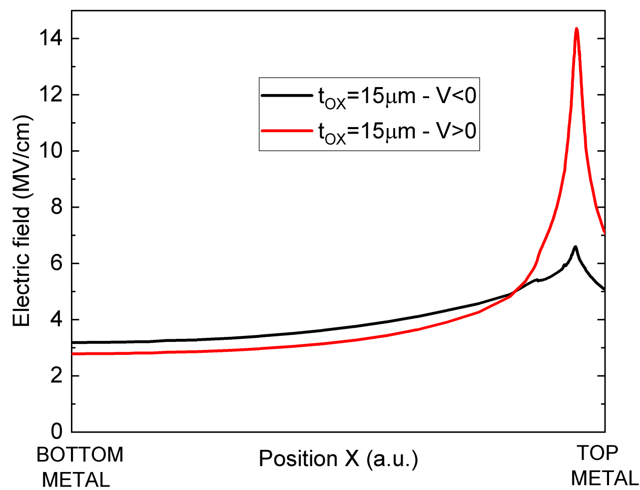

Figure 5.8: Electric field along the X axis for the oxide with $t_{OX} = 15\mu$m during the AC stress at negative and positive polarity.

The role of the top metal corner is clearly shown in Fig. 5.9 where the avalanche generation rate of the thick oxide is represented at the onset of the breakdown for the positive (Fig. 5.9, left) and negative polarity (Fig. 5.9, right). The fact that the breakdown field depends on the sign of the bias

applied to the MIM and to its thickness is a clear hint that not only the geometry, but also the thickness of the oxide itself plays a role in determining the breakdown of the device.

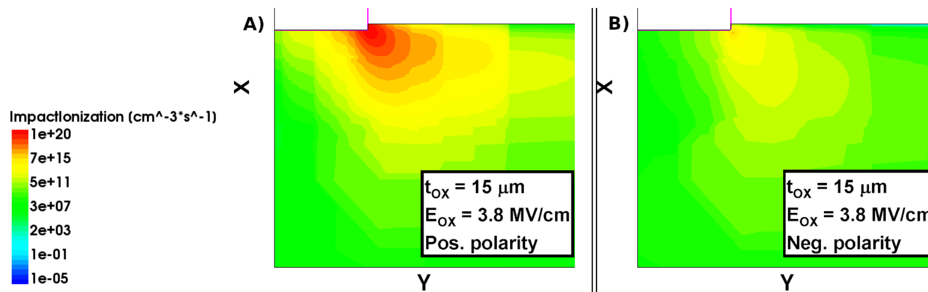

Figure 5.9: Impact ionization generation rate across the thick oxide ($t_{OX} = 15\mu$m) during the AC stress at $E_{OX} = 3.8$MV/cm for positive and negative polarity.

In order to further investigate the great difference of the breakdown field between the thick oxide and the thin oxide, in Fig. 5.10 the trapped charge is shown during the positive and the negative half-wave of the AC stress for the thicknesses 0.9μm and 15μm. In the thin oxide (Fig. 5.10 A-B) defects are almost uniformly charged through the entire thickness of the insulator in a region of limited extension around the top metal corner. On the contrary, in the thick oxide (Fig. 5.10 C-D) the traps are substantially empty over a great portion of the oxide thickness, and there is a significant trapped charge density only in the proximity of the top metal corner.

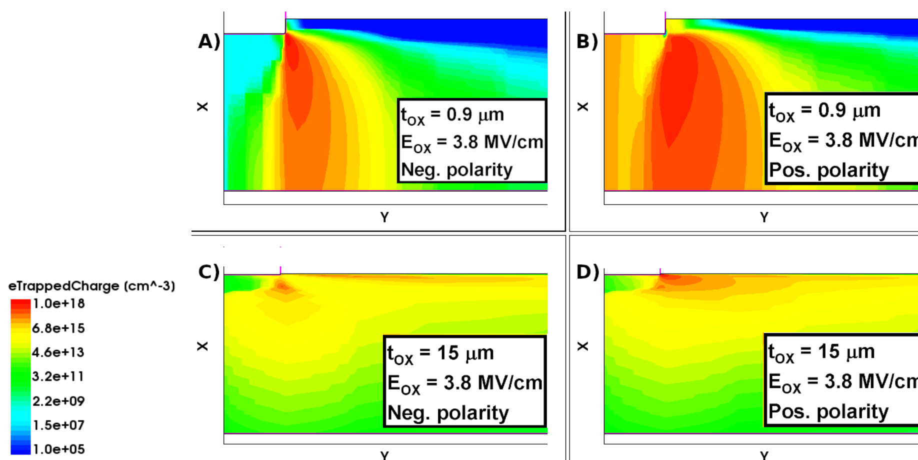

Figure 5.10: Trapped charge within the oxide layer for the oxides with thicknesses: $t_{OX} = 0.9\mu$m (A-B) and $t_{OX} = 15\mu$m (C-D) at positive and negative polarity during the AC stress. X and Y axes have arbitrary units. The same scale is used on every Y axis, while different scales have been used for the X axes due to the different thicknesses.

The distribution of the charged traps is further highlighted in Fig. 5.11 where the trapped charge density is plotted against the normalized position in the X axis (X_{norm}) along the vertical black lines of Fig. 5.6, where $X_{\text{norm}} = X/t_{\text{OX}}$ for both $t_{\text{OX}} = 0.9\mu\text{m}$ and $t_{\text{OX}} = 15\mu\text{m}$. We have to point out that during each half-wave the charge is trapped in a region of limited thickness around the cathode. This trapping length is in the order of $\approx 0.4\mu\text{m}$, a significant fraction the total thickness of the thin oxide. This means that the charged defects in thin oxide are distributed approximately in a uniform manner along the entire thickness of the oxide, as shown by the dashed lines of Fig. 5.11, leading to a limited increase of the electric field. As far as the thicker oxide is concerned, this trapping length represents only a small fraction of the total thickness of the device, implying that defects are almost empty throughout the oxide except in a small region around the top metal and in particular around the corner, as it can clearly be seen by the solid lines of Fig. 5.11. Hence, the electric field in this region is much increased if compared to the field built up in the same region of the thinner oxide.

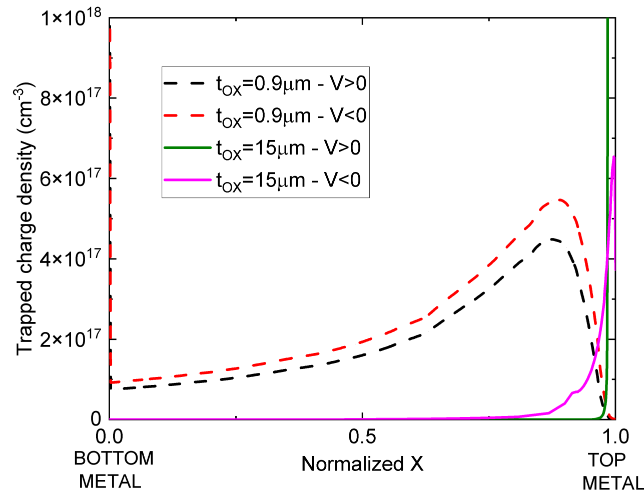

Figure 5.11: Trapped charge density along the normalized X axis (X_{norm}) during the AC stress at negative and positive polarity with $E_{\text{OX}} = 3.8\text{MV/cm}$. Dashed lines: $t_{\text{OX}} = 0.9\mu\text{m}$. Solid lines: $t_{\text{OX}} = 15\mu\text{m}$. The position $X_{\text{norm}} = 0$ corresponds to the bottom metal, the position $X_{\text{norm}} = 1$ corresponds to $X = t_{\text{OX}}$ (top metal).

It is clearly visible in Fig. 5.12 where the electric field is plotted against the normalized X-axis. In the thicker oxide, the electric field exhibits a sharp peak in the proximity of the top metal corner with a value of about 14 MV/cm, being relatively small in the bulk oxide, whereas in the thinner oxide the electric field is approximately constant through all the oxide thickness with a

smooth and rounded peak of about 4.5MV/cm, only slightly different from the oxide field $E_{OX} = 3.8$ MV/cm.

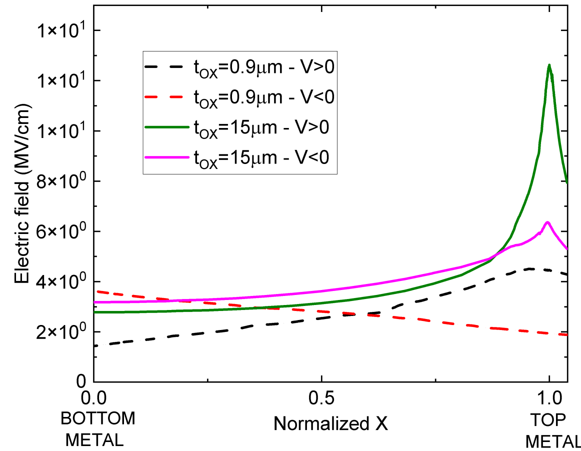

Figure 5.12: Electric field along the normalized X axis during the AC stress at negative and positive polarity with $E_{OX} = 3.8$MV/cm. Solid lines: $t_{OX} = 15\mu$m. Dashed lines: $t_{OX} = 0.9\mu$m. The position $X_{norm} = 0$ corresponds to the bottom metal, the position $X_{norm} = 1$ corresponds to $X = t_{OX}$ (top metal).

5.3.2 TCAD analysis of the breakdown under AC and DC stresses

A further comparison between the DC stress and the AC stress has been made to deeply understand the relevant differences between them. As a significant difference in the breakdown field is observed at large thicknesses, the oxide with $t_{OX} = 15\mu$m has been taken as a reference for this analysis.

In Fig. 5.13, the electric field during DC (Fig. 5.13 A-B) and AC (Fig. 5.13 C-D) stresses is compared for different biases. In order to have a fair comparison between oxides which show very different behaviors, two biases have been used for the DC case: $E_{OX} = 3.8$MV/cm, which is equal to the AC field and at the onset of AC breakdown and is far from the DC-breakdown and $E_{OX} = 8.8$MV/cm which is at the onset of the avalanche condition during the DC stress.

The DC-electric field profile at low fields (Fig. 5.13 A) is very similar to the AC profile during the negative half-wave (Fig. 5.13 D), with a relatively high-field region extending around the top metal corner but with maximum values that are not high enough to trigger on the breakdown, meaning that top metal

injection is a condition which cannot cause a premature breakdown of the device. Differently, at the same bias, the electric field around the corner during the positive half-wave of the AC stress (Fig. 5.13 C) is very high, reaching values of about 14MV/cm, explaining why we can reach breakdown even at such a low stress. We would like to highlight that simulations are performed using cylindrical coordinates, thus the dimensions of the regions that appear in two-dimensional charts are not in linear relation with the actual volumetric dimensions of the structure. The DC profile at high stresses (Fig. 5.13 B) is indeed different from all the other situations: the electric field is high over a very wide region of the device, but its peak is still lower than the peak of the AC stress represented on bottom-left. Nevertheless, the large extension of the region combined with high values of the electric field determines the breakdown of the device. Thus we can conclude that, even though in the bulk of the device the electric field is (relatively) low, a very high field (much greater than 10 MV/cm) in a small region of the device (small if compared to the total dimensions) is sufficient to cause the failure of the device. This condition can be reached even at very small values of the applied electric field because the high-field region around the corner is associated with a great increase of the impact-generation term, as shown in Fig. 5.14.

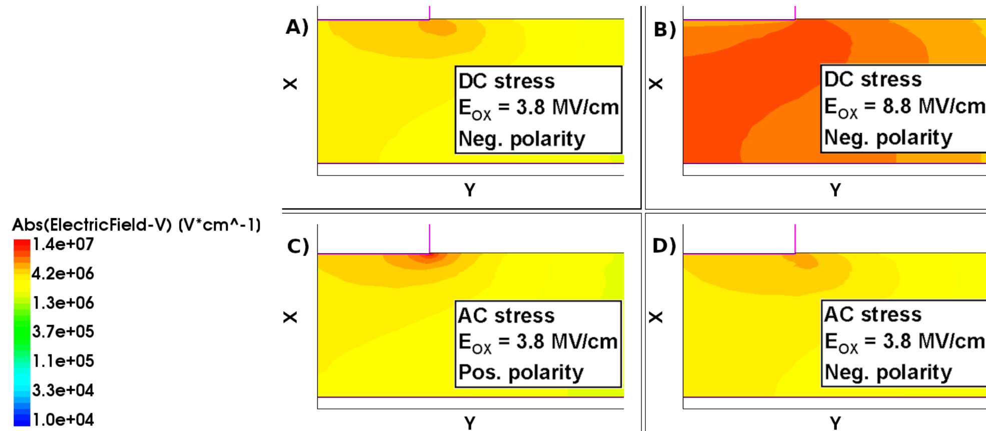

Figure 5.13: Electric field profile within the thick oxide ($t_{OX} = 15\mu$m) during AC and DC stresses.
A) DC stress at $E_{OX} = 3.8$MV/cm (far from breakdown) with negative polarity.
B) DC stress at $E_{OX} = 8.8$MV/cm (onset of avalanche breakdown) with negative polarity.
C-D) AC stress at $E_{OX} = 3.8$MV/cm with positive and negative polarity, respectively.

At small values of E_{OX}, the impact-ionization profile in the DC case is

very similar to the AC profile during the negative half-wave, with a relatively high-impact region extending around the top metal corner, because the electric field (not shown) has a maximum value of about 6MV/cm, not enough to trigger on the breakdown . Differently, at the same bias, the electric field around the corner during the positive half-wave of the AC stress is very high, with a maximum value of about 14MV/cm, explaining why the impact-ionization generation can reach values as high as 10^{20}cm^{-3}s^{-1}, thus leading to the breakdown of the device. The DC profile at high stresses (5.14 B) is indeed different from all the other situations: the impact-ionization is high over a very wide region of the device, but its peak is still lower than the peak of the AC stress (5.14 C). Nevertheless, breakdown can take place also at lower values of the maximum electric field (which must be comparable with the breakdown strength of SiO_2), but with a greater extension of the high-field profile region.

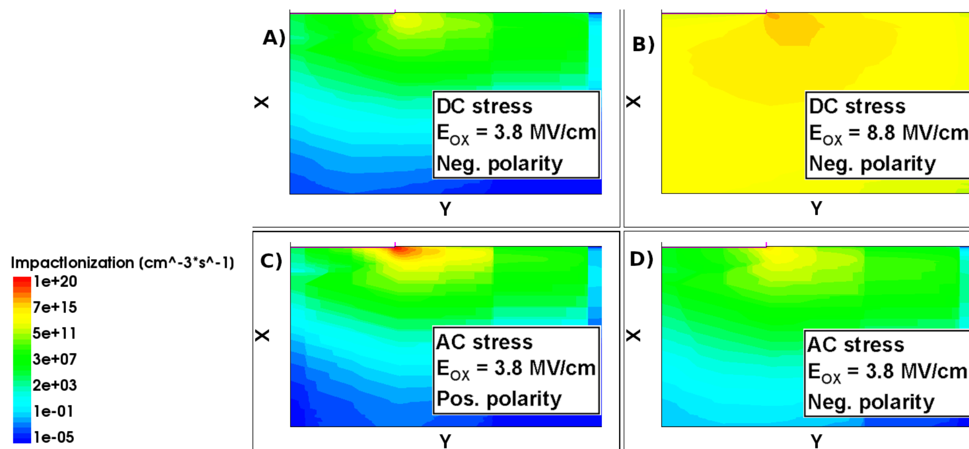

Figure 5.14: Impact ionization generation rate within the thick oxide ($t_{OX} = 15\mu$m) during AC and DC stresses.
A) DC stress at $E_{OX} = 3.8$MV/cm (far from breakdown) with negative polarity.
B) DC stress at $E_{OX} = 8.8$MV/cm (onset of avalanche breakdown) with negative polarity.
C) AC stress at $E_{OX} = 3.8$MV/cm with positive polarity.
D) AC stress at $E_{OX} = 3.8$MV/cm with negative polarity.

In order to have a complete representation of the situation, the trapped charge has been represented for both the AC and DC stresses as shown in Fig. 5.15. The stress conditions represented are the same as those of Fig. 5.13. During the DC stress a trapping dynamics is observed, as shown by the uppermost charts of Fig. 5.15: the trapped charge simply increases with time during the negative unipolar stress, in particular in the proximity of the top metal corner. The dynamics observed during an AC stress is more

complicated (Fig. 5.15, bottom), as the polarity change makes charges to trap and partially de-trap very fast. Except ofr a small region around the corner, traps are less charged than at the same stress condition of a DC stress. In particular, we can observe that a much lesser amount of charge is trapped in the proximity of the two contacts with respect to the DC regime, due to the fast de-trapping. In addition, more charge is trapped in the negative half-period than in the positive half-period, meaning that, on average, a grater current flows through the insulator during the negative half-wave.

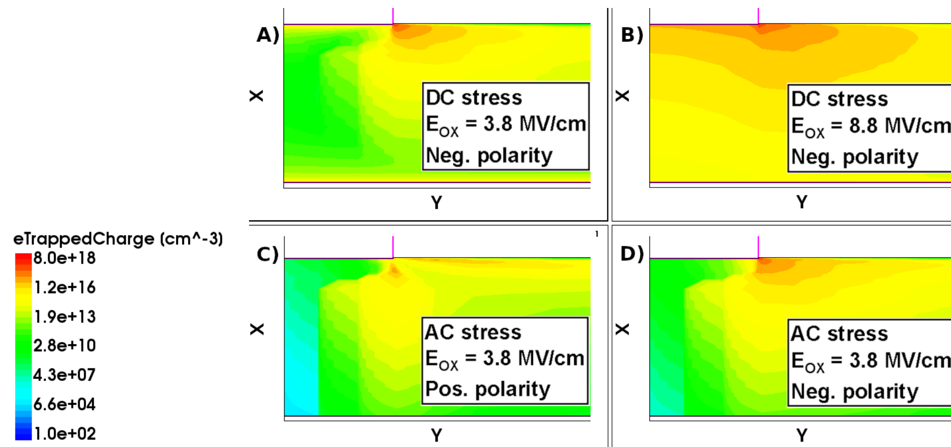

Figure 5.15: Trapped charge in the thick oxide ($t_{OX} = 15\mu$m) during AC and DC stresses.
A) DC stress at $E_{OX} = 3.8$MV/cm (far from breakdown) with negative polarity.
B) DC stress at $E_{OX} = 8.8$MV/cm (onset of avalanche breakdown) with negative polarity.
C-D) AC stress at $E_{OX} = 3.8$MV/cm with positive and negative polarity, respectively.

Chapter 6

Conclusions

Silicon dioxide (SiO_2) is the main insulator in the electronic industry because of its near-ideal properties; however, the degradation and failure of MIM devices is still limited by charge buildup in pre-existing defect sites of the oxide layer. For this reason, a detailed knowledge of charge injection and transport mechanisms of such materials under high electric fields plays a key role in improving the reliability of such devices. Since stacked dielectrics have long been used in commercial products, the reliability of the technology is empirically well established, but very few works are based on a self-consistent theoretical framework. For such reasons, a TCAD-based model of charge transport capable of correctly handling charge injection, trapping and de-trapping mechanisms and avalanche onset in bulk SiO_2 oxides is highly desirable as it would be a key instrument for the development and optimization of ultra-compact capacitances in integrated high-voltage systems.

In this thesis, a TCAD model has been presented to investigate conduction mechanisms in high-voltage silicon oxide thick TEOS capacitors embedded in the back-end inter-level dielectric layers for galvanic insulation applications. The TCAD framework has been proven to be a useful tool for the study of transport in oxides. The most important conduction mechanisms, i.e., charge injection processes at the electrodes and trap-assisted capture and emission processes, have been modeled in order to reproduce the electrical behavior of the device in different stress conditions: constant voltage stress, AC stress and voltage ramps. The role of traps has been extensively investigated. Since it is not possible to determine unambiguously the exact nature of defects, being silicon oxide an amorphous material and the type of traps being process-dependent, it has been shown that it is possible to reproduce the leakage current of thick capacitors with a proper choice of trap parameters, such as concentration, capture cross section and energy level. Two uniform distributions with an energy width of 0.5 eV each and mean energies $E_1 = 6.3$ eV and $E_2 = 6.5$ eV with respect to the top of the valence band have

been defined. By analyzing the DC-stress characteristics, it has been possible to calibrate the concentration and the cross section of such traps. In addition, our choice of trap parameters is in quite good agreement with the theoretical results reported in recent theoretical studies.

Different stress conditions, such as constant-current time dependent dielectric breakdown and AC and DC voltage ramp stresses up to breakdown, have been analyzed in order to investigate the role of the main physical mechanisms involved in the breakdown of such devices. The reported predictions are in nice agreement with experiments up to the breakdown condition. From the comparison of TCAD simulations with experiments, we can conclude that impact-ionization is the most relevant mechanism involved in the breakdown of such devices.

After having modeled the main physical mechanisms responsible of the conduction and the breakdown in SiO_2 TEOS oxide using a simple parallel plate capacitor as test structure, the analysis has then been focused on the breakdown under different stress conditions in realistic 2-D structures with thicknesses in the range from 1μm to 15μm. The breakdown of such devices is strongly affected by the applied stress condition. Numerical simulations capture the overall thickness dependence of the breakdown field under AC and DC stress conditions, showing that not only the geometry of the structure, but also the thickness of the sample are responsible of a strong decrease of the breakdown field under an AC stress. The numerical analysis on realistic 2-D structures has shown that charge injection by tunneling and charge accumulation at defect sites in a limited region of the device are responsible for a large increase of the electric field which triggers impact ionization causing the anticipated failure of the device.

Bibliography

[1] S. Shin, Y. Chen, W. Ahn, *et al.*, "High voltage time-dependent dielectric breakdown in stacked intermetal dielectric," in *IEEE 56th Annual International Reliability Physics Symposium, Burlingame, CA, USA*, IEEE, 2018, P–GD.9–1–P–GD.9–5. DOI: 10.1109/IRPS.2018.8353669.

[2] C. C. Hung, A. S. Oates, H. C. Lin, *et al.*, "New understanding of metal-insulator-metal (mim) capacitor degradation behavior," in *IEEE 45th Annual International Reliability Physics Symposium, Phoenix, AZ, USA*, IEEE, 2007, pp. 630–631. DOI: 10.1109/RELPHY.2007.369985.

[3] P. Mahalingam, D. Guiling, and S. Lee, "Manufacturing challenges and method of fabrication of on-chip capacitive digital isolators," in *IEEE International Symposium on Semiconductor Manufacturing, Santa Clara, CA, USA*, IEEE, 2007, pp. 1–4. DOI: 10.1109/ISSM.2007.4446870.

[4] R. Higgins and J. McPherson, "Tddb evaluations and modeling of very high-voltage (10 kv) capacitors," in *IEEE 47th Annual International Reliability Physics Symposium, Montreal, QC, Canada*, IEEE, 2009, pp. 432–436. DOI: 10.1109/IRPS.2009.5173292.

[5] W. Wu, S. Rojas, S. Manzini, A. Modelli, and D. Re, "Characterization of sio_2 films deposited by pyrolysis of tetraehylorthosilicate (teos)," *Journal de Physique Colloques*, vol. 49, pp. C4–397–C4–400, 1988. DOI: 10.1051/jphyscol:1988483.

[6] M. Sometani, R. Hasunuma, M. Ogino, H. Kuribayashi, Y. Sugahara, and K. Yamabe, "Suppression of leakage current of deposited sio_2 with bandgap increasing by high temperature annealing," *ECS Transactions*, vol. 19, pp. 403–413, 2009. DOI: 10.1149/1.3122105.

[7] E. Runnion, S. Gladstone, R. Scott, D. Dumin, L. Lie, and J. Mitros, "Thickness dependence of stress-induced leakage currents in silicon oxide," *IEEE Transactions On Electron Devices*, vol. 44, no. 6, pp. 993–1001, 1997. DOI: 10.1109/16.585556.

[8] T.H.Chiang and J.F.Wager, “Electronic conduction mechanisms in insulators,” *IEEE Transactions On Electron Devices*, vol. 65, no. 1, pp. 223–230, 2018. DOI: 10.1109/TED.2017.2776612.

[9] P. M. Lenahan and P. V. Dressendorfer, “Hole traps and trivalent silicon centers in metal/oxide/silicon devices,” *Journal of Applied Physics*, vol. 55, pp. 3495–3499, 1984. DOI: 10.1063/1.332937.

[10] W.D.Zhang, J.F.Zhang, M.Lalor, D.Burton, G.V.Groeseneken, and R.Degraeve, “Two types of neutral electron traps generated in the gate silicon dioxide,” *IEEE Transactions On Electron Devices*, vol. 49, no. 11, pp. 1868–1875, 2002. DOI: 10.1109/TED.2002.804709.

[11] D. J. DiMaria and J. W. Stasiak, “Trap creation in silicon dioxide produced by hot electrons,” *Journal of Applied Physics*, vol. 65, no. 6, pp. 2342–2356, 1989. DOI: 10.1063/1.342824.

[12] W. Goes, Y. Wimmer, A. El-Sayed, *et al.*, “Identification of oxide defects in semiconductor devices: A systematic approach linking dft to rate equations and experimental evidence,” *Microelectronics Reliability*, vol. 87, pp. 286–320, 2018. DOI: 10.1016/j.microrel.2017.12.021.

[13] E. H. Poindexter, G. J. Gerardi, M. Rueckel, P. J. Caplan, N. M. Johnson, and D. K. Biegelsen, “Electronic traps and pb centers at the si/sio_2 interface: Band-gap energy distribution,” *Journal of Applied Physics*, vol. 56, no. 10, pp. 2844–2849, 1984. DOI: 10.1063/1.333819.

[14] J. M. M. de Nijs, K. G. Druijf, V. V. Afanas'ev, E. van der Drift, and P. Balk, “Hydrogen induced donor-type si/sio_2 interface states,” *Applied Physics Letters*, vol. 65, no. 19, pp. 2428–2430, 1994. DOI: 10.1063/1.112696.

[15] D. Buchanan, M. Fischetti, and D. Dimaria, “Coulombic and neutral electron trapping centers in sio_2,” *Applied Surface Science*, vol. 39, no. 1, pp. 420–428, 1989. DOI: 10.1016/0169-4332(89)90459-5.

[16] T. Yang, C. Shen, M. Li, *et al.*, “Fast dnbti components in p-mosfet with sion dielectric,” *IEEE Electron Device Letters*, vol. 26, no. 11, pp. 826–828, 2005. DOI: 10.1109/LED.2005.857684.

[17] L. Vandelli, A. Padovani, L. Larcher, R. G. Southwick, W. B. Knowlton, and G. Bersuker, “A physical model of the temperature dependence of the current through sio_2/ hfo_2 stacks,” *IEEE Transactions on Electron Devices*, vol. 58, no. 9, pp. 2878–2887, 2011. DOI: 10.1109/TED.2011.2158825.

[18] J. Robertson, "High dielectric constant gate oxides for metal oxide si transistors," *Reports on progress in Physics*, vol. 69, no. 2, p. 327, 2005. DOI: 10.1088/0034-4885/69/2/R02.

[19] E. Y. Wu, W. L. Lai, M. Khare, *et al.*, "Polarity-dependent oxide breakdown of nfet devices for ultra-thin gate oxide," *2002 IEEE International Reliability Physics Symposium. Proceedings. 40th Annual (Cat. No.02CH37320)*, pp. 60–72, 2002. DOI: 10.1109/RELPHY.2002.996611.

[20] E. Ogawa, J. Kim, G. Haase, H. Mogul, and J. McPherson, "Leakage, breakdown, and tddb characteristics of porous low-k silica-based interconnect dielectrics," in *2003 IEEE International Reliability Physics Symposium Proceedings, 2003. 41st Annual.*, 2003, pp. 166–172. DOI: 10.1109/RELPHY.2003.1197739.

[21] R. Degraeve, J. Ogier, R. Bellens, P. Roussel, G. Groeseneken, and H. Maes, "A new model for the field dependence of intrinsic and extrinsic time-dependent dielectric breakdown," *IEEE Transactions on Electron Devices*, vol. 45, no. 2, pp. 472–481, 1998. DOI: 10.1109/16.658683.

[22] D. J. DiMaria, E. Cartier, and D. Arnold, "Impact ionization, trap creation, degradation, and breakdown in silicon dioxide films on silicon," *Journal of Applied Physics*, vol. 73, no. 7, pp. 3367–3384, 1993. DOI: 10.1063/1.352936.

[23] D. N. Chen and Y. C. Cheng, "A new model for dielectric-breakdown phenomenon in silicon dioxide films," *Journal of Applied Physics*, vol. 61, no. 4, pp. 1592–1600, 1987. DOI: 10.1063/1.338096.

[24] X. Jin, M. Masuduzzaman, S. H. Shin, S. Palit, and M. A. Alam, *Time-dependent gate oxide breakdown lab*, 2015. DOI: doi:10.4231/D3JD4PQ3W. [Online]. Available: https://nanohub.org/resources/tddb.

[25] U. Sharma, G. Kumar, S. Mishra, and R. Thomas, "Advancement of gate oxides from sio_2 to high-k dielectrics in microprocessor and memory," *Journal of Physics: Conference Series*, vol. 2267, no. 1, pp. 012142 1–7, 2022. DOI: 10.1088/1742-6596/2267/1/012142.

[26] M. Morgen, E. T. Ryan, J.-H. Zhao, C. Hu, T. Cho, and P. S. Ho, "Low dielectric constant materials for ulsi interconnects," *Annual Review of Materials Science*, vol. 30, no. 1, pp. 645–680, 2000. DOI: 10.1146/annurev.matsci.30.1.645.

[27] N. C. Norman, *Periodicity and the s- and p-Block Elements*. Oxford Chemistry Primers, 1997, pp. 50–52.

[28] V. A. Gritsenko, "Atomic structure of the amorphous nonstoichiometric silicon oxides and nitrides," *Physics-Uspekhi*, vol. 51, no. 7, p. 699, 2008. DOI: 10.1070/PU2008v051n07ABEH006592.

[29] S. Nekrashevich and V. Gritsenko, "Electronic structure of silicon dioxide (a review)," *Physics of the Solid State*, vol. 56, no. 2, pp. 207–222, 2014. DOI: 10.1134/S106378341402022X.

[30] R. P. Gupta, "Electronic structure of crystalline and amorphous silicon dioxide," *Phys. Rev. B*, vol. 32, pp. 8278–8292, 12 1985. DOI: 10.1103/PhysRevB.32.8278.

[31] H. Philipp, "Optical properties of non-crystalline si, sio, siox and sio2," *Journal of Physics and Chemistry of Solids*, vol. 32, no. 8, pp. 1935–1945, 1971. DOI: https://doi.org/10.1016/S0022-3697(71)80159-2.

[32] J. F. Verwey, E. A. Amerasekera, and J. Bisschop, "The physics of sio_2 layers," *Reports on Progress in Physics*, vol. 53, no. 10, p. 1297, 1990. DOI: 10.1088/0034-4885/53/10/002.

[33] M. V. Fischetti, D. J. DiMaria, S. D. Brorson, T. N. Theis, and J. R. Kirtley, "Theory of high-field electron transport in silicon dioxide," *Phys. Rev. B*, vol. 31, pp. 8124–8142, 12 1985. DOI: 10.1103/PhysRevB.31.8124.

[34] D. DiMaria and M. Fischetti, "Hot electrons in silicon dioxide: Ballistic to steady-state transport," *Applied Surface Science*, vol. 30, no. 1, pp. 278–297, 1987. DOI: https://doi.org/10.1016/0169-4332(87)90103-6.

[35] F.-C. Chiu, "A review on conduction mechanisms in dielectric films," *Advances in Materials Science and Engineering*, vol. 2014, 2014. DOI: 10.1155/2014/578168.

[36] S. Sze, Y. Li, and K. Ng, *Physics of semiconductor devices*. John Wiley and Sons, 2021.

[37] D. Schroder, *Semiconductor material and device characterization*. John Wiley and Sons, 2006.

[38] M. Stadele, F. Sacconi, A. Di Carlo, and P. Lugli, "Enhancement of the effective tunnel mass in ultrathin silicon dioxide layers," *Journal of Applied Physics*, vol. 93, pp. 2681–2690, Mar. 2003. DOI: 10.1063/1.1541107.

[39] T. F. C. Hamann H. Burghardt, *Electrical conduction mechanisms in solids*. Berlin : VEB Deutscher Verlag der Wissenschaften, 1988.

[40] M. A. Lampert, "Simplified theory of space-charge-limited currents in an insulator with traps," *Phys. Rev.*, vol. 103, pp. 1648–1656, 6 1956. DOI: 10.1103/PhysRev.103.1648.

[41] N. F. Mott and E. A. Davis, *Electronic Processes in Non-Crystalline Materials*. Oxford University Press, Oxford, UK, 1979.

[42] J. D. Jackson, *Classical electrodynamics*. John Wiley and Sons, 1999.

[43] M. Rudan, *Physics of semiconductor devices*. Springer, 2015.

[44] P. C. Arnett, "Transient conduction in insulators at high fields," *Journal of Applied Physics*, vol. 46, pp. 5236–5243, 1975. DOI: 10.1063/1.321592.

[45] P. A. Martin, B. G. Streetman, and K. Hess, "Electric field enhanced emission from non-coulombic traps in semiconductors," *Journal of Applied Physics*, vol. 52, no. 12, pp. 7409–7415, 1981. DOI: 10.1063/1.328731.

[46] E. Rosencher, V. Mosser, and G. Vincent, "Transient-current study of field-assisted emission from shallow levels in silicon," *Physical Review B*, vol. 29, pp. 1135–1147, 3 1984. DOI: 10.1103/PhysRevB.29.1135.

[47] S. Inc., "Sentaurus device user guide," Tech. Rep. R-2021.09, 2021.

[48] A. Mahajan, L. Patil, J. Bange, and D. Gautam, "Growth of sio2 films by teos-pecvd system for microelectronics applications," *Surface and Coatings Technology*, vol. 183, no. 2, pp. 295–300, 2004. DOI: https://doi.org/10.1016/j.surfcoat.2003.09.056.

[49] M. Sometani, R. Hasunuma, M. Ogino, H. Kuribayashi, Y. Sugahara, and K. Yamabe, "Improvement of dielectric properties on deposited sio2 caused by stress relaxation with thermal annealing," *Japanese Journal of Applied Physics*, vol. 48, no. 5S1, 05DB03–1 –05DB03–4, 2009. DOI: 10.1143/JJAP.48.05DB03.

[50] K. Okada, K. Narita, M. Kamei, S. Ohno, Y. Ito, and S. Suzuki, "Generalized model of dielectric breakdown for thick and thin sio_2 and si_3n_4 films combining percolation model and constant- Δe model," in *2017 IEEE International Reliability Physics Symposium (IRPS)*, 2017, 5B–2.1–5B–2.5. DOI: 10.1109/IRPS.2017.7936324.

[51] J. J. O'Dwyer, "Current-voltage characteristics of dielectric films," *Journal of Applied Physics*, vol. 37, no. 2, pp. 599–601, 1966. DOI: 10.1063/1.1708222.

[52] R. I. Frank and J. G. Simmons, "Space-charge effects on emission-limited current flow in insulators," *Journal of Applied Physics*, vol. 38, no. 2, pp. 832–840, 1967. DOI: 10.1063/1.1709421.

[53] D. L. Pulfrey, A. H. M. Shousha, and L. Young, "Electronic conduction and space charge in amorphous insulating films," *Journal of Applied Physics*, vol. 41, no. 7, pp. 2838–2843, 1970. DOI: 10.1063/1.1659325.

[54] S. Kanitz, "Charge transport in thick sio2-based dielectric layers," *Solid-State Electronics*, vol. 41, no. 12, pp. 1895–1902, 1997. DOI: https://doi.org/10.1016/S0038-1101(97)00163-9.

[55] C. Schleich, D. Waldhör, T. Knobloch, *et al.*, "Single-versus multi-step trap assisted tunneling currents - part i: Theory," *IEEE Transactions on Electron Devices*, vol. 69, no. 8, pp. 4479–4485, 2022. DOI: 10.1109/TED.2022.3185966.

[56] T. Grasser, T.-W. Tang, H. Kosina, and S. Selberherr, "A review of hydrodynamic and energy-transport models for semiconductor device simulation," *Proceedings of the IEEE*, vol. 91, no. 2, pp. 251–274, 2003. DOI: 10.1109/JPROC.2002.808150.

[57] R. J. Powell and M. Morad, "Optical absorption and photoconductivity in thermally grown sio_2 films," *Journal of Applied Physics*, vol. 49, no. 4, pp. 2499–2502, 1978. DOI: 10.1063/1.325099.

[58] V. Astašauskas, A. Bellissimo, P. Kuksa, C. Tomastik, H. Kalbe, and W. Werner, "Optical and electronic properties of amorphous silicon dioxide by single and double electron spectroscopy," *Journal of Electron Spectroscopy and Related Phenomena*, vol. 241, pp. 1–7, 2019. DOI: 10.1016/j.elspec.2019.02.008.

[59] N. Bhat, P. Apte, and K. Saraswat, "Charge trap generation in lpcvd oxides under high field stressing," *IEEE Transactions on Electron Devices*, vol. 43, no. 4, pp. 554–560, 1996. DOI: 10.1109/16.485537.

[60] O. L. Curtis and J. R. Srour, "The multiple-trapping model and hole transport in sio_2," *Journal of Applied Physics*, vol. 48, no. 9, pp. 3819–3828, 1977. DOI: 10.1063/1.324248.

[61] R. C. Hughes, "Hole mobility and transport in thin sio_2 films," *Applied Physics Letters*, vol. 26, no. 8, pp. 436–438, 1975. DOI: 10.1063/1.88200.

[62] E. Gnani, S. Reggiani, and M. Rudan, "Density of states and group velocity of electrons in sio_2 calculated from a full band structure," *Phys. Rev. B*, vol. 66, pp. 195–205, 19 2002. DOI: 10.1103/PhysRevB.66.195205.

[63] H.-J. Fitting and J.-U. Friemann, "Monte-carlo studies of the electron mobility in sio_2," vol. 69, pp. 349–358, 1 1982. DOI: doi:10.1515/9783112494400-034.

[64] F. McLean, H. B. Jr., and T. Oldham, *Electron-hole generation, transport, and trapping in SiO_2, Chapter 3 in Ionizing Radiation Effects in MOS Devices and Circuits*. Eds. New York Wiley, 1989.

[65] C. Brisset, V. Ferlet-Cavrois, O. Flament, *et al.*, "Two-dimensional simulation of total dose effects on nmosfet with lateral parasitic transistor," *IEEE Transactions on Nuclear Science*, vol. 43, no. 6, pp. 2651–2658, 1996. DOI: 10.1109/23.556849.

[66] J. Leray, P. Paillet, V. Ferlet-Cavrois, C. Tavernier, K. Belhaddad, and O. Penzin, "Impact of technology scaling in soi back-channel total dose tolerance. a 2-d numerical study using self-consistent oxide code," *IEEE Transactions on Nuclear Science*, vol. 47, no. 3, pp. 620–626, 2000. DOI: 10.1109/23.856489.

[67] C. Canali, G. Majni, R. Minder, and G. Ottaviani, "Electron and hole drift velocity measurements in silicon and their empirical relation to electric field and temperature," *IEEE Transactions on Electron Devices*, vol. 22, no. 11, pp. 1045–1047, 1975. DOI: 10.1109/T-ED.1975.18267.

[68] D. K. Ferry, "Electron transport and breakdown in sio2," *Journal of Applied Physics*, vol. 50, no. 3, pp. 1422–1427, 1979. DOI: 10.1063/1.326125.

[69] M. Ieong, P. Solomon, S. Laux, H.-S. Wong, and D. Chidambarrao, "Comparison of raised and schottky source/drain mosfets using a novel tunneling contact model," pp. 733–736, 1998. DOI: 10.1109/IEDM.1998.746461.

[70] Y. Sugimoto, M. Kajiwara, K. Yamamoto, Y. Suehiro, D. Wang, and H. Nakashima, "Effective work function modulation of tan metal gate on hfo_2 after postmetallization annealing," *Applied Physics Letters*, vol. 91, no. 11, pp. 105 –112, 2007. DOI: 10.1063/1.2783472.

[71] T. H. Ning, "High-field capture of electrons by coulomb-attractive centers in silicon dioxide," *Journal of Applied Physics*, vol. 47, no. 7, pp. 3203–3208, 1976. DOI: 10.1063/1.323116.

[72] D. J. DiMaria, F. J. Feigl, and S. R. Butler, "Trap ionization by electron impact in amorphous sio2 films," *Applied Physics Letters*, vol. 24, no. 10, pp. 459–461, 1974. DOI: 10.1063/1.1655011.

[73] P. Solomon, "High-field electron trapping in sio2," *Journal of Applied Physics*, vol. 48, no. 9, pp. 3843–3849, 1977. DOI: 10.1063/1.324253.

[74] J. Albohn, W. Füssel, N. D. Sinh, K. Kliefoth, and W. Fuhs, "Capture cross sections of defect states at the si/sio2 interface," *Journal of Applied Physics*, vol. 88, no. 2, pp. 842–849, 2000. DOI: 10.1063/1.373746.

[75] M. H. Chang, J. Zhang, and W. Zhang, "Assessment of capture cross sections and effective density of electron traps generated in silicon dioxides," *IEEE Transactions on Electron Devices*, vol. 53, pp. 1347–1354, 2006. DOI: 10.1109/TED.2006.874155.

[76] G. Hurkx, D. Klaassen, and M. Knuvers, "A new recombination model for device simulation including tunneling," *IEEE Transactions on Electron Devices*, vol. 39, no. 2, pp. 331–338, 1992. DOI: 10.1109/16.121690.

[77] G. Vincent, A. Chantre, and D. Bois, "Electric field effect on the thermal emission of traps in semiconductor junctions," *Journal of Applied Physics*, vol. 50, no. 8, pp. 5484–5487, 1979. DOI: 10.1063/1.326601.

[78] D. Arnold, E. Cartier, and D. J. DiMaria, "Theory of high-field electron transport and impact ionization in silicon dioxide," *Phys. Rev. B*, vol. 49, pp. 10 278–10 297, 15 1994. DOI: 10.1103/PhysRevB.49.10278.

[79] R. V. Overstraeten and H. D. Man, "Measurement of the ionization rates in diffused silicon p-n junctions," *Solid-State Electronics*, vol. 13, no. 5, pp. 583–608, 1970. DOI: https://doi.org/10.1016/0038-1101(70)90139-5.

[80] A. G. Chynoweth, "Ionization rates for electrons and holes in silicon," *Phys. Rev.*, vol. 109, pp. 1537–1540, 5 1958. DOI: 10.1103/PhysRev.109.1537.

[81] Y. Okuto and C. Crowell, "Threshold energy effect on avalanche breakdown voltage in semiconductor junctions," *Solid-State Electronics*, vol. 18, no. 2, pp. 161–168, 1975. DOI: https://doi.org/10.1016/0038-1101(75)90099-4.

[82] M. Rudan, R. Katilius, S. Reggiani, E. Gnani, and G. Baccarani, "Impact-ionization coefficient in silicon at high fields - a parametric approach," *Journal of Computational Electronics*, vol. 7, pp. 151–154, 2008. DOI: 10.1007/s10825-008-0184-8.